DECOVALEX-2023
Task C Final Report

Bastian Graupner, Kate Thatcher, Rebecca Newson

With contributions from:
Aqeel Afzal Chaudhry, Changsoo Lee, Chan-Hee Park, Dmitri Naumov, Edward Matteo, Hua Shao, J Taehyun Kim, Jan Thiedau, Jonny Rutqvist, Jörg Buchwald, Larissa Friedenberg, Merle Bjorge, Michael Pitz, Peng-Zhi Pan, Ruiping Guo, Sonja Kaiser, Teklu Hadgu, Thomas Dewers, Thomas Nagel, Wenbo Hou, Wenqing Wang and Wolfram Rühaak

April 2024

Disclaimer

This document was prepared as an account of the international research project DECOVALEX-2023 comprising participants from industry, government and academia, with funding organizations--Andra, BASE, BGE, BGR, CAS, CNSC, COVRA, U.S. DOE, Enresa, ENSI, JAEA, KAERI, NWMO, NWS, SÚRAO, SSM and Taipower. The statements made in the report are, however, solely those of the authors and do not necessarily reflect those of the Funding Organizations. While this document is believed to contain correct information, neither the United States Government nor any agency thereof, nor the Regents of the University of California, nor any of their employees, makes any warranty, express or implied, or assumes any legal responsibility for the accuracy, completeness, or usefulness of any information, apparatus, product, or process disclosed, or represents that its use would not infringe privately owned rights. Reference herein to any specific commercial product, process, or service by its trade name, trademark, manufacturer, or otherwise does not necessarily constitute or imply its endorsement, recommendation, or favoring by the United States Government or any agency thereof or the Regents of the University of California. The views and opinions of the authors expressed herein do not necessarily state or reflect those of the United States Government, any agency thereof, or the Regents of the University of California.

This technical document does not consider contractual limitations or obligations under the Standard Contract for Disposal of Spent Nuclear Fuel and/or High-Level Radioactive Waste (Standard Contract) (10 CFR Part 961).

To the extent discussions or recommendations in this document conflict with the provisions of the Standard Contract, the Standard Contract governs the obligations of the parties, and this presentation in no manner supersedes, overrides, or amends the Standard Contract.

No inferences should be drawn from this document regarding future actions by DOE, which are limited by the terms of the Standard Contract and Congressional appropriations for the Department to fulfill its obligations under the Nuclear Waste Policy Act, including licensing and constructing a spent nuclear fuel repository.

Copyright

DECOVALEX-2023

Task C Final Report

Main Authors :

Bastian Graupner
Swiss Federal Nuclear Safety Inspectorate (ENSI)

Kate Thatcher, Rebecca Newson
Quintessa Ltd

Contributing Authors (alphabetical by organisation):

Merle Bjorge, Wolfram Rühaak
Federal Company for Radioactive Waste Disposal (BGE)

Hua Shao, Jan Thiedau, Michael Pitz
Federal Institute for Geosciences and Natural Resources (BGR)

Peng-Zhi Pan, Wenbo Hou
Chinese Academy of Sciences (CAS)

Larissa Friedenberg
Gesellschaft für Anlagen- und Reaktorsicherheit (GRS)

Taehyun Kim, Changsoo Lee
Korea Atomic Energy Research Institute (KAERI)

Chan-Hee Park
Korea Institute of Geoscience and Mineral Resources (KIGAM)

Jonny Rutqvist
Lawrence Berkeley National Laboratory (LBNL)

Ruiping Guo
Nuclear Waste Management Organization (NWMO)

Teklu Hadgu, Edward Matteo, , Thomas Dewers
Sandia National Laboratories

Aqeel Afzal Chaudhry, Dmitri Naumov, Sonja Kaiser, Thomas Nagel
Technische Universität Bergakademie Freiberg (TUBAF)

Jörg Buchwald, Wenqing Wang
Helmholtz-Zentrum für Umweltforschung (UFZ)

Reviewed by AE Bond

Published 29/11/2024
LBNL-2001623

Preface

The DECOVALEX Project is an ongoing international research collaboration established in 1992 to advance the understanding and modeling of coupled Thermal (T), Hydrological (H), Mechanical (M), and Chemical (C) processes in geological systems. DECOVALEX was initially motivated by recognising that predicting these coupled effects is essential to the performance and safety assessment of geologic disposal systems for radioactive waste and spent nuclear fuel. Later, it was realized that these processes also play a critical role in other subsurface engineering activities, such as subsurface CO_2 storage, enhanced geothermal systems, and unconventional oil and gas production through hydraulic fracturing. Research teams from many countries (e.g., Canada, China, Czech Republic, Finland, France, Germany, Japan, Netherlands, Republic of Korea, Spain, Sweden, Switzerland, Taiwan, United Kingdom, and the United States) various institutions have participated in the DECOVALEX Project over the years, providing a wide range of perspectives and solutions to these complex problems. These institutions represent radioactive waste management organizations, national research institutes, regulatory agencies, universities, and industry and consulting groups.

At the core of the collaborative work within DECOVALEX is the collaborative analysis and comparative modeling of state-of-the-art field and laboratory experiments. DECOVALEX engages model comparison in a broad and comprehensive sense, including the modelers' interpretation of experimental data, selection of boundary conditions, rock and fluid properties, etc., and their choice of coupling schemes and simulators. This recent phase of DECOVALEX has expanded the work scope to include the modelers being challenged to gain an understanding of the representation coupled processes in generic 'whole system' or 'performance assessment' models. In-depth and detailed discussions among the teams yield insight into the coupled THMC processes and stimulate the development of modeling capabilities and measurement methods. This would have been impossible if only one or two groups had studied the data.

Since the project initiation, DECOVALEX has been organized in several four-year phases, each featuring several modeling tasks of importance to radioactive waste disposal and other geoscience applications. Seven project phases were successfully concluded between 1992 and 2019, the results of which have been summarized in several overview publications (e.g., Tsang et al., 2009; Birkholzer et al., 2018; Birkholzer et al., 2019, Birkholzer et al., 2024). The most recent phase, DECOVALEX-2023, started in 2020 and ended in 2023. Seven tasks were conducted in DECOVALEX-2023, as follows:

- **Task A: HGFrac** – Thermal- and gas- induced fracturing of the Callovo-Oxfordian Clay, France
- **Task B: MAGIC** – Migration of gas in compacted clay
- **Task C: FE Experiment** – Thermal-hydro-mechanical (THM) modelling of the FE experiment at Mont Terri, Switzerland
- **Task D: Horonobe EBS Experiment** - THM modelling of the Horonobe EBS experiment at the Horonobe URL, Japan
- **Task E: BATS** – THM modeling for the Brine Availability Test in Salt (BATS) at the WIPP, New Mexico, USA

- **Task F: Performance Assessment** – Comparative generic performance assessment models in crystalline and salt formations
- **Task G: SAFENET** – Laboratory-scale TH and THM analyses of single fractures

The DECOVALEX Project would not have been possible without the support and engagement of the participating organizations who jointly support the coordination of the project within a given project phase, propose and coordinate modeling tasks, including the necessary experimental data, and deploy their research team (or teams) working on a selection of the tasks conducted in the project. The partner organizations in DECOVALEX-2023 were:

- Andra, National Radioactive Waste Management Agency, *France*
- BASE, Federal Office for the Safety of Nuclear Waste Management*, Germany*
- BGE, Federal Company for Radioactive Waste Disposal, *Germany*
- BGR, Federal Institute for Geosciences and Natural Resources, *Germany*
- CAS, Chinese Academy of Sciences, *China*
- CNSC, Canadian Nuclear Safety Commission, *Canada*
- COVRA, Central Organisation for Radioactive Waste, *Netherlands*
- DOE, Department of Energy, *USA*
- Enresa, National Radioactive Waste Management Agency, *Spain*
- ENSI, Swiss Federal Nuclear Safety Inspectorate, *Switzerland*
- JAEA, Japan Atomic Energy Agency, *Japan*
- KAERI, Korea Atomic Energy Research Institute, Republic of Korea
- NWMO, Nuclear Waste Management Organization, *Canada*
- NWS, Nuclear Waste Services, *United Kingdom*
- SSM, Swedish Radiation Safety Authority, *Sweden*
- SÚRAO, Radioactive Waste Repository Authority, *Czech Republic*
- Taipower, Taiwan Power Company, *Taiwan*

We are extremely grateful to these organizations for their financial and technical support of DECOVALEX-2019.

Jens Birkholzer (Chairman of the DECOVALEX project) and Alex Bond (Technical Coordinator of the DECOVALEX Project).

Berkeley, California, USA, October 2024

References:

Birkholzer, J.T., Bond, A.E., Hudson, J.A., Jing, L., Tsang, C.-F., Shao, H., Kolditz, O. (2018): DECOVALEX-2015 - An International Collaboration for Advancing the Understanding and Modeling of Coupled Thermo-Hydro-Mechanical-Chemical (THMC) Processes in Geological Systems, Environmental Earth Sciences, 77(14). https://doi.org/10.1016/j.ijrmms.2022.105097

Birkholzer, J.T., Tsang, C.-F., Bond, A.E., Hudson, J.A., Jing, L., and Stephansson, O. (2019): 25 Years of DECOVALEX - Scientific Advances and Lessons Learned from an International Research Collaboration in Coupled Subsurface Processes, Invited Review, International Journal and Rock Mechanics and Mining Sciences, 122. https://doi.org/10.1016/j.ijrmms.2019.03.015

Birkholzer, J.T., Bond, A.E. and Tsang, C.-F. (2024). The DECOVALEX international collaboration on modeling of coupled subsurface processes and its contribution to confidence building in

radioactive waste disposal. Hydrogeology Journal, https://doi.org/10.1007/s10040-024-02799-7

Tsang, C.-F., Stephansson, O., Jing, L., and Kautsky, F. (2009): DECOVALEX Project: from 1992 to 2007. Environmental Geology, 57(6). https://doi.org/10.1007/s00254-008-1625-1

Summary

The Full-scale Emplacement (FE) heater experiment at the Mont Terri Underground Rock Laboratory (URL) was designed and conducted by Nagra to replicate an emplacement tunnel of Nagra's reference repository design at 1:1 scale. Alongside testing the technical feasibility of constructing disposal tunnels, emplacing waste containers in the tunnels and then backfilling them, the main goals of the FE experiment are (1) to obtain a better understanding of the coupled effects of induced thermo-hydro-mechanical (THM) processes that may occur and (2) to validate existing coupled THM models (Müller et al., 2017).

A key aspect of ensuring safety for repositories located in low-permeability rock involves minimizing any damage to the rock itself, thereby preserving its integrity and promoting a stable environment Amongst a number of processes that could damage the rock is the increase in pore pressure due to thermal loading caused by heat emitted from the waste. To reduce the potential damage of the rock, it is important to analyse the evolution of heat over time due to the heat load of the containers and assess possible consequences by coupled THM models. The aim of Task C of DECOVALEX-2023 was to build 3D numerical models of the FE experiment, focussing in particular on the heating induced pore pressure change in the Opalinus Clay.

Data from a large number of sensors were available from the FE experiment for model comparison. These sensors measured temperature and relative humidity in the bentonite around the heaters, and temperature, pressure and displacement/strain in the surrounding Opalinus clay. Data were available from the start of excavation (April 2012) up to August 2020 for most sensors (more than 5 years from the start of heating in December 2014).

To fulfil the overall aim of the task, the work was broken down into a number of steps, starting with simpler models to build confidence in each team's approach and then moving to more complex models that better represent the FE experiment.

Step 0 consisted of 2D benchmark models, gradually increasing the number of processes that are represented from thermal (T) only models in Step 0a, to coupled thermal-hydraulic (TH) models in Step 0b with a representation of changing porosity, to coupled thermo-hydro-mechanical (THM) models in Step 0c, where porosity changes are calculated by the mechanical model. A detailed specification of processes, parameters, initial and boundary conditions was provided for this step, with the ambition that all teams would work towards close agreement in their model results, thus building confidence in the model implementations.

It was not straightforward to achieve agreement between the teams, so additional steps (Step 0b2, 0b3, 0c2, 0c3) were added along with derivation of some analytical solutions against which the models could be compared. The reasons for the differences between teams were investigated and found to be caused primarily by different conceptual model assumptions (including temperature dependence of the thermal expansion of water), different model formulations (including porosity evolution) and differences in modelled domain sizes, boundary conditions and grid discretisation. This demonstrates that comparisons between multiple modelling teams and/or comparison with analytical results and experimental data are highly beneficial in providing an indication of uncertainty in model predictions. At the conclusion of Step 0, almost all teams had achieved a close agreement in model results and those that had not achieved an agreement knew the reason for this.

Step 1 moved from 2D models to 3D models of the FE experiment without adding technical features like shotcrete or EDZ, and only considering the heating phase. Initially the 3D model was tightly specified to continue to build confidence in the model implementations (Step 1a). The results of Step 1a were compared to the data from the FE-experiment without the teams seeing the data. The teams were then provided with a sub-set of the data from the FE-experiment and invited to consider how best to use the large dataset for model comparison (Step 1b). Teams were then asked to use the data provided to calibrate their models, only changing material property values rather than adding features or processes to their models (Step 1c). In Step 1, teams were asked to only model the heating phase of the experiment, so pressure in the Opalinus Clay was reported as change in pressure since the initial conditions were specified rather than modelled. The change from 2D to 3D models was accompanied by an increase in the dispersion of results between the teams. Some of this was resolved during the task, but some remained and is potentially due to model discretisation. Calibration of parameters was useful in improving the fit of the models to the data but the remaining differences indicated that the models were missing features or processes.

In Step 2, the teams were asked to update their models with additional features and processes as well as calibrating parameters to try and improve the fit of the models to the data. Teams were encouraged to represent ventilation of the open FE tunnel prior to backfilling with heaters and bentonite and in Step 2, the absolute pressure in the Opalinus Clay was compared between the teams. Teams took different approaches, but there was consideration of adding shotcrete and an EDZ into the model, representing stress change during excavation and different approaches to modelling ventilation of the FE tunnel. Overall, the documented results showed a very good agreement for temperature. The results for porewater pressure evolution showed a significant

improvement for most teams compared to Step 1c with a good agreement to the measurements for several teams whereas some teams overpredicted the pressure increase and others overpredicted the drainage effect especially for the sensors close to the heater.

Step 3 was an opportunity for teams to use the models developed in Step 1 and Step 2 to make predictions about the temperature and pressure changes that will be expected at the FE experiment over the next few years in light of the planned changes in thermal output of the heaters.

Contents

1 Introduction

The Full-scale Emplacement experiment (FE experiment) at the Mont Terri Underground Rock Laboratory (URL) was designed and conducted by Nagra to replicate an emplacement tunnel of Nagra's reference repository design at 1:1 scale. Alongside testing the technical feasibility of constructing disposal tunnels, emplacing waste canisters in the tunnels and then backfilling them, the main goals of the FE experiment are (1) to obtain a better understanding of the coupled effects of induced thermo-hydro-mechanical (THM) processes that may occur once the actual repository is in operation and (2) to validate existing coupled THM models (Müller *et al*. 2017).

A key aspect of ensuring safety for repositories located in low-permeability rock involves minimizing any damage to the rock itself, thereby preserving its integrity and promoting a stable environment. Amongst a number of processes that could damage the rock is the increase in pore pressure due to thermal loading caused by heat emitted from the waste. Heating of both the rock and the pore water leads to expansion, with water expanding more than the rock and hence the pore pressure increasing. This in turn decreases the effective stress on the rock, making it more susceptible to fracturing. To reduce the potential damage of the rock, it is important to analyse the evolution of heat over time due to the heat load of the containers and assess possible consequences by coupled THM models. Similar work has been performed before for smaller heater tests (Garitte *et al*., 2017) and in other host rocks (Plua *et al*., 2020) and it was assumed that the underlying physical processes are well understood.

The aim of Task C of DECOVALEX-2023 was to build 3D numerical models of the FE experiment, focussing in particular on the heating induced pore pressure change in the Opalinus Clay. The task contributed to the validation of existing mathematical models against data from the FE experiment. The challenge here was in representing a large experiment in numerical codes and using the simulations to help analyse a large dataset from the experiment. The models were also used to investigate how engineering factors (e.g. shotcrete, tunnel shape) affect pore pressure safety margins in the repository.

This report introduces the Steps in Task C (Chapter 2) and the teams participating in Task C (Chapter 3). Steps 0 to 3 are reported in Chapter 4 to Chapter 7, with a summary of the outcomes and conclusions of Task C given in Chapter 8.

2 Task Outline

The task was broken down into several steps, starting with simpler models to build confidence in each team's numerical implementation and moving to more complex models that better represent the FE experiment.

Step 0 – 2D Benchmark Cases

Aim: To build confidence in the numerical implementation of physical processes in each team's code and achieve agreement in model results between the teams so differences in subsequent steps can be understood.

Objectives: Achieve agreement across the teams through following a tightly defined model specification, or understand why models give different results, for three models with increasing complexity.

- **Step 0a:** a 2D T simulation;
- **Step 0b:** a 2D TH+vapour simulation;
- **Step 0c:** a 2D THM simulation.

Step 1 – Heating phase of FE experiment

Aim: Continue to build confidence in the teams' models by moving to 3D but maintain a tightly defined specification. Perform an initial comparison of models against data from the FE experiment to begin to validate the THM approach and consider shortcomings in the simplifications made in the specification.

Objectives: Comparison of models against data from the FE experiment for three cases, focussing on pressure changes during the heating phase rather than absolute pressure.

- **Step 1a:** a 3D THM simulation of the heating phase of the FE experiment, following the tightly defined model specification.
- **Step 1b:** comparison of the model results against the data available and consideration of how best to use the large dataset available.
- **Step 1c:** calibration of the material parameters in the 3D THM model with no addition of features or processes to the model.

Step 2 – FE experiment from ventilation to heating

Aim: To allow teams to move away from the tightly defined specification, towards improved calibrations of the 3D FE experiment model, which can represent absolute pressure in the Opalinus Clay. Teams could add additional processes and features to the model to test their importance and improve fits to the data.

Processes that teams added to the models included representing excavation and ventilation of the FE tunnel prior to backfilling. Additional features that teams included were shotcrete lining the tunnel and the excavation damage zone (EDZ) in the Opalinus Clay around the tunnel. Teams were free to choose the level of complexity they wanted to include in the model.

Step 3 – Extended heating prediction

Aim: Predict temperature and pressure in the Opalinus Clay as a function of time, taking into account the heating schedule that has and will be implemented at the FE experiment.

In addition to the steps outlined here, some teams undertook side studies on various features of the modelling geometry, parameterisation and boundary conditions which are also reported in the subsequent sections of this report.

3 Participants, Modelling approaches and Codes Involved

Nine teams were involved in Task C, using eight different codes (Table 1). This is a large number of teams and codes, which provided an opportunity for constructive comparison across a wide range of codes and modellers with a range of levels of experience. Further detail on the organisations involved and the codes used is provided in the following subsections.

Table 1: Modelling teams involved in Task C.

Team	Funding Organisation	Code
BGE/TUBAF	BGE	OpenGeoSys 6
BGR/UFZ	BGR	OpenGeoSys 5 and 6
CAS	CAS	CASRock
DOE/LBNL	DOE	TOUGH-FLAC
ENSI	ENSI	OpenGeoSys 6
GRS	BGR	CODE_BRIGHT
KAERI/KIGAM	KAERI	OpenGeoSys 5 and OpenGeoSys-FLAC3D
NWMO	NWMO	COMSOL Multiphysics ®
DOE/SNL	DOE	PFLOTRAN, COMSOL Multiphysics ®

3.1 BGE/TUBAF

The Federal Company for Radioactive Waste Disposal (BGE) is responsible for implementing and performing tasks in the final disposal of radioactive waste in Germany. This includes, besides other tasks, the search for a site with the best possible safety for the disposal of high-level radioactive waste in Germany. To perform these various tasks, BGE commissions and funds a broad variety of research and development projects. In 2020, the site selection department of BGE initiated participation in the DECOVALEX project in cooperation with the Technische Universität Bergakademie Freiberg (TUBAF).

TUBAF, as the so-called “University of Resources”, focuses its activities on environment, energy, resources and materials. The Geotechnical Institute works in the field of utilizing the earth’s crust in a safe and sustainable manner. This includes topics like radioactive waste repositories in different host rocks (salt, crystalline, clay), geothermal energy production, gas storage or geo-infrastructures. To address these challenges the facilities of the geomechanical laboratories, the local teaching and research mine "Reiche Zeche" and numerical simulations are used. As part of the Centre for Environmental Geosciences jointly operated by the Helmholtz-Centre for Environmental Research (UFZ) and TUBAF, both institutions continue their collaboration in the development of the numerical simulation platform OpenGeoSys for coupled multiphysics problems. The development focus at the TUBAF group is on nonlinear mechanics of porous media, high-temperature applications in reactive porous media and geotechnical applications in the field of energy supply, storage and disposal. Recent work has addressed the

quantification of uncertainties and the use of physics-constrained neural networks in geotechnical applications.

OpenGeoSys (OGS) is a scientific open-source initiative for the numerical simulation of thermo-hydro-mechanical/chemical (THMC) processes in fractured porous media. The OGS framework is targeting applications in various areas of environmental geoscience, including hydrogeology, energy storage, geothermics and geotechnics. The most recent version, OpenGeoSys-6 (OGS-6) (Bilke *et al*., 2019) relies on advanced methods in software engineering and architecture with a focus on code quality, modularity, performance and comprehensive documentation. Particular emphasis is put on the implementation of advanced numerical methods for the evolution of discontinuities, such as enriched finite element function spaces, non-local formulations and phase-field models for fracture with the ability to utilize HPC platforms. For more information please refer to the OpenGeoSys webpage www.opengeosys.org and the following references (Kolditz *et al*., 2019; Lehmann *et al*., 2024).

3.2 BGR/UFZ

The Federal Institute for Geosciences and Natural Resources (BGR) is the central geoscientific authority providing advice to the German Federal Government with independent and neutral advice on all geoscientific and geotechnical issues involved in the Federal Government's nuclear repository projects (www.bgr.de).

For the existing repository locations in Germany - Konrad, Asse and Morsleben - BGR undertakes these responsibilities by working together closely and successfully with the BGE (the Federal Company for Radioactive Waste Disposal) on the basis of an administrative agreement. BGR's expertise in the disposal of radioactive waste in deep geological formations includes:

1. site selection investigations
2. geological-geotechnical and geophysical site exploration
3. characterization of host rocks
4. scenario analysis and long-term safety
5. modelling the overall geological situation

Additionally, BGR actively carries out its own research, enabling BGR scientists to develop the state-of-the-art science and technologies needed to evaluate repository issues. This research is often carried out in collaboration with other national and international institutes and aims to develop and test methods and equipment for the geoscientific exploration of potential repository sites. The Helmholtz Centre for

Environmental Research (UFZ), a member of the Helmholtz Association of German Research Centers established in 1991, is one of the world's leading research centres in the field of environmental research, enjoying high social recognition (www.ufz.de). The Department of Environmental Informatics (ENVINF) is a department of UFZ that specially focuses on developing models and software to simulate environmental processes in hydrological, geological, and energy-technical systems.

In order to ensure the reliability of simulations of environmental processes, ENVINF of UFZ bundles a complete workflow from data collection and integration to process simulation and data analysis to scientific visualization into a quality-assured, open-source software package. This package consists of the process simulator, OpenGeoSys (OGS); the data integration and visualization tool, OGS Data Explorer; and a link to the UFZ's visualization centre. In that open-source software package, OGS is a scientific, open-source project for the development of numerical methods for the simulation of THMC processes in porous and fractured media. OGS is object-oriented designed and implemented in C++, and it focuses on the numerical solution of coupled multi-field problems (multi-physics). Parallel versions of OGS are available relying on both MPI and OpenMP concepts. Application areas of OGS currently include water resources management, hydrology, geothermal energy, energy storage, CO_2 sequestration, and waste deposition. The source code of OGS is hosted on Github and Gitlab (OGS 5: https://github.com/ufz/ogs5, OGS6: https://gitlab.opengeosys.org/ogs/ogs), and its documentation can be found on https://www.opengeosys.org/docs/.

3.3 CAS

The Institute of Rock and Soil Mechanics, Chinese Academy of Sciences (CAS) is a comprehensive research institution specializing in the basic research and applications of geomechanics and geotechnical engineering. The institute focuses on the main research areas, including prevention and control of major engineering disasters, exploitation of energy and resources, and protection of marine and ecological environment.

CAS has participated in the DECOVALEX project since 2004. The team uses a self-developed numerical code, the "Cellular Automata Software for the engineering Rockmass fracturing process" (CASRock), for various tasks of the DECOVALEX project. The code contains a series of previously developed numerical systems, namely EPCA for simulation of heterogeneous rock failure process, VEPCA for visco-elastoplastic analysis, D-EPCA for rock dynamic response simulation, THMC-EPCA for coupled THMC processes in geological media and RDCA2D for simulation of rock cracking process from continuity

to discontinuity (Pan *et al*., 2009, 2012a, 2012b, 2013, 2016, 2017; Mei *et al*., 2021; Feng *et al*., 2021).

3.4 DOE/LBNL

Berkeley Lab (LBNL) is a member of the national laboratory system supported by the U.S. Department of Energy (DOE) through its Office of Science. It is managed by the University of California (UC) and is charged with conducting unclassified research across a wide range of scientific disciplines. The Laboratory's scientific divisions are organized within six areas of research: Computing Sciences, Physical Sciences, Earth and Environmental Sciences, Biosciences, Energy Sciences, and Energy Technologies.

The TOUGH-FLAC simulator (Rutqvist *et al*., 2002; Rutqvist 2011; 2017; Rinaldi *et al*.,2022) is based on linking the TOUGH2 or TOUGH3 multiphase flow and heat transport simulators (Pruess *et al*., 2012; Jung *et al*., 2017) with the FLAC3D geomechanical simulator (Itasca 2017). In this approach, TOUGH2 or TOUGH3 is used for solving multiphase flow and heat transport equations, whereas FLAC3D is used for solving geomechanical stress-strain equations. In this task, TOUGH3 and FLAC3DV7 were used with improved computational performance through more efficient couplings and parallel computing (Rinaldi *et al*., 2022).

3.5 ENSI

ENSI, the Swiss Federal Nuclear Safety Inspectorate, is the national regulatory body with responsibility for the nuclear safety and security of Swiss nuclear facilities. ENSI is responsible for the supervision of the continuing geoscientific investigations to identify a suitable location for the deep geological disposal of radioactive waste.

ENSI has participated in the DECOVALEX project since 2012 (e.g. Rutqvist *et al*. 2020, Graupner *et al*. 2018). In the earlier phases, ENSI used the code OpenGeoSys version 5. Since then, the newer version 6 has become available and is applied by ENSI for this task (Bilke *et al*., 2019). This code is suitable for the simulation of thermo-hydro-mechanical-chemical (THMC) processes in porous and fractured media. In particular, the monolithic coupling of the thermal, hydraulic and mechanical processes might have improvements with respect to numerical stability and time stepping, which will be investigated during the course of the task. See chapter 3.2 for more explanations.

3.6 GRS

Gesellschaft für Anlagen- und Reaktorsicherheit (GRS) gGmbH is a non-profit and independent organisation which deals with technical-scientific research and provides expertise. The company administers interdisciplinary knowledge, progressive methods and qualified data. It carries out research and analysis in its fields of competence, namely reactor safety and radioactive waste management as well as radiation and environmental protection.

GRS has locations in Cologne, Garching, Berlin and Braunschweig. The Repository Safety Research department participating in DECOVALEX-2023 is located in Braunschweig and combines long-term safety with process analysis in conjunction with an on premises geo-scientific lab.

For numerical simulations in the field of process analysis, the finite element method (FEM) code CODE_BRIGHT is applied. CODE_BRIGHT is designed for handling thermo-hydro-mechanical (THM) coupled problems in geological media. The theoretical approach includes a set of governing equations, a set of constitutive laws and a special computational approach (Olivella *et al.*, 2021). More information about CODE_BRIGHT can be found at: https://deca.upc.edu/en/projects/code_bright.

CODE_BRIGHT has been used by GRS for several years in research projects connected to repository research comprising different kind of host rocks and engineered barrier materials.

3.7 KAERI / KIGAM

The Korea Atomic Energy Research Institute (KAERI), a government-funded research institute established by “the Act on the Establishment, Operation and Fostering of Government-funded Science and Technology Research Institutes, etc.”, contributes to academic advancement, energy acquisition, and utilization of nuclear energy through active research and development in related fields. Since its establishment in 1959, KAERI has been the only research institute in Korea dedicated to nuclear energy (www.kaeri.re.kr).

As Korea’s unique government-funded Geoscience research organization, the Korea Institute of Geoscience and Mineral Resources (KIGAM) has contributed to resolving public safety issues and national developments since the foundation of the Geological Survey of Korea in 1918 (www.kigam.re.kr).

KAERI/KIGAM use two different numerical programs of; OpenGeoSys-5, a well-known open-source software; and OpenGeoSys-FLAC3D, a self-developed numerical module combining OpenGeoSys and FLAC3D. OpenGeoSys-5 is a multi-platform supported analysis software to analyse complex THM coupled behaviours in porous or fractured media. OpenGeoSys is implemented in the C language with high versatility and has strengths in TH analysis related to nuclide transport and multiphase fluid flow that can occur in a high-level radioactive waste repository in particular. Therefore, various experts in fields such as physics, chemistry, mathematics, fluid mechanics, and rock mechanics continuously develop their codes in the areas of interest.

OGSFLAC (Park *et al*, 2019, Kim *et al*, 2021), a self-developed code, is a program that combines OpenGeoSys and FLAC3D to enhance the advantages of each code. FLAC3D was developed by ITASCA and performs engineering calculations based on the finite difference method. It provides various constitutive models for ground stability analysis and has strengths in the field of mechanical analysis. Therefore, KAERI/KIGAM developed a numerical simulator named OGSFLAC, linking two programs to enhance the strengths of each program. OGSFLAC is based on a sequential coupling scheme, and OpenGeoSys solves TH analysis with time step decision while FLAC3D manages mechanical analysis depending on OpenGeoSys time-stepping analyses.

3.8 NWMO

The Nuclear Waste Management Organization (NWMO) is responsible for designing and implementing Canada's plan for the safe, long-term management of used nuclear fuel. The plan, known as Adaptive Phased Management, requires used fuel to be contained and isolated in a deep geological repository. It also calls for a comprehensive process to select an informed and willing host for the project.

The NWMO is a not-for-profit organization established in 2002 by Canada’s nuclear electricity producers in accordance with the Nuclear Fuel Waste Act (NFWA). The founding members of the NWMO are Ontario Power Generation (OPG), New Brunswick Power Corporation, and Hydro-Québec (HQ). These organizations, along with Atomic Energy of Canada Limited (AECL), are mandated to fund NWMO’s operations.

COMSOL Multiphysics v5.6 (COMSOL, 2017) was used to perform this modelling exercise. COMSOL Multiphysics is a finite element modelling environment used to model and solve all kinds of scientific and engineering problems. The software provides an integrated desktop environment with a Model Builder that allows the user to solve coupled physics phenomena.

COMSOL is installed on a Dell Precision T7600 machine with Windows 7 professional running system with the following properties:

- Intel® Xeon® CPU E5-2680 0 @ 2.70 GHz 2.70 GHz (2 processors)
- 64GB (RAM)

The model is solved using 16 cores. A fully coupled solver is conducted with a Newton non-linear iteration scheme.

3.9 DOE/SNL

Sandia National Laboratories (SNL) is a multi-mission laboratory managed and operated by National Technology and Engineering Solutions of SNL LLC, a wholly owned subsidiary of Honeywell International Inc. for the U.S. Department of Energy's National Nuclear Security Administration.

The SNL Nuclear Fuel Cycle team leads in developing, integrating, and implementing technically safe, viable and sustainable solutions, R&D, and analyses for nuclear energy challenges, ranging from power conversion to the management of spent nuclear fuel and high-level radioactive waste.

For DECOVALEX-2023, Task C, the SNL team used PFLOTRAN for thermal and thermal-hydrologic simulations. The PFLOTRAN code is an open source, state-of-the-art, massively parallel subsurface flow and reactive transport code operating in a high-performance computing environment (Hammond *et al*., 2014).

For THM work on Task C, SNL used COMSOL Multiphysics v5.6 (COMSOL, 2020), which is used on a variety of desktop workstations and takes advantage of SNL's many high-performance computing systems. SNL have undertaken several inter-SNL code verification exercises between COMSOL and PFLOTRAN and are in the process of building confidence in modelling codes by undertaking this process.

4 Step 0 – 2D Benchmark Cases

4.1 Aim

The aim of the benchmark cases was to build confidence in each team's model implementation and the ability of each code to represent processes that are important in modelling the FE experiment. The benchmark cases were designed to start with simple cases and get gradually more complex, so that when models disagree, it is easier to pinpoint the reasons for this. With a tightly defined specification, the aim of this exercise was for all teams to achieve the same results, or to understand why some teams or codes were unable to agree. The aim of this step was not to produce the best model possible of the FE experiment, so the specification contains known simplifications to aid model comparison rather than try to replicate results from the FE experiment.

The tasks for this step were for teams to build three 2D variant case models:

1. A thermal (T) only model with constant saturation and to supply temperature data at specified output locations.
2. A thermal-hydraulic (TH) model with porosity change calculated based on pressure changes, and to supply temperature, pressure, and relative humidity data at specified output locations.
3. A thermal-hydraulic-mechanical (THM) model, where porosity changes are calculated using the mechanical model, and to supply temperature, pressure, relative humidity, stress, strain and displacement data at specified output locations.

4.2 Model specification

4.2.1 Geometry and measurement locations

The benchmark cases were based on a 2D geometry through the centre of the middle heater in the FE experiment (Figure 1). Details of the geometry are shown in Table 2. The heater is centred within the tunnel. A domain size of 50x50 m was recommended to ensure consistency between teams, although teams were free to test whether this domain size was large enough. The heater itself was not modelled but represented as hole.

The locations for data output for comparison are given in Table 3.

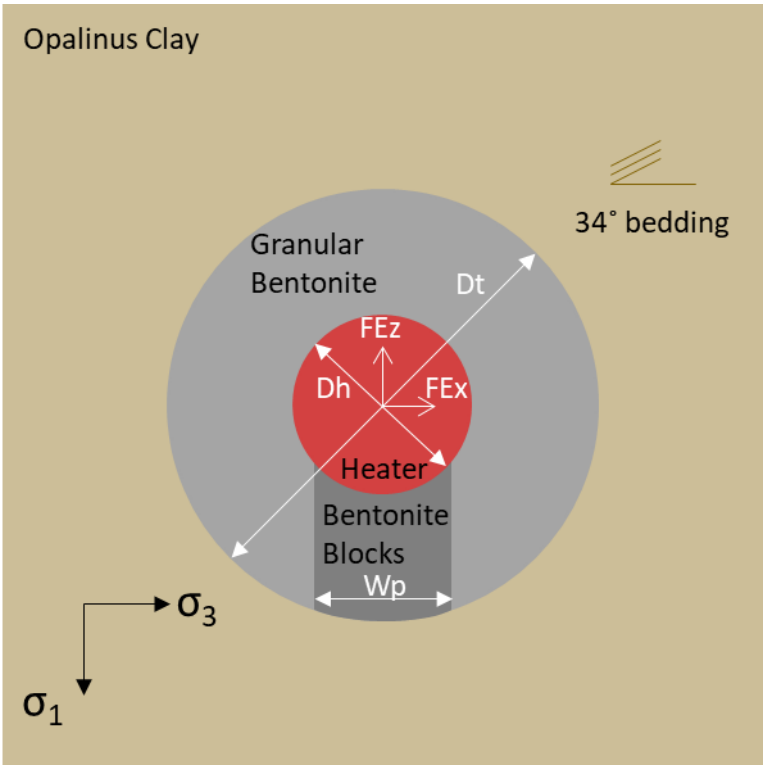

Figure 1 - Model geometry for Step 0.

Table 2: Details of the geometry for the 2D model.

Description	Value	Reference
Diameter of FE tunnel (Dt)	2.48 m	Nagra, 2019
Heater diameter (Dh)	1.05 m	Nagra, 2019
Pedestal width at base (Wp)	0.8 m	Nagra, 2019
Opalinus Clay domain	50 m x 50 m	

Table 3: Measurement locations and parameters for reporting.

Name	Radial distance from heater centre (m)	Angle (vertically upwards is zero and measured clockwise)	Parameters to be reported (where temperature is T, relative humidity is RH, porewater pressure is p_w and displacement is 'disp')		
			Step 0a	Step 0b	Step 0c
H_1	0.525	0	T	T, RH	T, RH, disp, strain, total stress
H_2	0.525	90	T	T, RH	T, RH, disp, strain, total stress
H_3	0.525	180	T	T, RH	T, RH, disp, strain, total stress
H_4	0.525	270	T	T, RH	T, RH, disp, strain, total stress
H_5	0.525	56	T	T, RH	T, RH, disp, strain, total stress
H_6	0.525	326	T	T, RH	T, RH, disp, strain, total stress
H_7	0.725	0	T	T, RH	T, RH, disp, strain, total stress
H_8	0.725	90	T	T, RH	T, RH, disp, strain, total stress
H_9	0.725	180	T	T, RH	T, RH, disp, strain, total stress
H_10	0.725	270	T	T, RH	T, RH, disp, strain, total stress
H_11	0.725	56	T	T, RH	T, RH, disp, strain, total stress
H_12	0.725	326	T	T, RH	T, RH, disp, strain, total stress
T_1	1.04	0	T	T, RH	T, RH, disp, strain, total stress
T_2	1.04	90	T	T, RH	T, RH, disp, strain, total stress
T_3	1.04	180	T	T, RH	T, RH, disp, strain, total stress
T_4	1.04	270	T	T, RH	T, RH, disp, strain, total stress
T_5	1.04	56	T	T, RH	T, RH, disp, strain, total stress
T_6	1.04	326	T	T, RH	T, RH, disp, strain, total stress
O_1	5	56	T	T, p_w	T, p_w, disp, strain, total stress
O_2	8	56	T	T, p_w	T, p_w, disp, strain, total stress
O_3	14	56	T	T, p_w	T, p_w, disp, strain, total stress
O_4	5	326	T	T, p_w	T, p_w, disp, strain, total stress
O_5	8	326	T	T, p_w	T, p_w, disp, strain, total stress
O_6	14	326	T	T, p_w	T, p_w, disp, strain, total stress

4.2.2 Material Properties

Three materials should be represented in the benchmark cases: Opalinus Clay, granular bentonite and bentonite blocks. The Opalinus Clay is bedded and has anisotropic THM properties in directions parallel and perpendicular to bedding. The bedding dips at 34˚ as shown in Figure 1.

A full parameterisation of material properties was provided to teams (Table 4) to aid comparison between teams.

Table 4: Material parameters for Step 0 based on Bock (2009), Bossart (2015), ENSI (2014) and Nagra (2019).

Input parameters		Symbol	Unit	OPA	GBM	Bentonite blocks	Source
Thermal parameters	Dry thermal conductivity parallel and perpendicular to bedding	$\lambda_{dry,\parallel}$	*W/mK*	2.4	0.35	0.26	
		$\lambda_{dry,\perp}$	*W/mK*	1.3			
	Saturated thermal conductivity parallel and perpendicular to bedding	$\lambda_{sat,\parallel}$	*W/mK*	2.4	1.2	0.96	
		$\lambda_{sat,\perp}$	*W/mK*	1.3			
	Solid specific heat capacity	c_s	J/kgK	995	800	800	
Hydraulic parameters	Dry Bulk Density	ρ_{bulk}	*kg/m³*	2340	1490	1690	NTB 15-02
	Porosity	ϕ	-	0.13	0.331	0.331	
	Intrinsic permeability	$k_{i,\parallel}$	*m²*	1.6E-20	3.5E-20	1.0E-22	
		$k_{i,\perp}$		1.0E-20			
	van Genuchten Entry Pressure	p_e	*MPa*	20.0	28.6	30	
	van Genuchten n	n	-	2.5	2.0	1.67	
	van Genuchten maximum water saturation	s_{max}	-	1.0	1.0	1.0	
	van Genuchten residual water saturation	s_r	-	0.0	0.0	0.0	
	Pore compressibility	c_{pore}	*1/Pa*	-	-	-	calculated from E, ν
Mechanical parameters	Young's modulus	$E_\parallel$	*MPa*	8000	18	24	
		$E_\perp$		4000			
	Shear modulus	$G_\perp$	*MPa*	3500	-	-	
	Poisson ratio	$\nu_\parallel$	-	0.35	0.35	0.2	
		$\nu_\perp$		0.25			
	Linear thermal expansion	α_T	*1/K*	1.5E-05	3.0E-06	3.0E-06	
	Biot coefficient	α	-	1	1	1	
Fluid parameters	Reference water density	ρ_{fluid_ref}	*kg/m³*	1000			
	Fluid compressibility	c_{fluid}	*1/Pa*	4.65E-10			
	Linear thermal expansion water	α_w	*1/K*	4.00E-04			
	Vapour diffusivity (vapour in air)	D_v	*m²/s*	2.42E-05			

C_p^{water} is specific heat capacity of water = 4181.3 J/kg/K;

ρ_g is grain density in kg/m^3;

R is the gas constant, 8.314472 (J mol-1 K-1); and

M is the molar mass of water vapour (0.018 kg mol-1).

4.2.3 Initial and boundary conditions

Initial and boundary conditions were specified as shown in Table 5.

Table 5: Initial and boundary conditions

	Initial	Heater boundary	Outer boundaries
Thermal	15˚C	88.969 W/m^2	No heat flow
Hydraulic	OPA: 2 MPa pore pressure, saturation of 1 Granular bentonite: water content 5 wt% Bentonite blocks: water content 18 wt%	No flow	No flow
Mechanical	$\sigma_1 = \sigma_{zz} = 6.5$ MPa $\sigma_3 = \sigma_{xx} = 2.5$ MPa	Zero displacement	Zero displacement

4.2.4 Variant cases

The three variant cases are described below as Steps 0a to 0c. After an initial attempt at these cases, the results from the teams were very different (discussed further in Section 4.5.5), so additional cases were specified in Step 0b and Step 0c to reduce complexity and help teams develop their models.

Step 0a – Thermal (T) simulation

Only thermal processes were represented in this model. Whilst hydraulic and mechanical processes did not need to be represented, the thermal properties were made saturation dependent and saturation held at initial values.

Step 0b – Thermal-Hydraulic (TH) simulation

In this simulation, both thermal and hydraulic (two phase) processes were represented along with porosity change calculated based on pressure changes. Inclusion of vapour flow was important in this simulation. Two additional simplified cases were also carried out:

- Step 0b2: All bentonite was replaced with saturated Opalinus Clay (Figure 2) and the Opalinus Clay had a permeability of zero (or set extremely small). Pressure changes in this model reflected only the changes in water density and porosity.

Thereby water density depends on temperature and pressure, and porosity depends on pressure changes.

- Step 0b3: All bentonite was replaced with saturated Opalinus Clay and the Opalinus Clay has the permeability given in Table 4. Following from Step 0b2, this case checked that the permeability of the Opalinus Clay was implemented correctly.

For these two additional cases, temperature and pressure results were requested at the sensors outside of the tunnel only (i.e. O_1 to O_6).

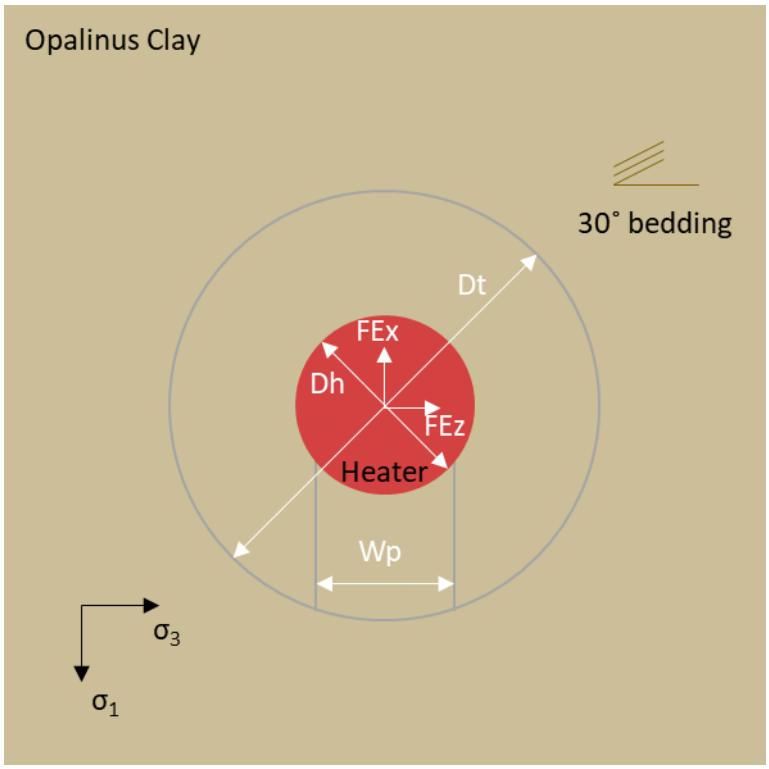

Figure 2: Geometry for cases Step 0b2, Step 0b3, Step 0c2, Step 0c3, with bentonite replaced by Opalinus Clay.

Step 0c – THM simulation

In this simulation, thermal, hydraulic (two-phase) and mechanical processes were represented. Porosity changes were calculated using the strains calculated in the mechanical equations. Linear elastic models for bentonite and Opalinus Clay were used at this stage. Two additional simplified cases were carried out:

- Step 0c2: All bentonite was replaced with saturated Opalinus Clay and the Opalinus Clay had a permeability of zero (or set to be extremely small). Pressure changes in this model reflect only the changes in water density and porosity.

Thereby water density depends on temperature and pressure, and porosity depends on pressure changes.

- Step 0c3: All bentonite was replaced with saturated Opalinus Clay and the Opalinus Clay has the permeability given in Table 4. Following from Step 0c2, this case checked that the permeability of the Opalinus Clay was implemented correctly.

For these two additional cases, temperature, pressure, stress, strain and displacement results were requested at the sensors outside of the tunnel only (i.e. O_1 to O_6).

4.3 Step 0a – Thermal simulation

This section presents the expected modelling strategy from the teams, any deviations from this strategy for each team, and compares the results from the teams.

4.3.1 Modelling strategy

The teams represented thermal conduction as:

$$C_P \rho_b \frac{\partial T}{\partial t} - \nabla \cdot (\boldsymbol{\lambda}(s) \nabla T) = Q_H \tag{1}$$

where $\boldsymbol{\lambda}(s)$ is the anisotropic thermal conductivity (W m^{-1} K^{-1}), with saturation (s) dependence given by:

$$\boldsymbol{\lambda}(s) = \boldsymbol{\lambda}_{dry} + (\boldsymbol{\lambda}_{sat} - \boldsymbol{\lambda}_{dry}) \cdot s \tag{2}$$

Heat capacity (C_p, J/K) and bulk density (ρ_b, kg m^{-3}) are also saturation dependent:

$$C_p = C_p^{solid} \cdot (1 - \phi) \cdot \frac{\rho_g}{\rho_b} + C_p^{water} \cdot \phi \cdot s \cdot \frac{\rho_w}{\rho_b} \tag{3}$$

$$\rho_b = \rho_g(1 - \phi) + \rho_w \phi s + \rho_v \phi (1 - s) F_v + \rho_a \phi (1 - s)(1 - F_v) \tag{4}$$

Some teams implemented variations on this strategy, as outlined in the following subsections.

BGR/UFZ

In OGS-5 TRM (non-isothermal Richards-mechanics), heat transport is represented as follows:

$$\underbrace{\left((1-\phi)\rho_{\mathrm{g}} C_p^{\mathrm{solid}} + \phi s \rho_{\mathrm{w}} C_p^{\mathrm{water}}\right) \frac{\partial T}{\partial t}}_{\text{heat storage}} \underbrace{-\nabla \cdot (\lambda_m \mathbf{1} \nabla T)}_{\text{conduction}} \underbrace{+ C_p^{\mathrm{water}} \boldsymbol{q}_{\mathrm{water}} \nabla T}_{\text{convection}} \underbrace{+ Q_T}_{\text{source}} = 0 \tag{5}$$

where λ_m represents the porous medium thermal conductivity (W m^{-1} K^{-1}) which is saturation-dependent as defined in Section 4.3.1. To represent anisotropic behaviour, λ_m can also take the form of a tensor.

$\mathbf{q}_{\mathrm{water}}$ represents the Darcy flow (m s^{-1}) and it can be seen that OGS takes into account heat transport due to liquid advection which is not defined by the task specification in Section 4.3.1. This is not expected to cause any differences in predicted temperatures because either the hydraulic process is disregarded (Step 0a) or no high flow velocities are expected (later steps).

All other symbols represent the same variables as defined in Section 4.3.1 and Table 4.

The first term in Eqn. (5) represents the medium/bulk heat capacity and it is saturation dependent as well. The properties of air and vapour are not taken into account in the calculation of the bulk specific heat capacity and bulk density, but it can be seen that if $\rho_v = \rho_a = 0$ is used in the equation where ρ_b is calculated, the result for the heat storage term $C_P \rho_b \frac{dT}{dt}$ is identical in OGS-5 and the task definition (Section 4.3.1). Since the air and vapour properties are taken into account in the bulk density model but not in the bulk specific heat capacity model and since the air and vapour densities are much smaller than solid and water densities, the BGR/UFZ team is confident that the differences due to this simplification made in the OGS heat transport model are negligible.

Beginning with step0b, the BGR/UFZ team switched to an OGS-6 implementation of the of the fully coupled two-component two-phase flow in deformable porous media (TH^{2}M) model (Grunwald *et al.*, 2022) in which a liquid and a gaseous phase, $\alpha \in \{\mathrm{L}, \mathrm{G}\}$, were considered explicitly. The available pore space was coupled to a deformable porous solid $\alpha \equiv \mathrm{S}$. Each fluid phase is considered a mixture of two components $\zeta \in \{\mathrm{W}, \mathrm{C}\}$. In this task modelling the FE experiment, one of the components was always water, while the other was considered as unspecified repository gas. The TH^{2}M implementation also comprised a more general energy balance expressed in terms of internal energy u_α (given in J kg^{-1}) and specific enthalpy h_α (J kg^{-1}) of each phase $\alpha \in \{\mathrm{L}, \mathrm{G}, \mathrm{S}\}$:

$$0 = \underbrace{\frac{\mathrm{d}}{\mathrm{d}t}(\Sigma_\alpha \rho_\alpha u_\alpha)}_{\text{storage}} \underbrace{+\mathrm{div}\,(\Sigma_\alpha h_\alpha \boldsymbol{A}_\alpha)}_{\text{transport by advection}} \underbrace{+\mathrm{div}\left(\Sigma_\alpha \Sigma_\zeta h_\alpha^\zeta \boldsymbol{J}_\alpha^\zeta\right)}_{\text{transport by diffusion}} + \underbrace{(\Sigma_\alpha \rho_\alpha h_\alpha)\,\mathrm{div}\left(\frac{\mathrm{d}\boldsymbol{u}_S}{\mathrm{d}t}\right)}_{\text{medum volume change}} \underbrace{-\Sigma_\alpha \boldsymbol{g} \cdot \boldsymbol{A}_\alpha}_{\text{gravitation work}} \underbrace{-\mathrm{div}\,(\boldsymbol{\lambda}_{\mathrm{eff}}\,\mathrm{grad}\,T)}_{\text{heat conduction}} \quad (6)$$

where ρ_α represents the apparent density of a phase in the porous medium with $\rho_\mathrm{L} = \phi S_\mathrm{L} \rho_\mathrm{LR}$ and $\rho_\mathrm{G} = \phi(1 - S_\mathrm{L})\rho_\mathrm{GR}$ and $\rho_\mathrm{S} = (1 - \phi)\rho_\mathrm{SR}$ (kg m^{-3}). The effective medium thermal conductivity is given by a porosity-saturation based mixing rule with

$$\boldsymbol{\lambda}_{\mathrm{eff}} = (1-\phi)\boldsymbol{\lambda}_{\mathrm{S}} + \phi(S_{\mathrm{L}}\boldsymbol{\lambda}_{\mathrm{L}} + (1-S_{\mathrm{L}})\boldsymbol{\lambda}_{\mathrm{G}}) \quad (7)$$

where $\boldsymbol{\lambda}_{\mathrm{S}}$, $\boldsymbol{\lambda}_{\mathrm{G}}$ and $\boldsymbol{\lambda}_{\mathrm{L}}$ are the solid, gaseous and liquid phase thermal conductivity tensors (all in W m^{-1} K^{-1}).

CAS

In CASRock, the heat conduction part of the energy balance equation is represented as follows:

$$\rho_b c_p \dot{T} - \nabla(\lambda \nabla \mathrm{T}) = q_T \quad (8)$$

where ρ_b, c_p and λ are the same as defined by the task specification. In the CAS model, the heat source is a body (volumetric) heat source. But the heat source in the actual task (as specified for Step 0, Section 4.2.3) is a surface heat source, so a thin-walled cylindrical heater was adopted to achieve the effect of a surface heat source using a body heat source. Therefore, the heat source term q_T is measured in $\mathrm{W/m^3}$, and its value depends on the thickness of the thin wall. This approach has been compared to using a surface heat source and, for a thin-walled body heat source, the results for this step were expected to be the same.

DOE/SNL

The conduction part of the energy equation in PFLOTRAN is given as:

$$\frac{\partial}{\partial t}\Big((1-\phi)\rho_r C_p T\Big) - \boldsymbol{\nabla}\cdot(\kappa \boldsymbol{\nabla} T) = Q \quad (9)$$

where ϕ is porosity, ρ_r is rock grain density (kg m^{-3}), C_p is rock heat capacity (J/K) and κ is saturation dependent rock thermal conductivity (W m^{-1} K^{-1}). PFLOTRAN allows the input of energy flux (MW/m^2) to be applied to the heater surface. This feature was applied to Step 0 simulations where heat was applied to the surface of the heater. The Task C specified thermal conductivity-saturation equation (Eqn. (2)) was implemented in PFLOTRAN, and thus was used for Step 0. The heat capacity is a constant value in PFLOTRAN.

4.3.2 Results

Temperature results from the Opalinus Clay are shown in Figure 3, with close agreement, within 1˚C, between all teams. SNL (PFLOTRAN) show a more rapid increase in temperature at O_1 which could be attributed to a combination of the constant heat capacity and grid related differences between the actual output location and the desired output location.

In the bentonite (Figure 4) there is also close agreement between the majority of the teams, but CAS, LBNL and SNL get slightly different results. This is likely due to the location of output points for LBNL, potentially due to the heater representation for CAS and potentially due to the constant heat capacity for SNL.

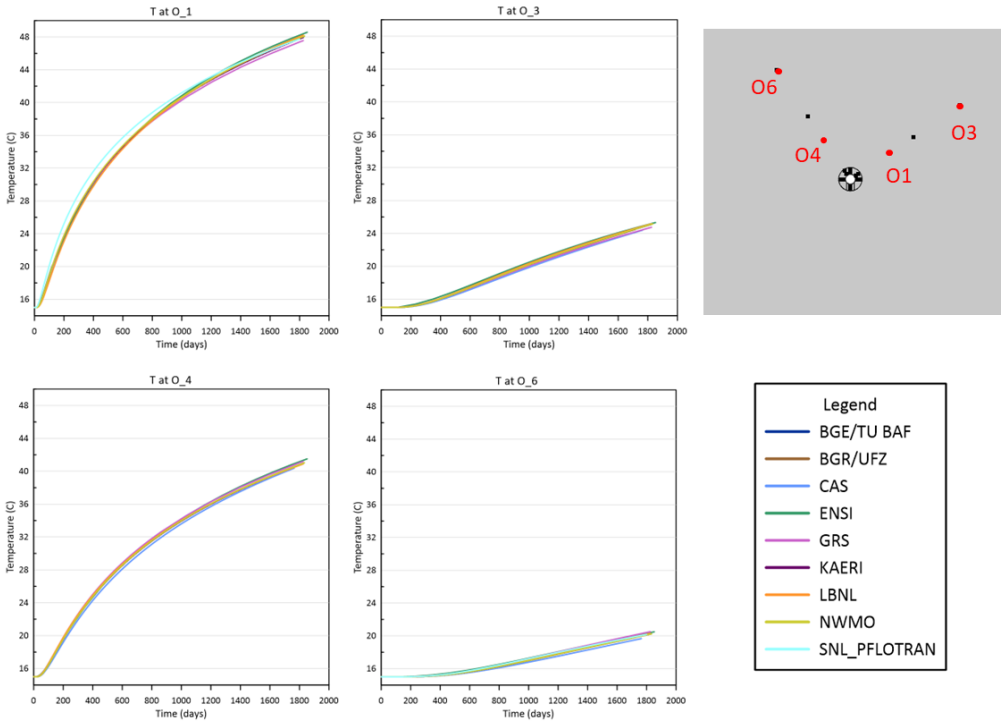

Figure 3: Selected temperature results for locations in the Opalinus Clay from Step 0a.

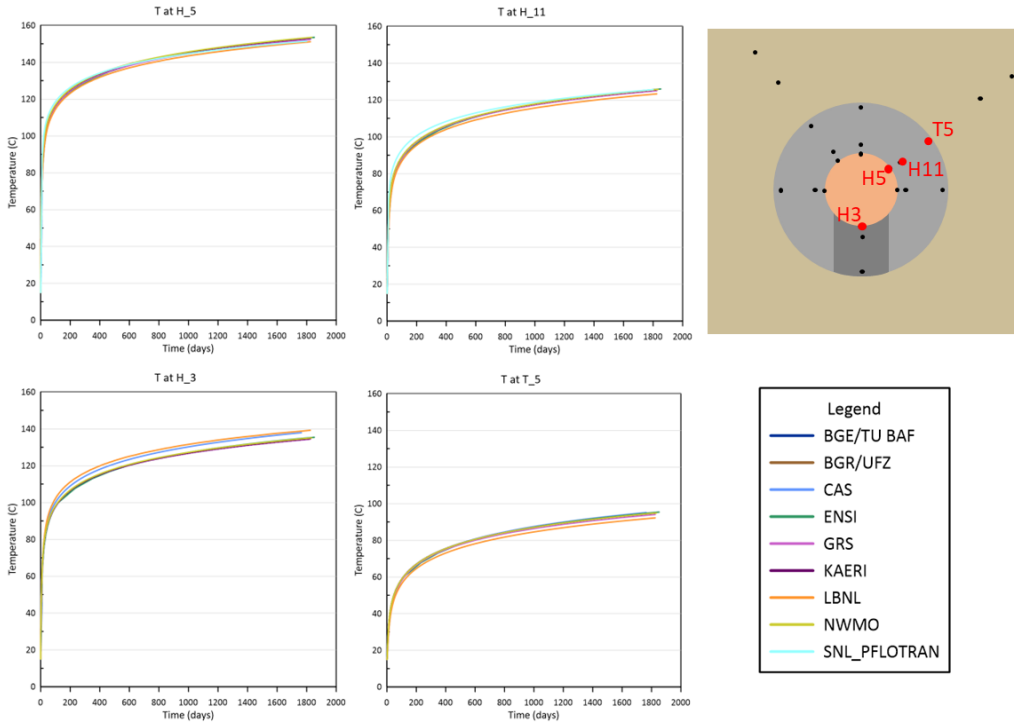

Figure 4: Selected temperature results for locations in the bentonite from Step 0a.

4.3.3 Discussion

In this simple case, representing thermal conduction with three different materials and anisotropy of thermal conductivity in the Opalinus Clay, the modelling teams achieved good agreement as expected. All teams covered the anisotropy of the heat conductivity in the Opalinus Clay, which can clearly be seen at the higher temperatures parallel to bedding (O1, O3) compared to perpendicular to bedding (O2, O4). Based on the results, the teams can be confident of the implementation of the relevant thermal processes in the models.

4.4 Step 0b – Thermal-Hydraulic simulation

4.4.1 Modelling strategy

The equations to describe heat flow and thermal properties are as described in Step 0a. This assumes that convection is not a significant process in the low permeability Opalinus Clay.

The hydraulic equation must account for Darcy flow of liquid water, advection and diffusion of vapour and changes in porosity, water density and saturated vapour density. Teams represented hydraulic processes as follows, assuming zero volume change (V, m^3):

$$\frac{1}{V}\frac{dm}{dt} = \frac{\partial(\phi s\rho_w + \phi(1-s)\rho_v)}{\partial t} = -\nabla\cdot(\rho_w \boldsymbol{q_l} + \rho_v \boldsymbol{q_v}) \quad (10)$$

where the liquid water flows ($\boldsymbol{q_l}$, $m^3\ s^{-1}$) are given by Richards' Equation:

$$\boldsymbol{q_l} = -\frac{\boldsymbol{\kappa}}{\mu}(\nabla p - \rho_w \boldsymbol{g}) \quad (11)$$

and vapour flows ($\boldsymbol{q_v}$, $m^3\ s^{-1}$) are given by vapour diffusion:

$$\boldsymbol{q_v} = -D_v\left(\nabla\left(\frac{\rho_v}{\rho_v^{sat}}\right)\right) \quad (12)$$

Gas advection was not included by most teams as it was thought to have a small effect.

Capillary pressure (P_c, MPa) and relative permeability (k_{rel}) are given by van Genuchten's equations:

$$s_c = \left(\frac{1}{1+(P_e P_c)^n}\right)^m \quad (13)$$

where $m = 1-\frac{1}{n}$; $s_c = \frac{s-s_r}{s_{max}-s_r}$

$$k_{rel} = s_c^{\frac{1}{2}}\left[1-\left(1-s_c^{\frac{1}{m}}\right)^m\right]^2 \quad (14)$$

Water density (ρ_w, $kg\ m^{-3}$) depends on both pore pressure and temperature:

$$\rho_w = \rho_w^0 \frac{1}{e^{\alpha_w (T - T_0)} e^{c_{fluid}(p_0 - p)}} \tag{15}$$

where α_w (K^{-1}) is the linear thermal expansion coefficient of water, specified as a constant in Table 4. Some teams also investigated the effect of a temperature-dependent thermal expansion coefficient of water, discussed in Section 4.4.5.

Water viscosity (μ, Pa s) is temperature dependent (Sharqawy *et al*., 2010):

$$\mu = 4.2844 \cdot 10^{-5} \mathrm{Pa \cdot s} + \left[0.157 \left(\frac{\mathrm{T} - 273.15 \mathrm{K}}{K} + 64.993 \right)^2 - 91.296 \right]^{-1} \mathrm{Pa \cdot s} \tag{16}$$

Vapour density (ρ_v, kg m^{-3}) is given by the temperature dependent saturated vapour density ρ_v^{sat} (Rutqvist, Noorishad and Tsang, 1999) multiplied by the relative humidity RH (Rutqvist, Noorishad and Tsang, 1999; Philip and de Vries, 1957; Edlefsen and Anderson, 1943 pg 260):

$$\rho_v^{sat} = 10^{-3} \mathrm{kg\ m^{-3}}\ e^{(19.891 - 4975.9\ \mathrm{K}/T)} \tag{17}$$

$$RH = e^{p/(\rho_w R T / M_w)} \tag{18}$$

Porosity changes due to water pressure changes are calculated as:

$$\phi = \phi_0 \left(1 + c_{pore}(p_w - p_{w0}) \right) \tag{19}$$

with pore compressibility given by (Settari and Mourits, 1998):

$$c_{pore} = \frac{1}{K \phi_0} \left(1 - \frac{2(1 - 2\nu_{av})}{3(1 - \nu_{av})} \right) \tag{20}$$

$$K = \frac{E_{av}}{3(1 - 2\nu_{av})} \tag{21}$$

With average Poisson's ratio $\nu_{av} = \sqrt[3]{\nu_\parallel \nu_\parallel \nu_\perp}$ and average Young's Modulus $E_{av} = \sqrt[3]{E_\parallel E_\parallel E_\perp}$.

Not all teams chose to implement the equations in this way, so alternative modelling strategies were considered as described in the following subsections.

BGE/TUBAF

BGE/TUBAF used the same set of equations as given in Section 4.5 but suppressing displacements on the entire domain. The TRM (non-isothermal Richards-mechanics) model can be condensed into a TR formulation by taking into account various kinematic assumptions such as no expansion, free expansion, uni-axial expansion, with or without expansive grains (Buchwald *et al*. 2021, 2024).

BGR/UFZ

The numerical model employed by BGR/UFZ was the non-isothermal two-phase two-component flow in deformable porous media (TH^2M) presented by Grunwald *et al*. (2022). It was implemented in the open-source finite element code OpenGeoSys-6 (Bilke *et al.,* 2019). Therefore, and in contrast to the general modelling strategy described in section 4.4.1, a mass balance for the gaseous component was calculated in addition to the water component mass balance. The component-wise formulation allows the consideration of phase transitions (dissolution or out-gassing of the gaseous component into and out of the liquid phase as well as evaporation or condensation of the water component into and out of the gas phase).

In Pitz *et al*. (2023), it is shown that the water-component mass balance equation collapses and becomes equivalent to the water mass balance expressed by the Richards equation. In their fully expanded form, the component mass balance equations are obtained by substituting $\zeta \equiv \mathrm{W}$ for the water component and $\zeta \equiv \mathrm{C}$ for the gaseous component in the following equation:

$$0 = \frac{\mathrm{d}\left(\phi \rho_{\mathrm{F}}^{\zeta}\right)}{\mathrm{d}t} + \phi \rho_{\mathrm{F}}^{\zeta} \mathrm{div}\left(\frac{\mathrm{d}\boldsymbol{u}_{\mathrm{S}}}{\mathrm{d}t}\right) + \mathrm{div}\left(\boldsymbol{A}^{\zeta} + \boldsymbol{J}^{\zeta}\right) \tag{22}$$

Where $\rho_{\mathrm{F}}^{\zeta} = (1 - S)\rho_{\mathrm{G}}^{\zeta} + S\rho_{\mathrm{L}}^{\zeta}$ represents the effective density of component ζ across the two fluid phases (kg m^{-3}), ϕ designates the medium porosity and $\boldsymbol{u}_{\mathrm{S}}$ is the solid displacement vector (m). The above equation utilises a linearisation around the reference deformation state of the medium. Mass transfer occurs via advection and diffusion in both fluid phases. A consequence of this formulation is that the water component in the form of vapour can be advected in the gas phase – this is a difference to the Richards formulation given in section 4.4.1. In order to simplify the numerical model, the dissolution of the gaseous component into the liquid phase was neglected and only water vaporisation was considered in terms of phase changes. Advection $\boldsymbol{A}^{\zeta}$ (kg s^{-1} m^{-2}) in each phase is described by a modified Darcy law similar to eq. (9). Diffusion

is expressed by means of mass fractions as opposed to the formulation based on vapour density:

$$\boldsymbol{J}^{\zeta} = -\rho_{\mathrm{G}}\, \boldsymbol{D}_{\mathrm{G}}^{\zeta}\, \mathrm{grad}\, x_{\mathrm{m,G}}^{\zeta} \tag{23}$$

Here, ρ_{G} represents the gas phase density (kg m^{-3}) and $\boldsymbol{D}_{\mathrm{G}}^{\zeta}$ (m² s^{-1}) is the tensor describing the diffusion coefficient of water vapour in air. $x_{\mathrm{m,G}}^{\zeta}$ (-) is the mass fraction of component ζ in the gas phase. A detailed evaluation and comparison of the diffusion formulations based on mass fraction and vapour density is conducted in the Appendix of Pitz *et al*. (2023).

The porosity evolution was defined in accordance with the task definition (Section 4.4.1). Thus, one can conclude that the two-phase two-component formulation constitutes a difference to the Richards formulation (foremost due to the explicit consideration of the gas phase), but in the modelling of the FE experiment, the significant hydraulic processes in the water phase were represented similarly to the DECOVALEX 2023 Task C definitions.

A difference between the TH^{2}M implementation in OGS-6 and the task definition is the water density model, which is realised in the present case using a linear model. Figure 5 illustrates a comparison of the relative pore water density change obtained by the linear model and by the exponential model given in the task definition. It became clear that any differences between the two models in the interval between 0 and 10 MPa pore water pressure are negligible and differences in the interval between 20 and 150 °C temperature are in the range of 0.1%.

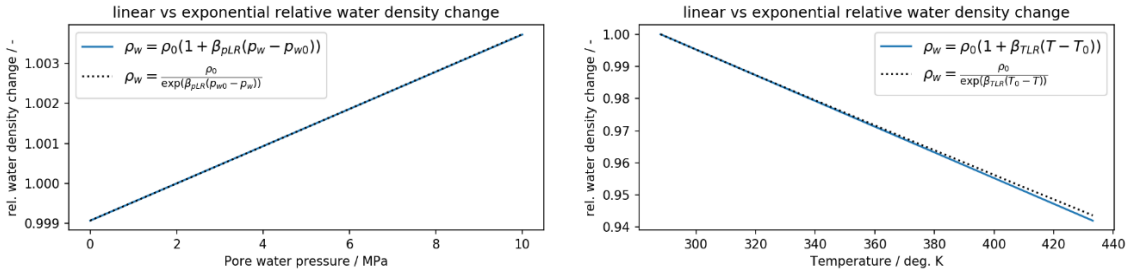

Figure 5: Comparison of the linear and exponential water density models

To improve TH2M coupling in later steps, BGR/UFZ switched the numerical code from OGS-5 to OGS-6 during the period between the interim and final task reports (Bilke *et al*. (2019); Grunwald *et al*. (2022)). As briefly discussed by Pitz *et al*. (2023), in the special case of full saturation, the equations governing the TH^{2}M water mass balance reduces to a THM model. Results obtained by OGS-6 TH^{2}M for cases 0-b2 and 0-b3 have been

submitted and agree nearly perfectly with results by OGS-5 submitted previously and the semi-analytical solution discussed below (Eqn. (27)).

CAS

In CASRock, the water mass balance equation of hydraulic part is represented as follows:

$$\phi\left[\frac{\rho_w-\rho_v}{\rho_w}\frac{\partial\theta}{\partial p}+(1-\theta)\frac{\rho_v}{\rho_w^2 RT}\right]\frac{\partial P}{\partial t}+\theta\left(\phi\beta_{fluid}+(\alpha-\phi)\beta_{solid}\right)\frac{\partial p}{\partial t}+\nabla \cdot\frac{q_w+q_v}{\rho_w} + \phi\frac{(1-\theta)}{\rho_w}\left(RH\frac{\partial\rho_{vS}}{\partial T}+\frac{\rho_v p}{\rho_w^2 RT^2}\right)\frac{\partial T}{\partial t} - (\phi\theta\alpha_w+(\alpha-\phi)\alpha_T)\frac{\partial T}{\partial t}=0 \quad (24)$$

where ϕ is porosity, θ is liquid water saturation, β_{fluid} is fluid compressibility (Pa^{-1}), β_{solid} is solid compressibility (Pa^{-1}), ρ_{vS} is saturated vapour density (kg m^{-3}), α_w is thermal expansion of water (Pa s) and α_T is thermal expansion of solid (K^{-1}). In addition, all the equations in the task specification (Section 4.4.1) were considered.

GRS

For GRS the approach of pore compressibility and porosity change due to water pressure change caused some issues. The THM approach of CODE_BRIGHT considers porosity variation as a mechanical effect induced by volumetric strains and/or solid density variation. This approach doesn't include porosity changes due to hydraulics and thus, a term for pore compressibility or storativity as used in this benchmark for the TH simulation was not implemented.

Due to the missing pore compressibility, GRS' liquid pressures in the TH-coupled simulation were much higher than the project partner ones, however. Therefore, the GRS results are not shown in the comparison plots for this modelling step. In general, the quantitative trend for GRS' liquid pressure results was in good agreement with the project partner ones.

Additionally, the approach of a constant vapour diffusivity coefficient D_v is not consistent with the basics of CODE_BRIGHT, where the vapour diffusivity coefficient depends on temperature and gas pressure (Eqn. (25)). Since gas pressure was kept

constant in the simulation (P_g = 0.1 MPa), only the dependence on temperature remains and causes some differences.

$$D_v = D_{v,0}\left(\frac{(273.15+T)^n}{P_g}\right) \quad (25)$$

$D_{v,0}$ = initial value for the vapour diffusivity coefficient ($m^2\ s^{-1}$), T = temperature (°C), n = parameter.

Figure 4-6 shows the evolution of the vapour diffusivity coefficient with temperature for the specified value by the task, the default option in CODE_BRIGHT and an adjusted value of $D_{v,0}$ = 4e-6 $m^2\ s^{-1}$. With the adjusted option, the differences were diminished to a minimum.

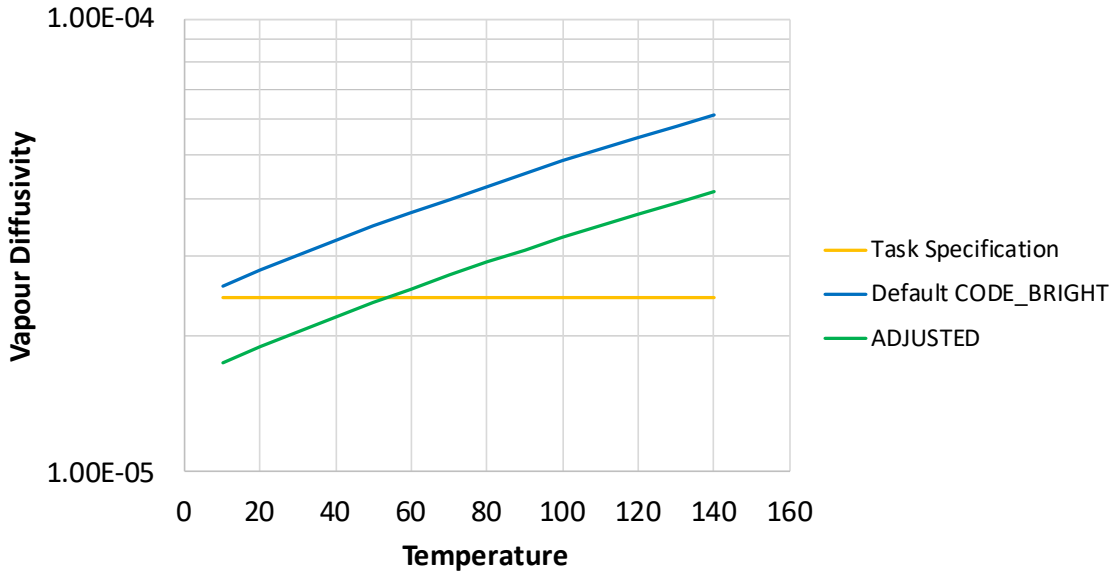

Figure 6: Vapour diffusivity coefficient as specified by the task, as default implementation in CODE_BRIGHT and the adjusted version

DOE/SNL

The SNL-PFLOTRAN team used PFLOTRAN with the General Mode, which calculates the strongly coupled flow and energy equations. No approximations such as Richards' equations were used. The van Genuchten capillary pressure and relative permeability equations (Eqn.s (13) and (14)) are also in PFLOTRAN. PFLOTRAN uses equation of state (EoS) to evaluate water properties (Hammond et al., 2014). Many of the material properties are also different from those specified for Task C. The SNL-PFLOTRAN team worked with PFLOTRAN developers to include Task C specified material and fluid

property equations into PFLOTRAN. As a result, thermal conductivity (Eqn. (2)), water density (Eqn. (15)), relative humidity (Eqn. (18)), and porosity (Eqn. (19)) have been incorporated into PFLOTRAN.

The Task C specified porosity vs pore compressibility equation (Eqn. (19)) is slightly different from that in PFLOTRAN. The equation in PFLOTRAN is:

$$\varphi = \varphi_0 + c_{pore}(p_w - p_{w0}) \tag{26}$$

where φ is porosity and φ_0 is initial porosity (-);

c_{pore} is pore compressibility (Pa^{-1});

p_w is water pressure and p_{w0} is initial water pressure (Pa).

Equation (26) can represent Equation (19) with some input manipulations. The value for the soil compressibility entered was the pore compressibility defined in Table 4 multiplied by the initial porosity.

Some of the Task C specified property equations were not implemented with PFLOTRAN at the time. These included material heat capacity (Eqn. (3)), water viscosity (Eqn. (16)), and vapor density (Equation 15). In PFLOTRAN a constant material heat capacity was used, and water viscosity and vapor density were obtained from the EoS. As a result, it was expected that modelling results will be affected by these omissions.

4.4.2 Results 0b2

The first simplified case, with no bentonite and no flow in the Opalinus Clay gave temperature results that are consistent with Step 0a (Figure 7).

Due to the simplifications in this model, an analytic solution is available for pressure if the temperature is known. The temperature used in the analytical solution is marked as analytic on Figure 7. The analytical solution for pressure was derived by BGR/UFZ as:

$$p_w[\mathrm{Pa}] = p_{w0} + \alpha_w(T - T_0) \cdot \left(c_{fluid} + c_{pore}\right)^{-1} \tag{27}$$

and results for this analytic solution are shown on Figure 8 labelled analytic.

Most teams yielded good agreement with the analytic solution (Figure 8).

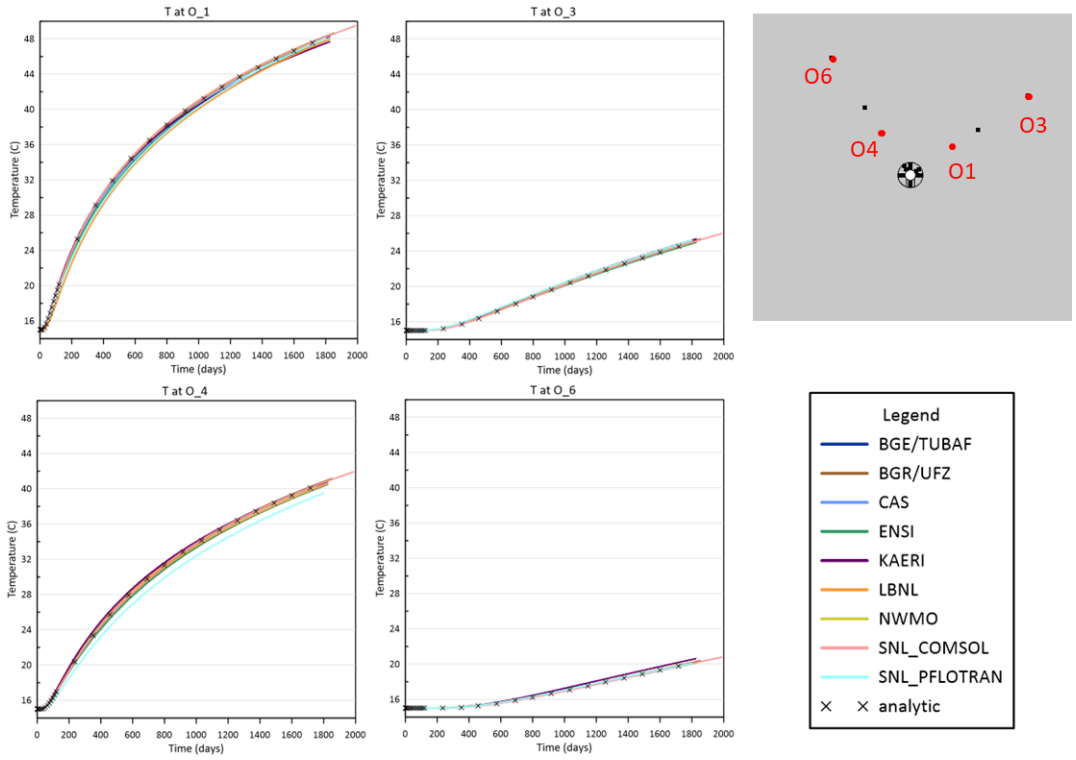

Figure 7: Selected temperature results for locations in the Opalinus Clay from Step 0b2.

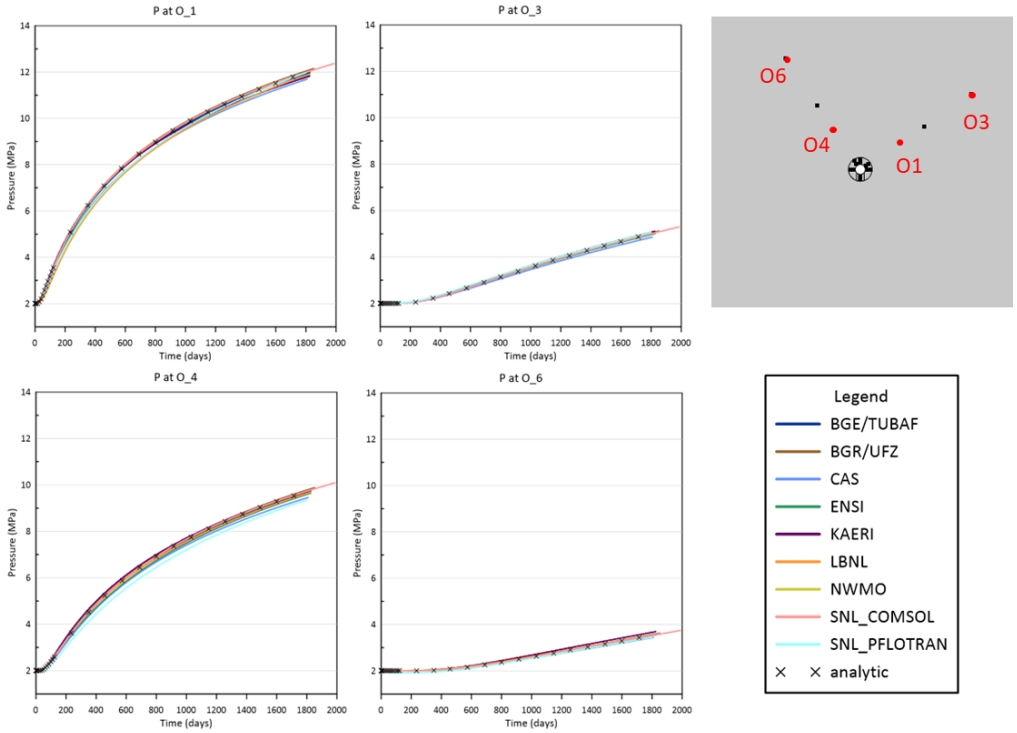

Figure 8: Selected pressure results for locations in the Opalinus Clay from Step 0b2.

4.4.3 Results 0b3

This second simplified case, with no bentonite but with a non-zero permeability in the Opalinus Clay, gave temperature results that were very similar to case 0b2 (and are therefore not shown), which was unsurprising as the Opalinus Clay is saturated so there is no change in the thermal properties.

The pressure results for most teams were also consistent with case 0b2, with pressures generally being lower than case 0b2 because water can flow in the Opalinus Clay (Figure 9).

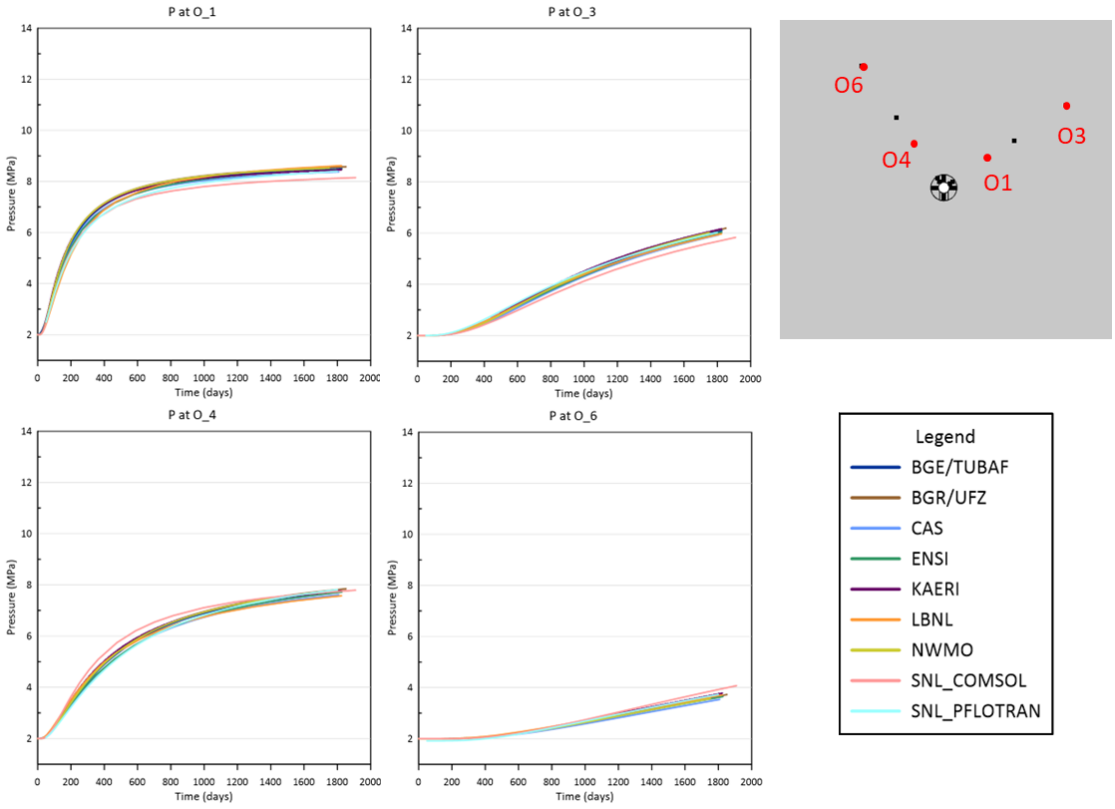

Figure 9: Selected pressure results for locations in the Opalinus Clay from Step 0b3.

4.4.4 Results 0b

Results from the TH model including bentonite within the FE tunnel show more spread across the teams than the simpler cases. For temperature results in the Opalinus Clay, the teams agree closely (Figure 10).

Temperature results within the bentonite vary more widely amongst the teams (Figure 11), but this does not significantly impact the results in the Opalinus Clay. This is because the total heat flux into the Opalinus Clay is the same as the output from the heater at (quasi-) steady state, so the distribution of temperature is defined by the thermal properties of the Opalinus Clay.

Pressure results in the Opalinus Clay (Figure 12) are less consistent than in the simpler cases, 0b2 and 0b3, but teams still agree reasonably closely.

There is some variation between the teams in the relative humidity within the bentonite (Figure 13), likely due to different implementations of saturation dependent parameters and vapour flows, including whether advective gas flow has been included, and representation of water density. There is no apparent correlation between teams with similar relative humidity and teams with similar pressure in the Opalinus Clay, which indicates that pressure in the Opalinus Clay is not strongly affected by the relative humidity of the bentonite.

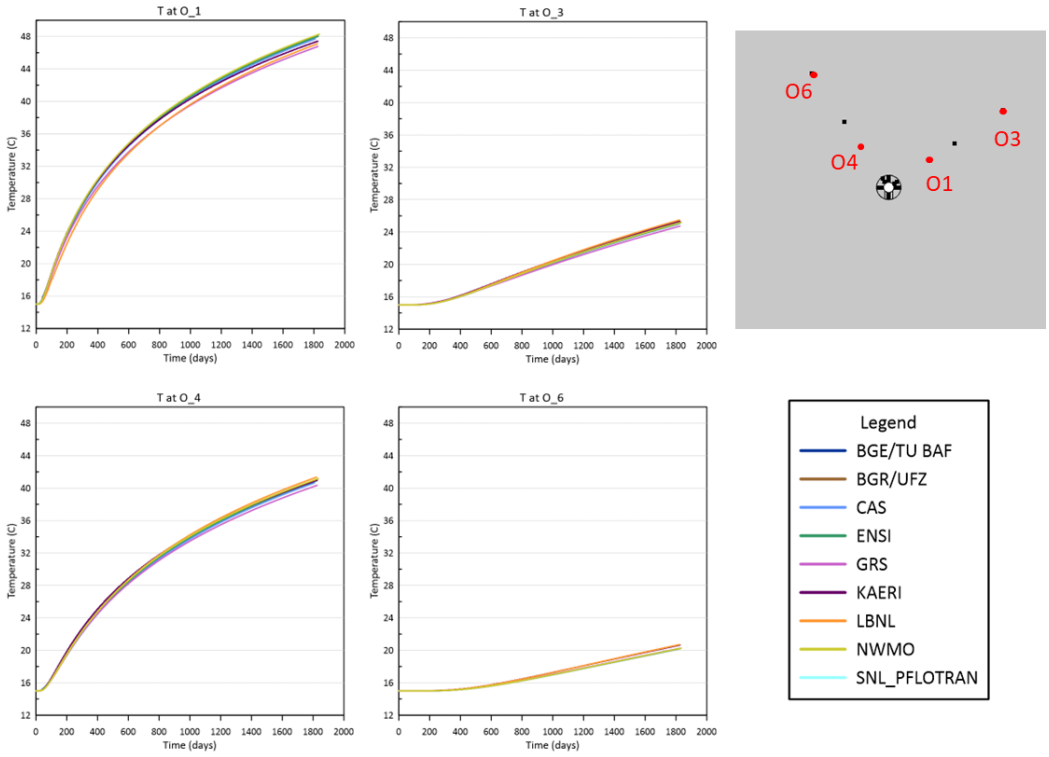

Figure 10: Selected temperature results for locations in the Opalinus Clay from Step 0b.

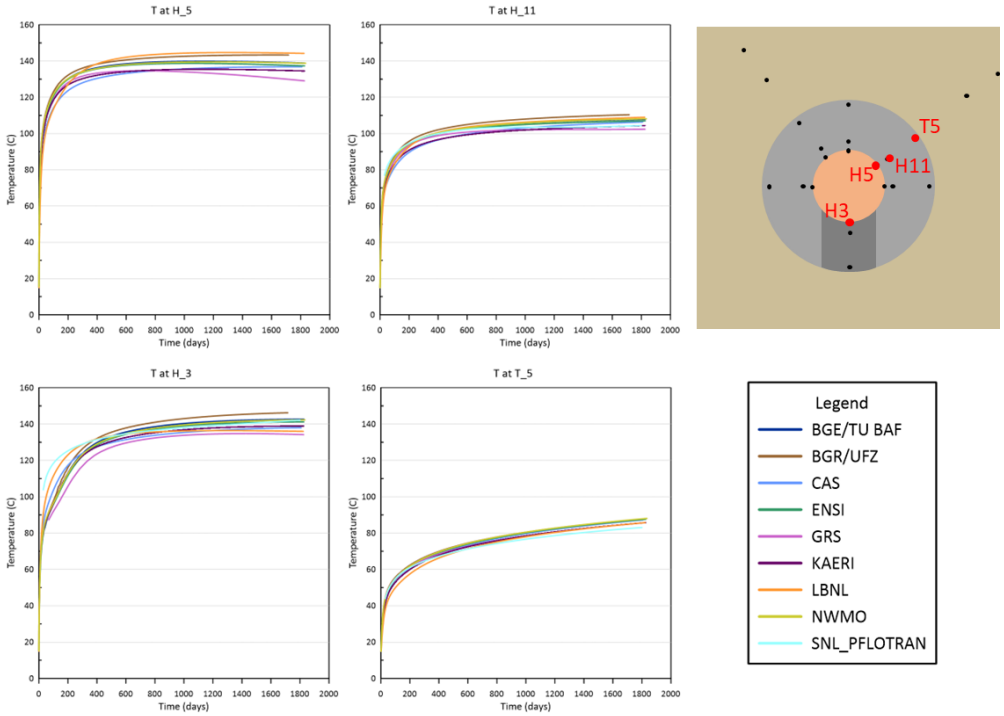

Figure 11: Selected temperature results for locations in the bentonite from Step 0b.

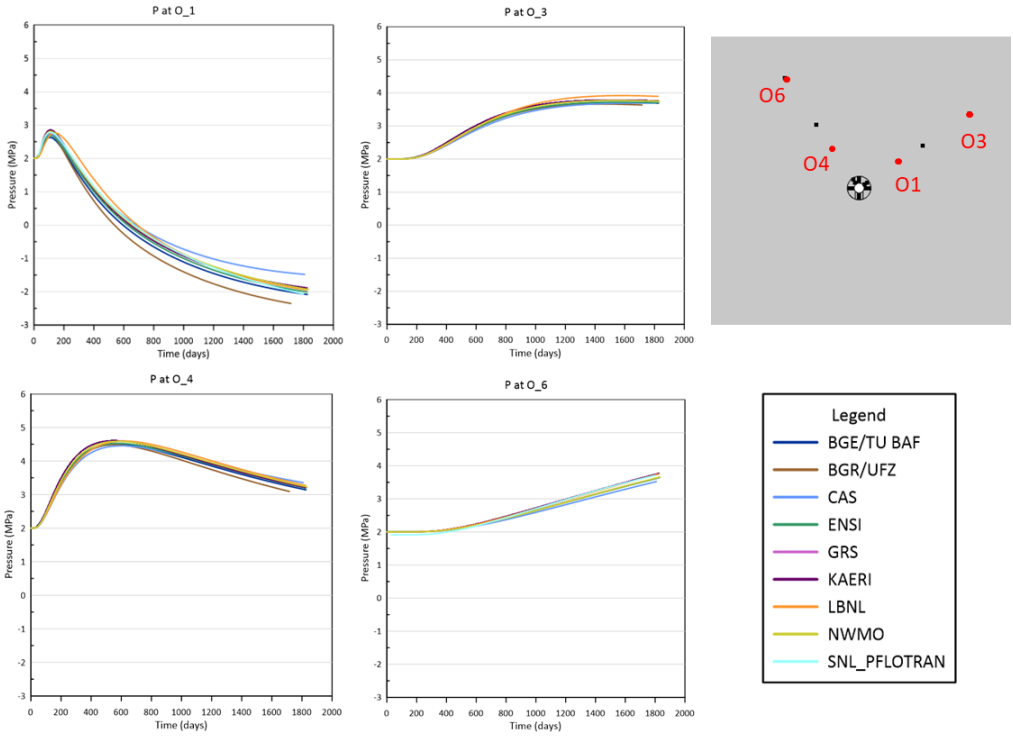

Figure 12: Selected pressure results for locations in the Opalinus Clay from Step 0b.

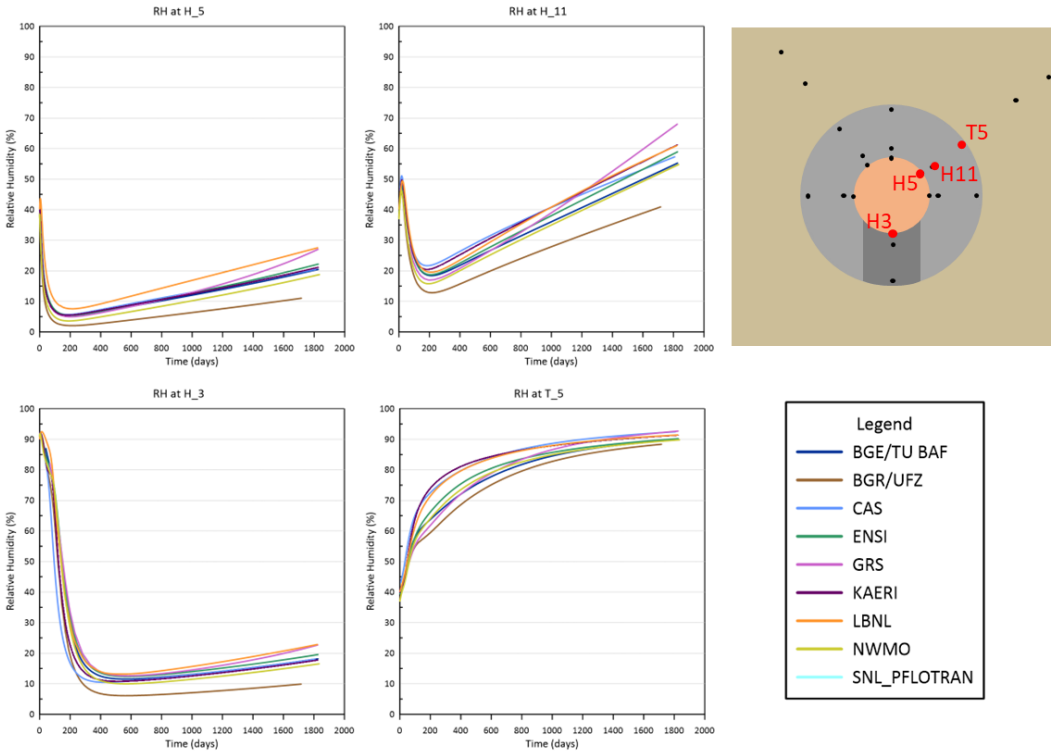

Figure 13: Selected relative humidity results for locations in the bentonite from Step 0b.

4.4.5 Discussion

The addition of hydraulic processes to this model was a significant change in the complexity of the model. In this task, we were primarily concerned with pore pressure generation in the Opalinus Clay and the teams achieved reasonably consistent implementations of the specification. Not all codes had the flexibility to implement a given set of equations. Therefore, not all teams could provide results for the TH simulation.

Sensitivity to Thermal Expansion Coefficient of Water

Several teams demonstrated the sensitivity of the results to the thermal expansion coefficient of water. For the simplified cases in Step 0, teams assumed a constant thermal expansion coefficient of water as specified in Table 4. However, the thermal expansion coefficient will have a temperature dependency that teams could choose to include in later steps.

BGR/UFZ calculated a semi-analytical solution for pore water pressure in the simplified case of Step 0b2 (as in Equation (28)) with a linear coefficient of thermal expansion of water, $\alpha_w(T) = \alpha_{w0} + f(T - T_0)$ using the trapezoidal rule and with f as a constant factor:

$$p_w[\mathrm{Pa}] = p_w^0 + \left(c_{fluid} + c_{pore}\right)^{-1}(T - T_0)\frac{1}{2}(\alpha_{w0} + \alpha_{w0} + f(T - T_0)) \qquad (28)$$

Simandoux (2015) gives a relation for the temperature dependency of the thermal expansion coefficient of water, which was used to approximate a linear expression for $a_w(T)$ (K^{-1}) (Figure 14).

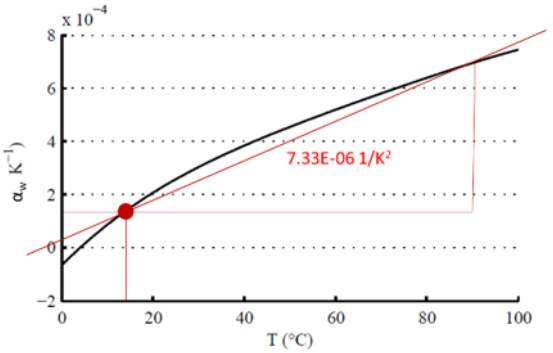

Figure 14: Coefficient of thermal expansion of water as a function of temperature from Simandoux (2015), with linear approximation in red.

The resulting semi-analytical pore pressures calculated for Step 0b2 are shown in Figure 15, compared with the equivalent semi-analytical results using a constant thermal expansion coefficient of water from Figure 7. With this parameterisation, the calculated pore pressures are lower with the linear thermal expansion coefficient, but this will be affected by the temperature dependence assumed.

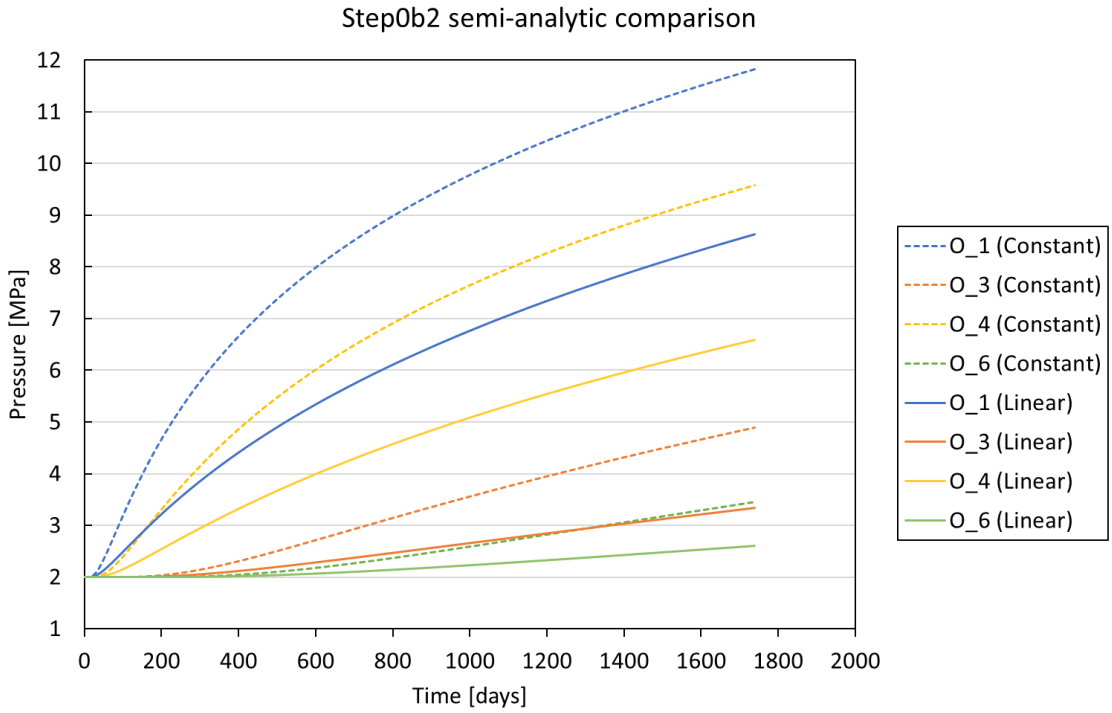

Figure 15: Comparison of semi-analytical solutions for pore pressure in Step 0b2, using a constant or linearly temperature dependent thermal expansion coefficient of water. Plotted for observation points O1-O6.

Other teams including NWMO, SNL and LBNL produced results with and without a temperature-dependent thermal expansion coefficient of water. For the purposes of comparison across the teams, the results with a simple constant coefficient have been used in this report. However, as teams moved to less tightly specified steps in this task, they could choose to include temperature dependency in the thermal expansion coefficient of water. This could be achieved by non-linear temperature dependence of the water density model.

4.5 Step 0c – Thermal-Hydraulic-Mechanical simulation

4.5.1 Modelling strategy

The thermal equation solved in Step 0a remained unchanged in Step 0c.

The hydraulic equations solved largely remained unchanged, but the volume of the material could now change given that mechanical calculations were now included:

$$\frac{1}{V}\frac{dm}{dt} = \frac{1}{V}\frac{d(V\phi s\rho_w + V\phi(1-s)\rho_v)}{dt} = -\nabla\cdot(\rho_w \boldsymbol{q_l} + \rho_v \boldsymbol{q_v}) \tag{29}$$

with parameters as defined in Table 4 and other variables defined in Section 4.4.1.

The porosity ϕ could also be calculated based on volumetric strain ε_{vol}, assuming that the solid grains are incompressible (this was an approximation since thermal expansion of the medium was included in this step, as in Eqn. (33)). Some teams took into account the full solid mass balance including thermal expansion, e.g. Eqns. (31,43)):

$$\phi = 1 - \frac{(1-\phi_0)}{(1+\varepsilon_{vol})} \tag{30}$$

Mechanical equations represent the conservation of momentum:

$$\rho_b \frac{\partial^2 \boldsymbol{u}}{\partial t^2} = \nabla\cdot\overline{\boldsymbol{\sigma}} + \rho_b \boldsymbol{g} \tag{31}$$

where $\boldsymbol{u}$ (m) is displacement and $\boldsymbol{g}$ is acceleration due to gravity, with a Biot effective stress defined when water pressure is positive ($\overline{\boldsymbol{\sigma}}$ (Pa) is total stress, where positive stress is compressive) as:

$$\overline{\boldsymbol{\sigma}} = \bar{\mathbf{C}}\colon(\boldsymbol{\varepsilon} - \boldsymbol{\varepsilon}_{th}) - \alpha\max(p_w - p_w^0, 0)\bar{\boldsymbol{I}} \tag{32}$$

where $\bar{\mathbf{C}}$ is the stiffness tensor, α is the Biot coefficient and $\boldsymbol{I}$ is the unity matrix.

Thermal expansion $\boldsymbol{\varepsilon_{th}}$ is given by:

$$\boldsymbol{\varepsilon}_{th} = \boldsymbol{\alpha}_T(T - T_0)\,\bar{\boldsymbol{I}} \tag{33}$$

Some teams implemented variations on this strategy, as described in the following subsections.

The basic equations used in OGS-6 TRM are listed here for comparison (these do not represent the complete set). Definitions are provided in Pitz *et al*. (2023).

The energy balance is as follows:

$$0 = \left(\rho c_p\right)_{\mathrm{eff}} T_S' - \nabla \cdot (\boldsymbol{\lambda}_{\mathrm{eff}} \nabla T) + \left(c_{p\mathrm{L}} \rho_{\mathrm{LR}} \widetilde{\boldsymbol{\omega}}_{\mathrm{vap,S}} + c_{p,\mathrm{vap}} \rho_{\mathrm{vap}} \widetilde{\boldsymbol{\omega}}_{\mathrm{vap,S}}\right) \cdot \nabla T \tag{34}$$

The mass balance is as follows:

$$\begin{aligned} 0 = {} & \left(\rho_{\mathrm{LR}} - \rho_{\mathrm{vap}}^{\mathrm{W}}\right)\left[\phi - p_{\mathrm{cap}} S_{\mathrm{L}} (\alpha_B - \phi) \beta_{p,\mathrm{SR}}\right] (S_{\mathrm{L}})_{\mathrm{S}}' \\ & + \rho_{\mathrm{LR}} S_{\mathrm{L}} \left[\phi \beta_{p,\mathrm{LR}} + S_{\mathrm{L}} (\alpha_{\mathrm{B}} - \phi) \beta_{p,\mathrm{SR}}\right] (p_{\mathrm{LR}})_{\mathrm{S}}' \\ & + \phi \left[(1 - S_{\mathrm{L}}) \frac{\partial \rho_{\mathrm{vap}}^{\mathrm{W}}}{\partial p_{\mathrm{LR}}}\right] (p_{\mathrm{LR}})_{\mathrm{S}}' + \nabla \cdot \left(\rho_{\mathrm{LR}} \widetilde{\boldsymbol{\omega}}_{\mathrm{LS}} + \rho_{\mathrm{vap}}^{\mathrm{W}} \widetilde{\boldsymbol{\omega}}_{\mathrm{vap,S}}\right) \\ & + S_{\mathrm{L}} \varrho_{\mathrm{LR}} \alpha_{\mathrm{B}} \nabla \cdot \boldsymbol{u}_{\mathrm{S}}' \\ & + \left[\phi (1 - S_{\mathrm{L}}) \frac{\partial \rho_{\mathrm{vap}}^{\mathrm{W}}}{\partial T} - \rho_{\mathrm{LR}} S_{\mathrm{L}} \left[\phi \beta_{T,\mathrm{LR}} + (\alpha_{\mathrm{B}} - \phi) \boldsymbol{\alpha}_{T,\mathrm{SR}} : \mathbf{I}\right]\right] T_{\mathrm{S}}' \end{aligned} \tag{35}$$

Where vapour transport is given by:

$$\widetilde{\boldsymbol{\omega}}_{\mathrm{vap,S}} = -D_{v,\mathrm{eff}} \nabla \rho_{\mathrm{vap}}^{\mathrm{W}} = -D_{v,\mathrm{eff}} \left(\frac{\partial \rho_{\mathrm{vap}}^{\mathrm{W}}}{\partial p_{\mathrm{LR}}} \nabla p_{\mathrm{LR}} + \frac{\partial \rho_{\mathrm{vap}}^{\mathrm{W}}}{\partial T} \nabla T\right) \tag{36}$$

And vapour diffusivity is:

$$D_{v,\mathrm{eff}} = \phi (1 - S_{\mathrm{L}}) D_v \tag{37}$$

The linear momentum balance is:

$$0 = \nabla \cdot (\boldsymbol{\sigma}_{\mathrm{eff}} - \alpha_B \chi p_{\mathrm{LR}} \mathbf{I}) + [(1 - \phi) \varrho_{\mathrm{SR}} + S_{\mathrm{L}} \phi \rho_{\mathrm{LR}}] \boldsymbol{b} \tag{38}$$

with Bishops saturation cutoff $\chi(S_{\mathrm{L}}) = \begin{cases} 0 \text{ if } S_{\mathrm{L}} < 1 \\ 1 \text{ else} \end{cases}$

The porosity evolution is given by:

$$\phi_{\mathrm{S}}' = (\alpha_B - \phi)\left[\nabla \cdot \boldsymbol{u}_{\mathrm{S}}' - \beta_{T,\mathrm{SR}} T_{\mathrm{S}}' + \beta_{p,\mathrm{SR}} (p_{\mathrm{FR}})_S'\right] \tag{39}$$

with $p_{\mathrm{FR}} = (1 - \chi) p_{\mathrm{GR}} + \chi p_{\mathrm{LR}}$ and $p_{\mathrm{GR}} = p_{\mathrm{atm}}$

Water density is calculated as:

$$\rho_{\mathrm{LR}} = \rho_{\mathrm{LR}}^{0} \cdot \left(e^{-\beta_{T,\mathrm{LR}} \cdot (T - T_0)} \cdot e^{\beta_{p,\mathrm{LR}} \cdot \left(\max(0, p_{\mathrm{LR}}) - p_{\mathrm{LR}}^{0} \right)} \right) \tag{40}$$

BGR/UFZ

The water mass balance equation that BGR/UFZ used in Step 0b was modified to include the medium deformation explicitly for step 0C:

$$0 = \frac{\mathrm{d}\left(\phi \rho_{\mathrm{F}}^{\zeta}\right)}{\mathrm{d}t} + \phi \rho_{\mathrm{F}}^{\zeta} \mathrm{div}\left(\frac{\mathrm{d}\boldsymbol{u}}{\mathrm{d}t}\right) + \mathrm{div}\left(\boldsymbol{A}^{\zeta} + \boldsymbol{J}^{\zeta}\right) \tag{41}$$

The porosity evolution in the OGS-6 TH^{2}M implementation used in step 0C is given by:

$$\frac{\mathrm{d}}{\mathrm{d}t}\phi = (B - \phi_0)\left(\mathrm{div}\left(\frac{\mathrm{d}\boldsymbol{u}}{\mathrm{d}t}\right) - \alpha_T \frac{\mathrm{d}T}{\mathrm{d}t} + \beta_{p,\mathrm{S}} \frac{\mathrm{d}\left((1 - S)p_{\mathrm{G}} + S p_{\mathrm{L}}\right)}{\mathrm{d}t} \right) \tag{42}$$

Here, $\boldsymbol{u}$ represent the solid displacement vector and $\beta_{p,\mathrm{S}}$ (Pa^{-1}) is the solid compressibility. This porosity evolution includes a mechanical coupling via the solid deformation term.

BGR/UFZ initially used a staggered THM implementation, which led to convergence issues for the given problem (especially in the HM-coupling). With the change to the monolithic TH^{2}M implementation in OGS-6, these issues were resolved. As shown in Pitz *et al*. (2023), in case of full saturation, the water mass balance and momentum balance equations of the TH^{2}M model reduce to the same equations as they were used in the non-isothermal Richards equation (with mechanics) before.

Appendix A gives details of the THM porosity evolution, compared with the TH formulation.

CAS

In this case, the porosity equation of CAS was as follows:

$$\phi = (\phi_0 + \beta \varepsilon_v - \alpha_T (\beta - \phi_0)(T - T_0)) / (1 + \varepsilon_v) \tag{43}$$

where α is Biot coefficient, α_T is thermal expansion of solid and ε_v is volumetric strain.

For the part of effective stress, the CAS's equation is different from the above definition. The effective stress is dependent on pore pressure, thermal stress and swelling pressure. The equation is shown as follows:

$$\sigma' = \sigma + \alpha\chi pI + P_{sw} + \alpha_T C \Delta T \tag{44}$$

where χ is the Bishop coefficient, P_{sw} is the tensor of swelling pressure and C is the tensor of elasticity.

ENSI

Please see the description of BGE/TUBAF.

GRS

For unsaturated parts of the model, there was a small deviation between the definition of effective stresses in the task specification and in CODE_BRIGHT. The above defined Biot effective stress only considers the influence of pore pressure on the effective stresses for saturated material (p_w is positive). For unsaturated parts of the model, the effective stress is equal to the total stress. Instead, CODE_BRIGHT also considers the influence of pore pressure on effective stresses for unsaturated parts by adding gas pressure and total stresses.

$$\boldsymbol{\sigma}' = \sigma + p_f \qquad with\ p_f = \max(p_g, p_w) \tag{45}$$

$$\text{for } p_w > 0 \text{ MPa} \rightarrow \boldsymbol{\sigma}' = \sigma + p_w$$

$$\text{for } p_w < 0 \text{ MPa} \rightarrow \boldsymbol{\sigma}' = \sigma + p_g$$

Since gas advection was neglected in this case, the gas pressure was set constant to 0.1 MPa resulting in a very small deviation of GRS' modelling results.

KAERI/KIGAM

The mass balance equation in the code of OpenGeoSys-5 is as follows:

$$\underbrace{n\left[\frac{\rho_w - \rho_v}{\rho_w}\frac{\partial S_w}{\partial p} + (1 - S_w)\frac{\rho_v}{\rho_w^2 RT}\right]\frac{\partial p}{\partial t} + S_w\left(n_0\beta_w + n_0 \cdot c_p\right)\frac{\partial p}{\partial t}}_{\text{Storage}} + \underbrace{\nabla \cdot (\boldsymbol{q} + \boldsymbol{q}_v)}_{\text{Flow}} \tag{46}$$

$$+\underbrace{\mathrm{n}\frac{1-\mathrm{S_w}}{\rho_\mathrm{w}}\left(\mathrm{h_{rel}}\frac{\partial\rho_\mathrm{vS}}{\partial\mathrm{T}}+\frac{\rho_\mathrm{v}\mathrm{p}}{\mathrm{RT}^2}\right)\frac{\partial\mathrm{T}}{\partial\mathrm{t}}}_{\text{Vapour diffusion}}-\underbrace{(\mathrm{n_0S_w}\beta_w^{th}+(\alpha-\mathrm{n})\ 3\beta_s^{th})\frac{\partial\mathrm{T}}{\partial\mathrm{t}}}_{\text{Thermal expansion}}=0$$

Porosity change depends on the volumetric strain change (Elyasi et al., 2016) to consider the mechanical effect during the coupled simulation:

$$n = n_o + \alpha\Delta\varepsilon_v + \frac{1}{\varphi}\Delta\mathrm{p} \tag{47}$$

where n_o is the initial porosity, ε_v the volumetric strain, α the Biot coefficient, and φ is the material constant, which is infinite for the porous media in this study. Pore compressibility of each material was also applied based on the given specification to consider the mechanically induced storage term change in the equation (46).

NWMO

The hydraulic balance equation that was used in NWMO's coupled THM model is as follows (Guo, 2023):

$$\frac{\partial(\phi S_e\rho_w+\phi(1-S_e)\rho_v)}{\partial t}+(\phi S_e\rho_w+\phi(1-S_e)\rho_v)\frac{1}{1+\varepsilon_v}\frac{\partial\varepsilon_v}{\partial t}+\nabla q_l+\nabla q_v=0 \tag{48}$$

$$q_v=-\rho_l(D_{pv}\nabla p+D_{Tv}\nabla T)$$

$$D_{pv}=D_v\,\rho_v/(\rho_w^2R_vT)$$

$$D_{Tv}=\frac{f_{Tv}D_v[R_H\left(\frac{d\rho_{vs}}{dT}\right)-\frac{s_c\rho_v}{\rho_wR_vT^2}]}{\rho_l}$$

Definition of the porosity variation depends on the hydraulic balance equation used in the coupled THM modelling. The following equation was used for the porosity in this modelling activity in NWMO's coupled THM models (Guo, 2023):

$$\phi=(\phi_0+\alpha_B\varepsilon_v+(\alpha_B-\phi_0)(p-p_0)(1-\alpha_B)C_m-\alpha_s(\alpha_B-\phi_0)(T-T_0))/(1+\varepsilon_v) \tag{49}$$

where α_s is the volumetric thermal expansion of the rock (1/K), ϕ_0 is the initial porosity (unitless), C_m is the inverse of rock bulk modulus (Pa^{-1}), α_B is the Biot coefficient (unitless), ε_v is the volumetric strain (unitless), p is the pore water pressure (Pa), p_0 is

the reference pressure (Pa), T is the temperature (K), and T_0 is the reference temperature (K).

4.5.2 Results 0c2

The first simplified case, with no bentonite and no flow in the Opalinus Clay, gave temperature results that were very consistent across the teams that supplied results (Figure 16). The temperature results are very similar to those in Step 0b2 because the mechanical part of the equations does not affect temperature.

Most teams produced very similar estimates of pore pressure in the Opalinus Clay, with one team (KAERI) showing different trends in pore pressure (Figure 17). The pressure results are influenced by the change in volume, porosity and water density. KAERI had not implemented the effect of the change in pore volume due to stress changes in their water balance equation, which explains why their results differ from the other teams.

Consistent with the pressure results, the stress and displacement results show similar results (in both the x-direction and the z-direction, but only x results are shown in Figure 18 and Figure 19).

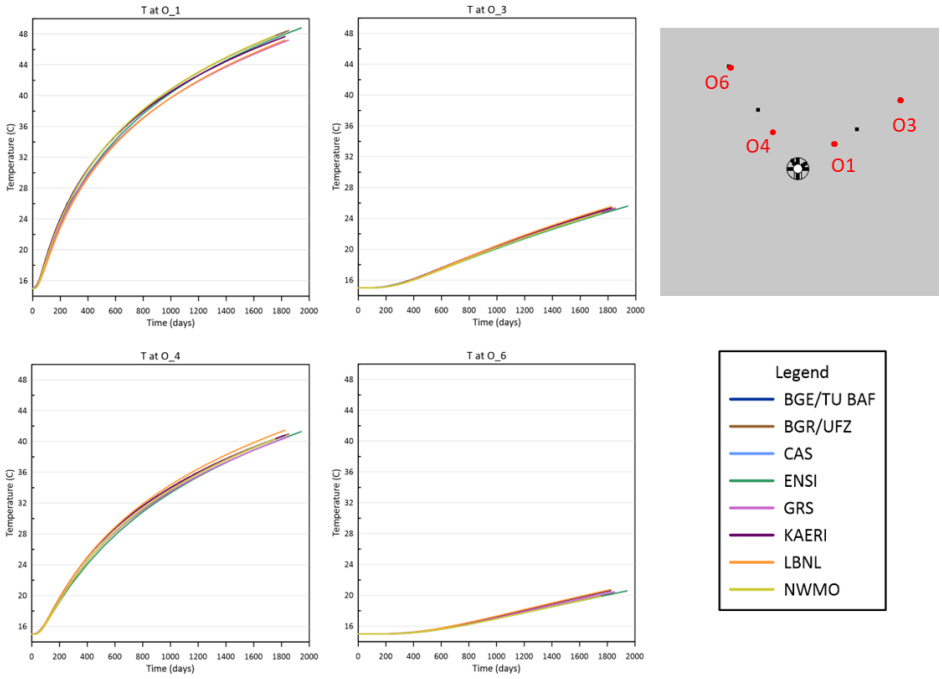

Figure 16: Selected temperature results for locations in the Opalinus Clay from Step 0c2.

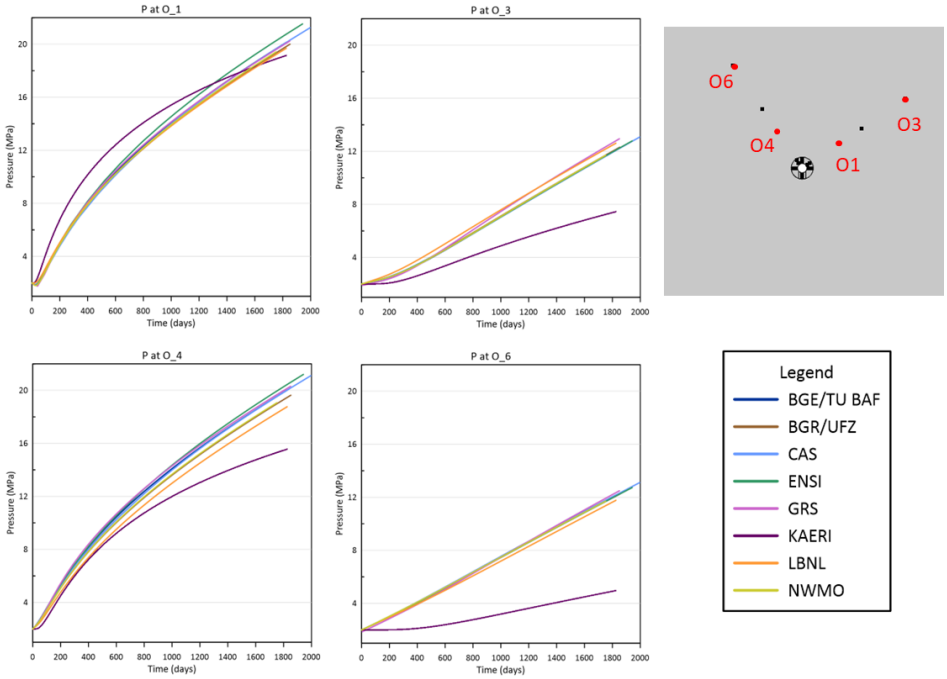

Figure 17: Selected pressure results for locations in the Opalinus Clay from Step 0c2.

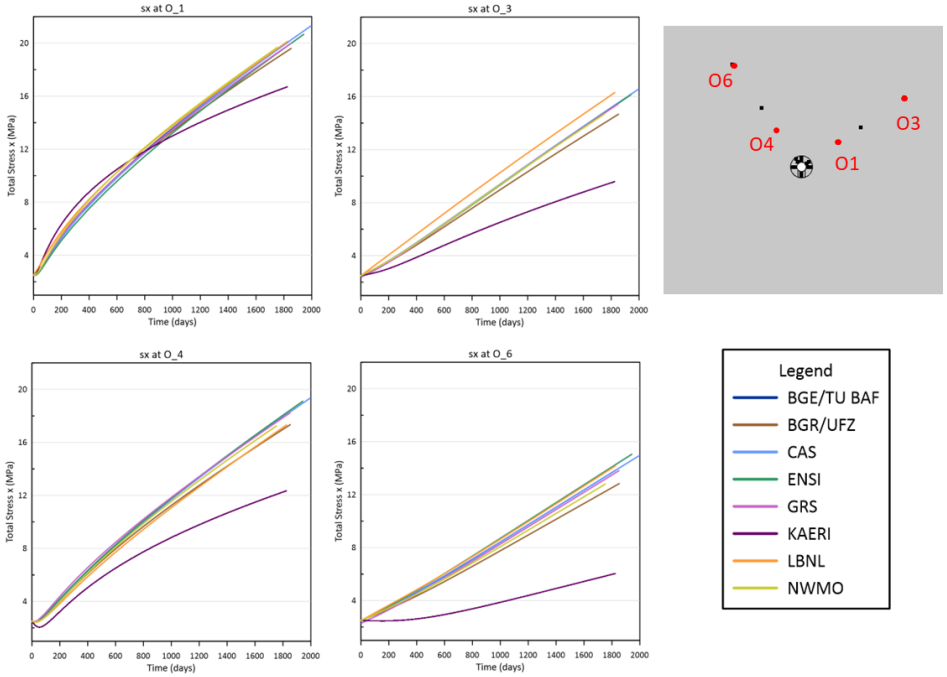

Figure 18: Selected total stress in the x-direction results for locations in the Opalinus Clay from Step 0c2.

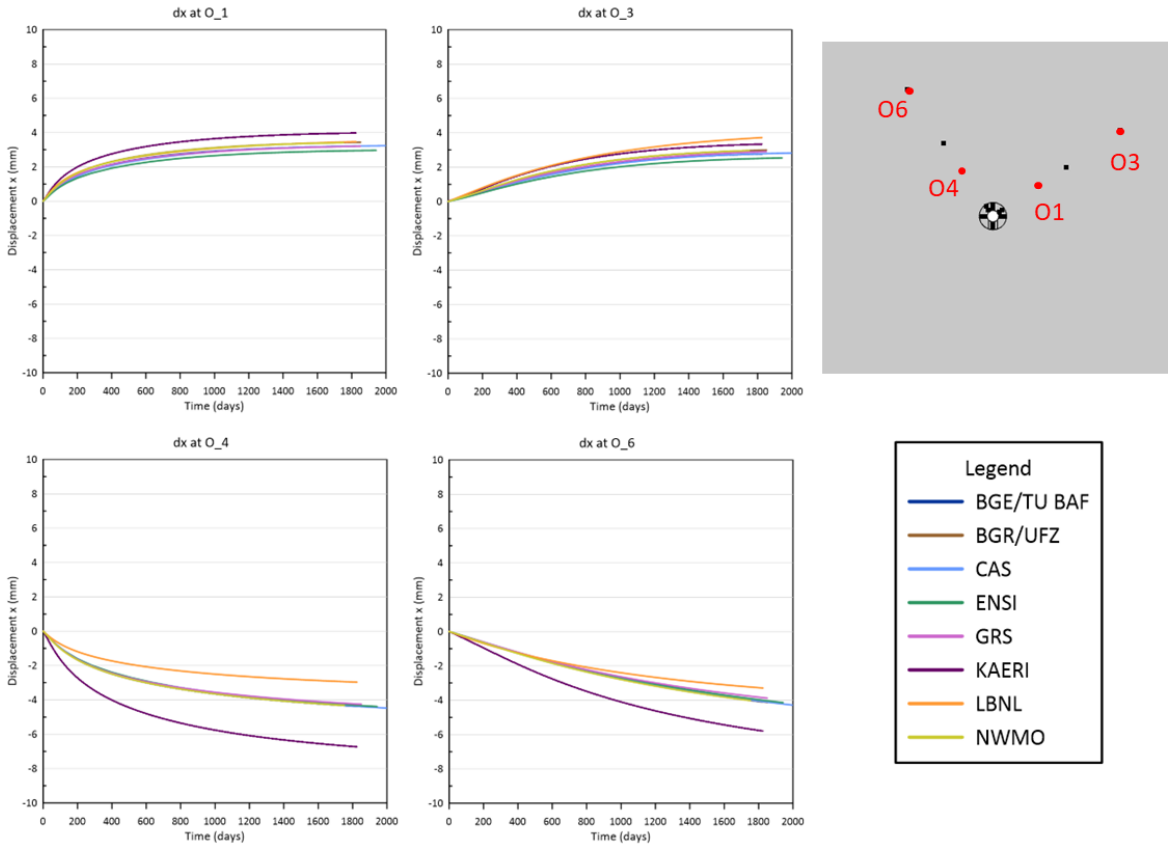

Figure 19: Selected displacement in the x-direction results for locations in the Opalinus Clay from Step 0c2.

4.5.3 Results 0c3

This second simplified case, with no bentonite but with a non-zero permeability in the Opalinus Clay gave temperature results that were very similar to Step 0c2 (and are therefore not shown), which was unsurprising as the Opalinus Clay is saturated so there was no change in thermal properties.

Pressure, stress and displacement results differ from Step 0c2 in magnitude due to the addition of drainage in Step 0c3, but the relationships between the results of the different teams are the same, and therefore only the pressure results are presented (Figure 20). Most teams produced very similar results with the same team showing different results as in Step 0c2 for the same reason.

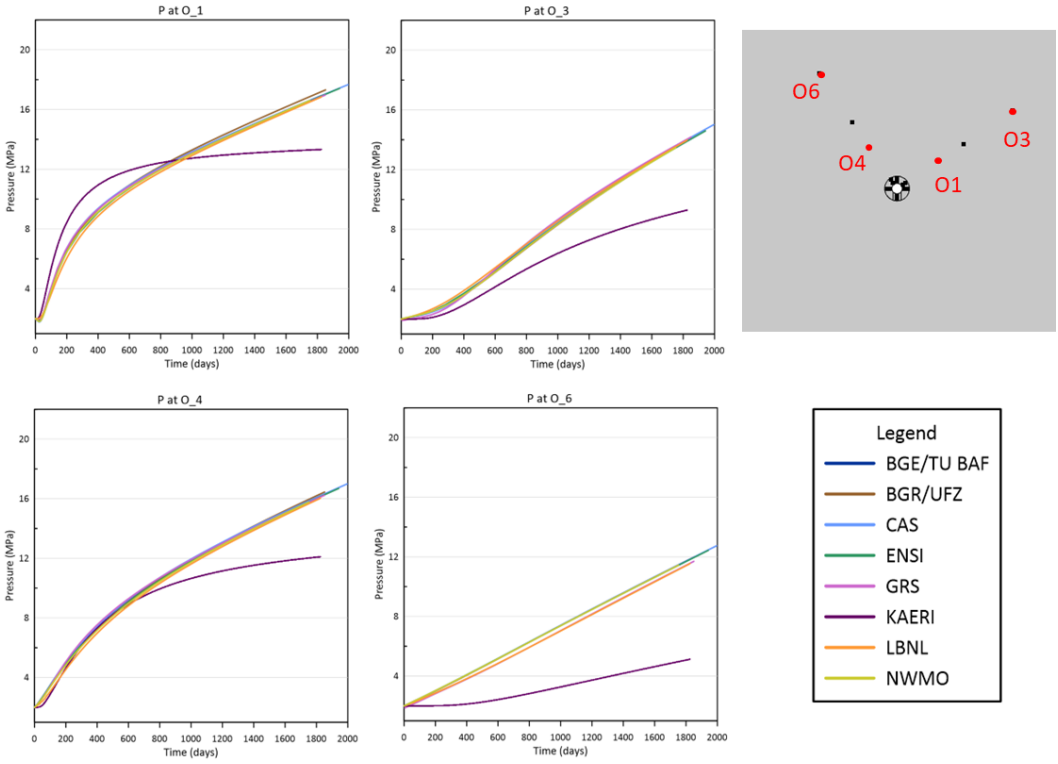

Figure 20: Selected pressure results for locations in the Opalinus Clay from Step 0c3.

4.5.4 Results 0c

Results from the THM models including bentonite within the FE tunnel show more spread across the teams than the simpler cases. All teams showed generally good agreement for temperatures in the Opalinus Clay (Figure 21).

Pressure results in Step 0c were generally less consistent than in Step 0b (Figure 22). Nevertheless, there is agreement to within 1 MPa for most teams, with KAERI and LBNL overestimating peak pressure at sensor O_1 and KAERI and CAS showing lower pressures at the end of the model run than other teams. The reason for KAERI's results being different is due to the lack of a deformation term in the water mass balance as discussed previously. The reasons for the small differences in LBNL and CAS's results are not known.

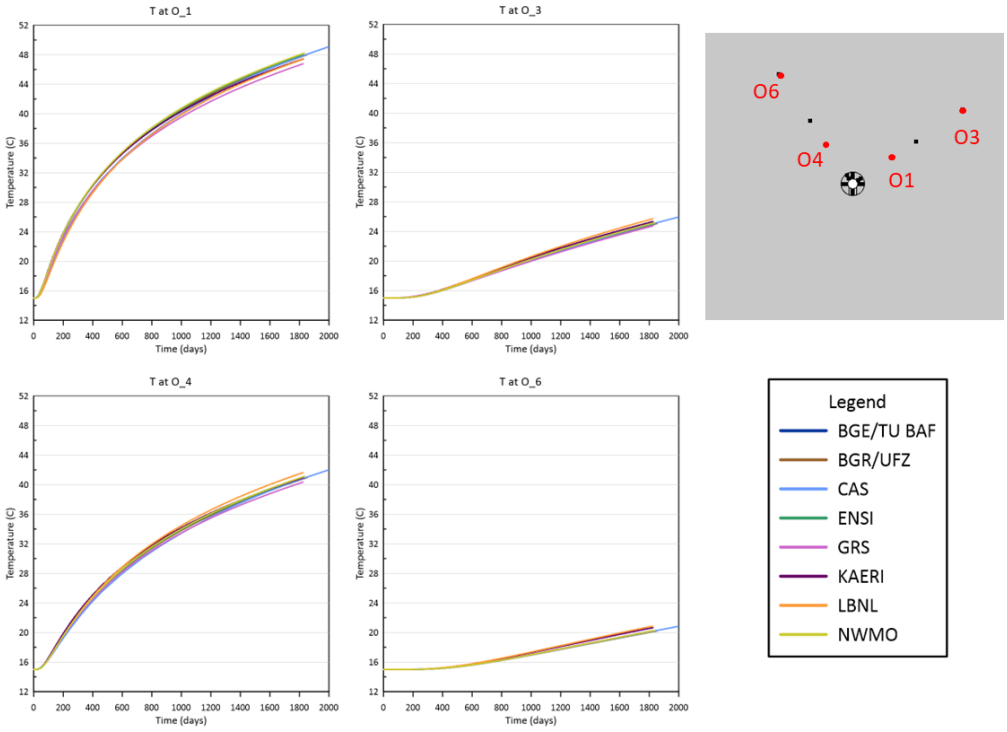

Figure 21: Selected temperature results for locations in the Opalinus Clay from Step 0c.

Results for stress and displacement are not shown here because they show similar patterns between the teams as the pressure results for Step 0c and the stress and displacement results for Steps 0c2 and 0c3.

In the bentonite, temperature and relative humidity are very similar to Step 0b with generally good agreement between all teams.

There are very limited changes in stress in the bentonite in all models, illustrating that the stress and strain changes generated within the Opalinus Clay are largely not transmitted to the FE tunnel. Teams showed small and consistent patterns of displacement in the bentonite.

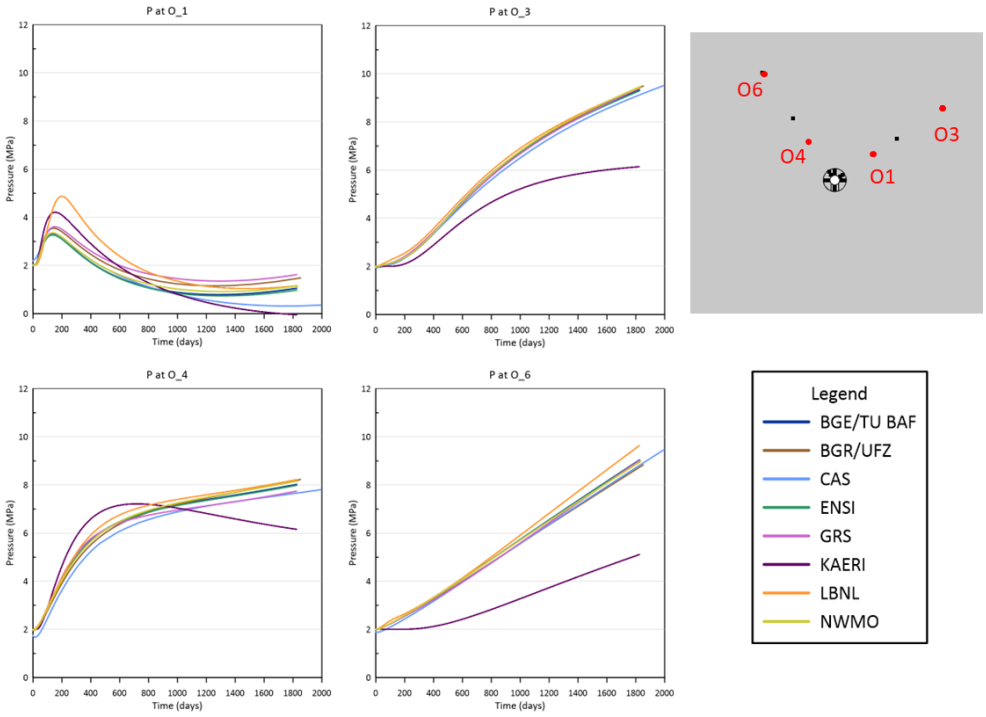

Figure 22: Selected pressure results for locations in the Opalinus Clay from Step 0c.

4.5.5 Discussion

The addition of mechanical processes to this model was a significant increase in complexity. Initially, teams were able to produce very similar predictions of temperature and consistent predictions of trends in porewater pressure development in the Opalinus Clay, but the predicted magnitudes of porewater pressure varied significantly (by up to 7 MPa) between teams. The reasons for those differences were investigated and made consistent as part of this benchmarking task. The primary differences included: representation of the thermal expansion coefficient of water (linear rather than temperature-dependent), different formulations of porosity evolution, differences in modelled domain sizes and boundary conditions, and differences in grid discretisation (and the location of reported output points). This exercise usefully highlighted assumptions which the results are sensitive to (information on further sensitivity

analyses is given below) and demonstrated the benefit of model comparisons between multiple teams to give an indication of uncertainties.

By the end of the task, all teams but KAERI were able to produce similar results. KAERI are aware of the reason for their results being different but did not have the time to implement the changes needed.

In this task, the primary focus was pore pressure generation in the Opalinus Clay. The teams produced a set of models that give consistent pore pressure results in the Opalinus Clay.

A number of teams (BGR/UFZ, BGE/TUBAF, GRS and NWMO) conducted sensitivity analyses to the domain size in these 2D calculations and found that, whilst a 50 m x 50 m domain was sufficient for the T and TH models, it was not sufficiently large for the THM models in order to obtain behaviour independent of the boundary conditions. This can be seen in comparison of the results from Step 0b and Step 0c, where Step 0c gives significantly higher pore pressures because the zero-displacement boundary condition on the outer boundaries confines the expansion of the pores within the Opalinus Clay. This effect is shown by BGR/UFZ in Figure 23 where different domain sizes were modelled alongside different boundary conditions, resulting in different pore water pressure response. Further details on this can be found in Appendix A. This was an important consideration when moving to representation of the full FE experiment.

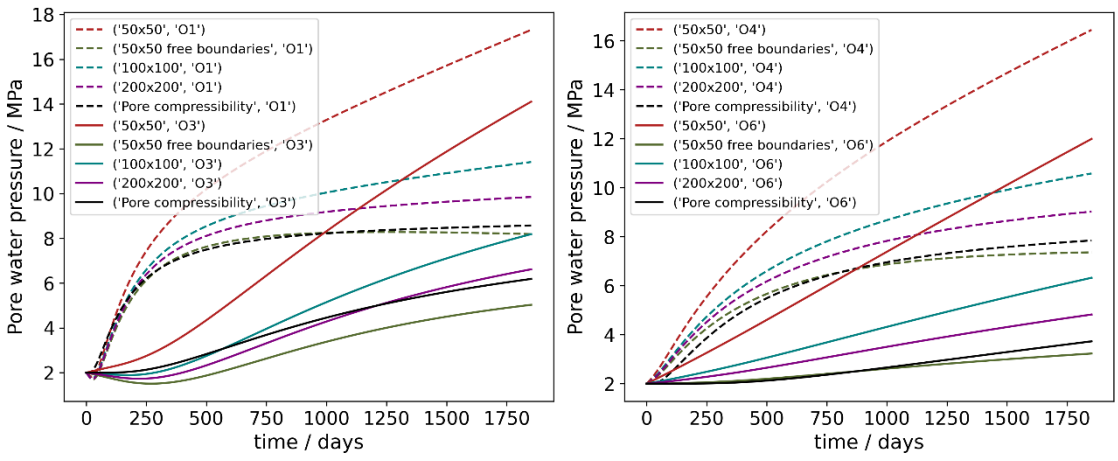

Figure 23: Pore water pressure temporal evolutions in the bedding parallel (left) and bedding perpendicular (right) direction in the near field (point O1, solid lines) and far field (point O3, dotted lines).

5 Step 1 – Heating phase of the FE experiment

5.1 Aim

The aim of Step 1 was to move from 2D simplified benchmark models to 3D models of the FE experiment and to begin to compare the model output against data from the FE experiment. A subset of the available data was used for initial comparison with models, and a larger data set was made available to teams who wished to investigate how to best use the large amount of data from the FE experiment. Step 1 still had a tightly defined specification, with teams asked to use a simplified geometry (shotcrete and EDZ are not considered) and prescribed parameterisation to build confidence in the comparison between models, before being invited to calibrate parameters against the experimental data. Furthermore, only the heating phase was represented in the models (excavation and ventilation were not considered). A more open invitation to update the modelling approach was given in Step 2.

For Step 1, the teams were asked to start modelling at the onset of heating and to assume specified initial conditions in the Opalinus Clay and tunnel backfill. It was expected that the initial temperature of the Opalinus Clay should be relatively well captured by a constant initial condition, and therefore modellers were asked to look at the absolute temperature. However, the pore pressure field at the start of heating is affected by the excavation and ventilation of the FE tunnel, such that models initialised at the start of heating with a constant pressure in the Opalinus Clay were unlikely to capture the correct absolute pressure. Still, models should be capable of capturing the changes in pore pressure, assuming linear elasticity and linear water compressibility, so only changes in pressure from the initial conditions were considered in this step.

The tasks for this step were for teams to:

1. Build 3D models of the FE experiment and supply temperature, pressure changes, relative humidity, stress and displacement data at specified output locations. These models should initially be 3D versions of the 2D models developed in Step 0c.
2. Consider how best to use the large amount of data available from the FE experiment to improve understanding and representation of the FE experiment.
3. Calibrate the material properties to improve the model fit to the data and supply updated temperature, pressure changes, relative humidity, stress and displacement data at specified output locations.

5.2 Model specification

5.2.1 Geometry and measurement locations

The 3D model geometry used in Step 1 was an extension of the 2D geometry used in Step 0 and considered all three heaters of the FE experiment. The cross-sectional geometry through the tunnel was the same as in Step 0 (Figure 1) and the geometry along the tunnel is shown in Figure 24. Dimensions are given in Table 5. Teams were requested to choose a domain size that was large enough, so the boundary conditions did not impact their results over a 5-year model run.

The locations for data output for comparison with other teams are given in Table 6. As we were modelling a simplified geometry, the sensor locations were not always consistent with the geometry, particularly close to the heater surface, with some sensors plotting inside the heater. To overcome this, some alternative sensor locations were proposed for the sensors in the tunnel as shown in Table 6. The FE-coordinate system was used in this work, as shown in Figure 24 (although the y-origin of the coordinate system is outside the tunnel).

Table 5: Details of the geometry for the 3D model.

Description	Value	Reference
Diameter of FE tunnel (Dt)	2.48 m	Nagra, 2019
Heater diameter (Dh)	1.05 m	Nagra, 2019
Pedestal width at base (Wp)	0.8 m	Nagra, 2019
Length of sealing section (Ls)	12.5 m	Firat Lüthi, 2018
Length of heaters (Lh)	4.6 m	Nagra, 2019
Length of gap 1 (Lg1)	3 m	Nagra, 2019
Length of gap 2 (Lg2)	3 m	Nagra, 2019
Length of gap 3 (Lg3)	3 m	Nagra, 2019
Length of plug (Lp)	5 m	Nagra, 2019
Length of access section (La)	9 m	Firat Lüthi, 2018

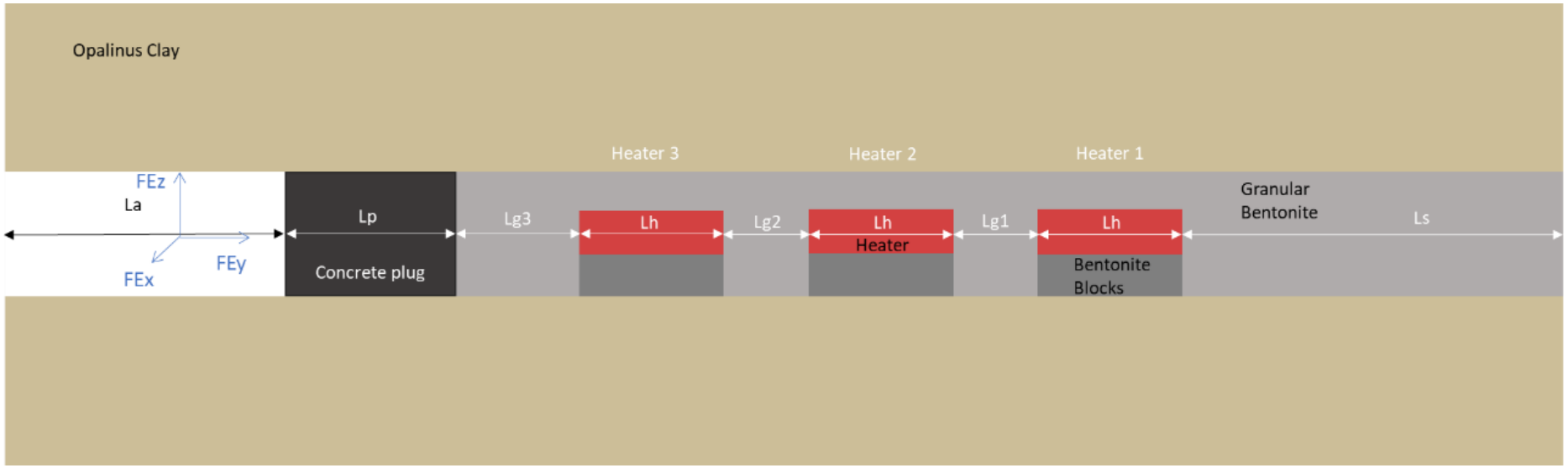

Figure 24: Model geometry for Step 1.

Table 6: Measurement locations and parameters for reporting (note locations that are bold and in brackets are the suggested alternative locations to be consistent with the simplified geometry).

	Sensor	Measure-ment	Gallery meters / m	FE-x / m	FE-y / m	FE-z / m
Temperature on the heater surface						
1	T_H1_230_O_1	T	35.45	-0.057 **(-0.062)**	40.147	0.479
2	T_H2_230_O_1	T	27.9	-0.072 **(-0.075)**	32.596	0.5 **(0.52)**
3	T_H2_230_O_3	T	27.9	0.508 **(0.525)**	32.596	-0.022 **(-0.023)**
4	T_H2_230_O_4	T	27.94	-0.017 **(-0.016)**	32.641	-0.547 **(-0.525)**
5	T_H3_230_O_2	T	20.28	-0.001	24.98	0.499 **(0.525)**
Temperature 20 cm from heater surface						
6a	T_BH2-230_6	T	27.9	0.395 **(0.359)**	32.596	0.692 **(0.630)**
7a	T_BH2-230_7	T	27.88	0.709 **(0.725)**	32.576	-0.022
8a	T_BH2-230_8	T	27.91	-0.017 **(-0.016)**	32.606	-0.755 **(-0.725)**
9a	T_BH2-230_10	T	27.89	-0.385	32.586	0.614
Relative humidity 20 cm from heater surface (at same locations as temperature measurements)						
6b	RH-H2-230-6	RH	27.9	0.345	32.596	0.605
7b	RH-H2-230-7	RH	27.88	0.808	32.576	-0.022
8b	RH-H2-230-8	RH	27.91	-0.017	32.606	-0.855
9b	RH-H2-230-10	RH	27.89	-0.430	32.586	0.692
Temperature in the Opalinus Clay						
10a	BFEA002_TEM_03	T	28.27	4.593	32.966	2.517
11a	BFEA003_TEM_03	T	27.89	7.142	32.588	4.287
12a	BFEA004_TEM_03	T	28.06	11.660	32.765	8.508
13a	BFEA005_TEM_03	T	27.9	-3.602	32.598	3.714
14a	BFEA006_TEM_03	T	27.91	-4.998	32.612	6.282

	Sensor	Measure-ment	Gallery meters / m	FE-x / m	FE-y / m	FE-z / m
15a	BFEA007_TEM_03	T	27.94	-8.956	32.638	11.702
Pressure in the Opalinus Clay (at same locations as temperature measurements)						
10b	BFEA002_PRE _03	P	28.27	4.593	32.966	2.517
11b	BFEA003_PRE_03	P	27.89	7.142	32.588	4.287
12b	BFEA004_PRE_03	P	28.06	11.660	32.765	8.508
13b	BFEA005_PRE_03	P	27.9	-3.602	32.598	3.714
14b	BFEA006_PRE_03	P	27.91	-4.998	32.612	6.282
15b	BFEA007_PRE_03	P	27.94	-8.956	32.638	11.702
Displacement / strain in the Opalinus Clay						
16a	BFEB012_DFO_01_res_H	Disp	26.6	-4.797	31.301	8.329
17a	BFEB012_DFO_04_res_H	Disp	26.6	-1.861	31.301	3.177
16b	BFEB012_DFO_01-02_res_strain	Strain	26.6	-4.797	31.301	8.329
17b	BFEB012_DFO_04-05_res_strain	Strain	26.6	-1.861	31.301	3.177
18a	BFEB011_DFO_01_res_H	Disp	26.6	7.311	31.301	6.139
18b	BFEB011_DFO_04_res_H	Disp	26.6	2.766	31.301	2.33
19a	BFEB011_DFO_01-02_res_strain	Strain	26.6	7.311	31.301	6.139
19b	BFEB011_DFO_04-05_res_strain	Strain	26.6	2.766	31.301	2.33

5.2.2 Material properties

Material properties used in Step 1a were the same as those in Step 0 (Table 4). Teams could choose whether to include the concrete plug or not. Teams calibrated these material properties in Step 1c and the updated parameter values are presented in Section 5.5.1.

5.2.3 Initial and boundary conditions

Initial and boundary conditions were specified as shown in Table 7. Teams were asked to use a model domain that was large enough so that the outer boundaries did not affect the results. Therefore, the type of boundary condition on the outer boundaries was not specified. The heating schedule is given in Table 8.

Table 7: Initial and boundary conditions

	Initial	Heater boundary
Thermal	15˚C	See Table 8
Hydraulic	OPA: 2 MPa pore pressure, saturation of 1 Granular bentonite: water content 5 wt% Bentonite blocks: water content 18 wt% Concrete: saturation of 0.1	No flow
Mechanical	σ1 = σz = 6.5 MPa σ2 = σy = 4.5 MPa σ3 = σx = 2.5 MPa	Zero displacement

Table 8: Heating schedule (Firat Lüthi, 2018)

	Date	Power (W)
Heater 1	15.12.2014 13.01.2015 16.02.2015	500 1000 1350
Heater 2	17.02.2015	1350
Heater 3	18.02.2015	1350

5.2.4 Step structure

Step 1 comprised three parts:

1. **Step 1a:** a 3D THM simulation of the heating phase of the FE experiment, following the tightly defined model specification.
2. **Step 1b:** comparison of the model results against the data available and consideration of how best to use the large dataset available.
3. **Step 1c:** calibration of the material parameters in the 3D THM model with no addition of features or processes to the model, to determine whether the models can match the observations with the assumed simplifications.

5.3 Step 1a

5.3.1 Modelling strategy

The teams used the same equations in Step 1a as were implemented in Step 0c, with the exceptions noted below. The difference between Step 0c and Step 1a was the full 3D geometry which required teams to build a 3D mesh and solve the equations in 3D rather than a 2D approximation. The domain sizes used by the teams are shown in Table 9.

Different teams took different approaches to representing the heaters in their model (Table 9).

Table 9: Domain sizes chosen by teams for Step 1a.

Team	Heater representation	Domain size (m)	Number of nodes/ elements
BGR/UFZ	Surface boundary	150 x 100 x 150	120000/720000
BGE/TUBAF	Surface boundary (mantle surface)	500 x 500 x 500	213195 / 1279828
CAS	Thin walled cylinder	100 x 100 x 55	226703 / 214240
DOE/LBNL	Solid volume	150 x 150 x 150	64158 / 67627
ENSI	Surface boundary	50x50x50	110405 / 644554
GRS	Solid volume	100 x 100 x 49.3	44368/259244
KAERI/KIGAM	Surface boundary	100 x 60 x 100	38403 / 71710
NWMO	Solid volume	100 x 90 x 100	140888/269371
DOE/SNL	Solid volume	50 x 50 x 50	1,038,463 elements

SNL

The SNL PFLOTRAN model was a TH model, and so results were not provided for THM.

5.3.2 Results

In Step 1a, the models had not been calibrated against the experimental data, and modellers were guided to using the same geometry, initial and boundary conditions and material properties as each other. There were some known differences between the models, such as the representation of the heaters or the domain size of the models. Analysis of the results therefore focusses on the similarity of results between modelling teams before assessing how well the experimental data are represented by the models.

The modelled temperature increase in the Opalinus Clay showed a very consistent trend across the teams (Figure 25), but there was significant divergence in the magnitude of temperature increase, particularly at sensors BFEA002_TEM_03 and BFEA005_TEM_03, which are closer to the tunnel. There was no correlation between heater boundary conditions chosen and the temperature results from the teams. The reasons for the discrepancies could include the chosen grid, the boundary conditions or the size of the model domain. Compared to the data from the FE experiment, the specified initial temperature was lower than that observed in the experiment. Most models underpredicted the increase in temperature in the bedding parallel direction based on the prescribed parameters but seemed to cover the increase in temperature in the perpendicular direction. The real anisotropy of the thermal properties in the Opalinus Clay may have differed from that given in the specification.

Modelled pressure changes in the Opalinus Clay showed similar trends across the teams but with significantly different magnitudes of change for all four sensors (Figure 26). There was no obvious correlation between differences in modelled temperatures and pressures. The reasons for the discrepancies could again include the chosen grid, the boundary conditions or the size of the model domain. Compared to the data from the FE experiment, the models show more rapid pressure increases and decreases and significantly more drainage, particularly at BFEA002_TEM_03. This could have been caused by parameterisation of the hydro-mechanical properties of the Opalinus Clay, which are investigated in Step 1c, as well as the simplified representation of the FE tunnel, which is investigated in Step 2.

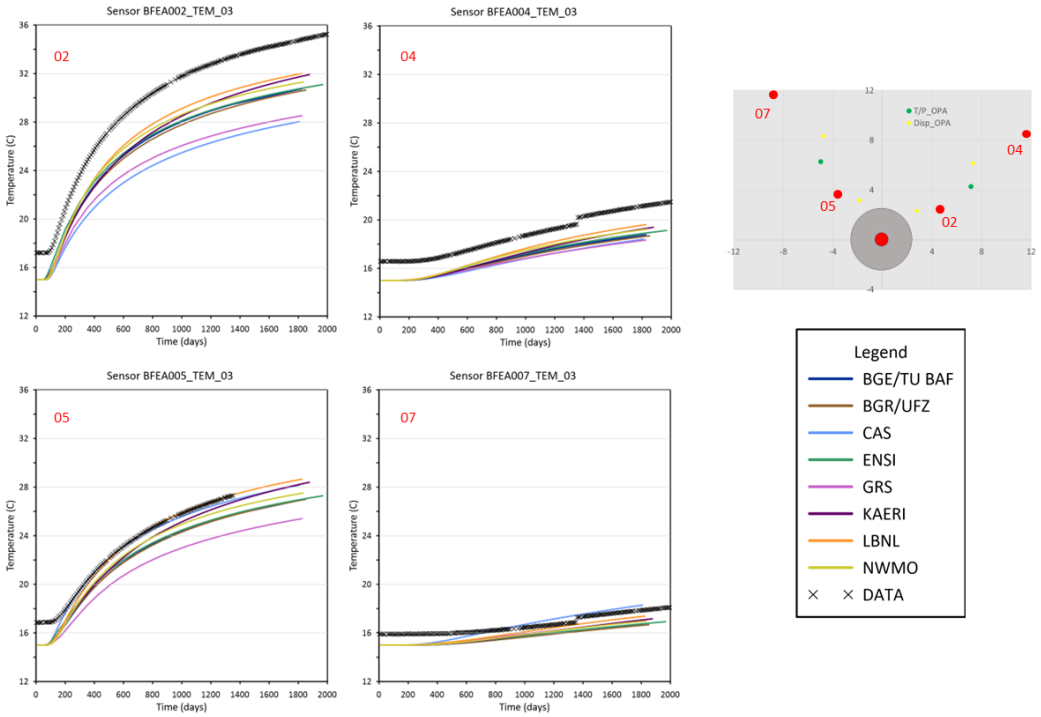

Figure 25: Selected temperature results for locations in the Opalinus Clay from Step 1a.

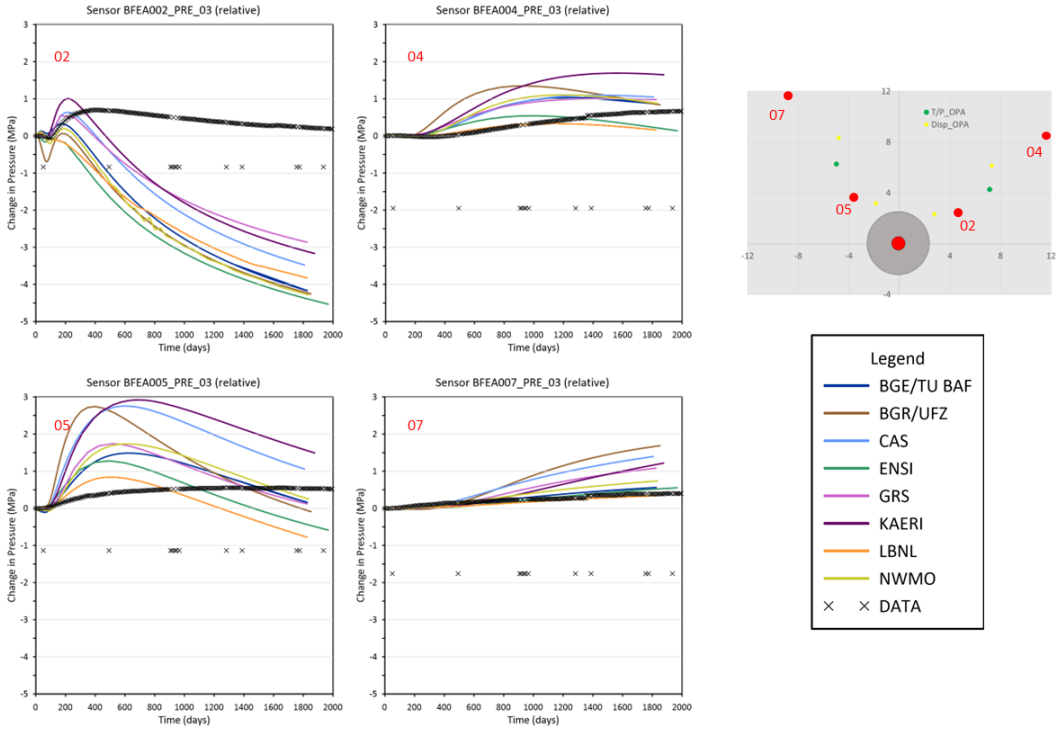

Figure 26: Selected pressure results for locations in the Opalinus Clay from Step 1a.

Modelled temperature increase in the bentonite (granular and blocks) shows reasonably consistent trends across the teams, but with a large range in magnitude of temperature

increase (Figure 27). The range in temperature increase at sensor T_H2_230_O_3 was 45°C, whilst most teams predicted a peak temperature between 111°C and 124°C. There was no obvious correlation between temperatures and the representation of the heater boundary. The reasons for the discrepancies could be the saturation dependent heat conductivity of the bentonite as well as the hydraulic behaviour relevant for the resaturation of the bentonite. The results for the relative humidity supported this. Compared to the data from the FE experiment, the models generally underpredicted temperatures, consistent with the findings in the Opalinus Clay. This could indicate that thermal conductivity was overestimated.

Modelled relative humidity in the bentonite (granular and blocks) showed quite different trends between the teams (Figure 28).

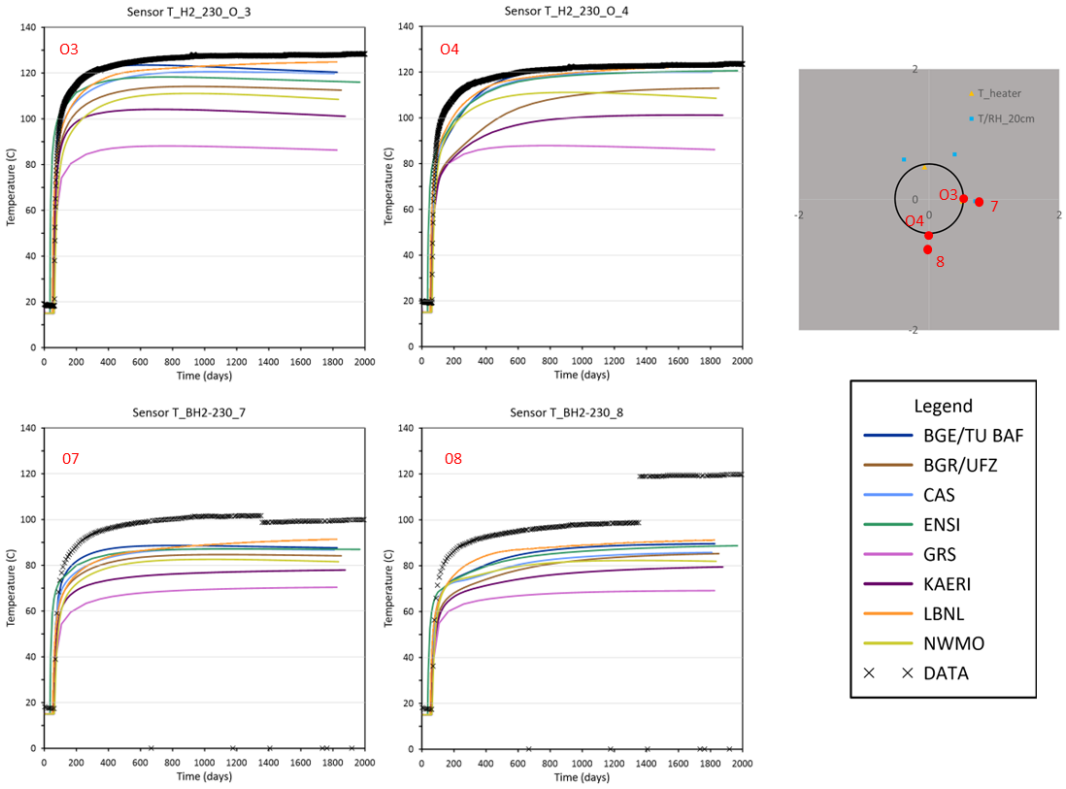

Figure 27: Selected temperature results in the bentonite from Step 1a.

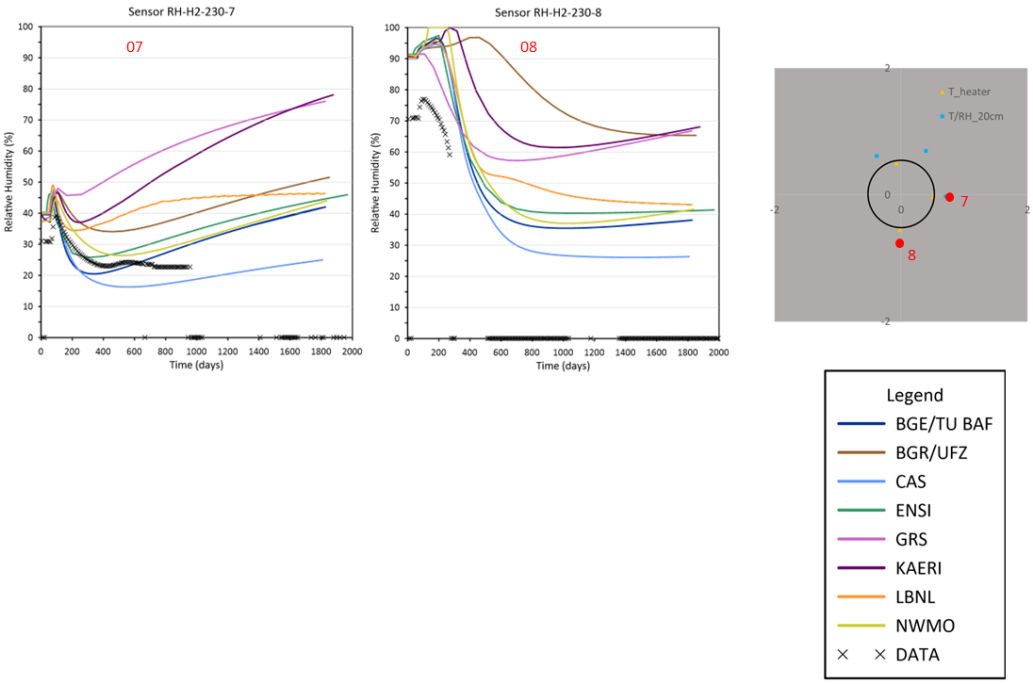

Figure 28: Selected relative humidity results in the bentonite for Step 1a (note that there are no RH sensors at locations O3 and O4, which are on the heater surface).

5.3.3 Discussion

Step 1a was an extension of the benchmarking exercise, this time in 3D, but still with the tightly defined model specification. It is interesting to note that when moving from 2D to 3D models the results became more different across the teams. Assuming all teams continued to follow the specification (or continued to differ from the specification in the same way between Step 0c and Step 1a), there are some reasons that could explain the differences in results. One possibility is that the domain sizes affect the results, and whilst there was not a clear trend between domain sizes, the teams with higher pressures / more rapid pressure response (BGR/UFZ, CAS, KAERI, GRS) did have smaller domains than those with lower pressures (BGE/TUBAF, LBNL). So domain size may be a contributing factor and due to the 3D models being computationally expensive, not all teams have been able to show that their assumptions around domain size did not affect their results. In general, this pointed to the relevance of mechanical boundary conditions and the properties of adjacent geological layers (see also Appendix D).

Another potential difference between models was the grid discretisation, both around the heaters and the tunnel and also around the measurement locations. Again, the more computationally expensive 3D runs may have caused teams to have to choose meshes

that were coarser than ideal or that did not have nodes at the measurement locations, both of which could have affected the reported results.

Several teams (NWMO, BGE/TUBAF, BGR/UFZ) have also reported that the initial pressure assumed affects the change in pore water pressure during heating. NWMO demonstrated this effect (Figure 29) (Guo and Briggs, 2024) and while it does not appear to be a big enough effect to explain all the differences between the teams' results, it could be a contributing factor, particularly in the timing of pressure build-up and release.

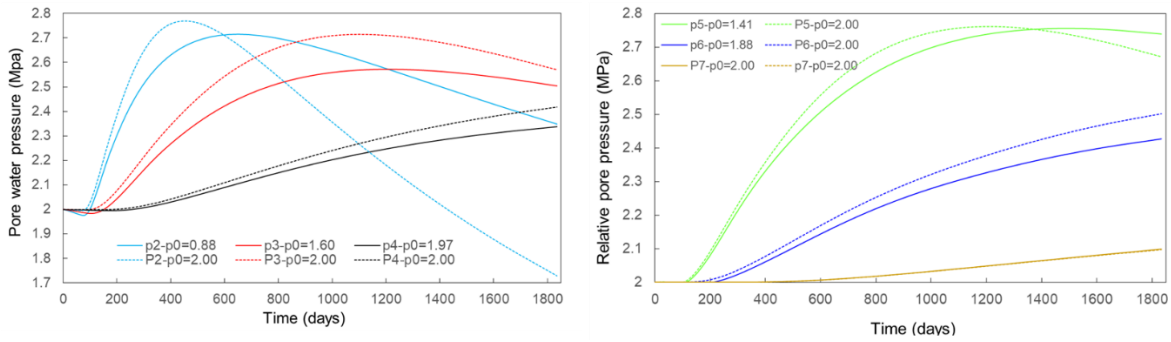

Figure 29: Effect of initial pore pressure on pore pressure change for bedding parallel (left) and bedding perpendicular (right) locations.

Several teams (NWMO, GRS, BGE/TUBAF, ENSI) also investigated the effect of different representations of the heater boundary condition. NWMO investigated several ways of applying the heat load (Guo and Briggs, 2024). They were:

- Applying the heat load at the inside surfaces of the heater cave without incorporating the heater, or
- Uniformly applying the heat load at the equivalent solid heater with an equivalent density and equivalent thermal parameters.

The challenge for simulating heat flow in the tunnel was the very different heat conductivity of the Granular Bentonite Mixture (GBM) and the bentonite blocks (Figure 30). The heat conductivity of the bentonite blocks is 2 times higher compared to the GBM which causes a higher heat flux per square meter into the bentonite blocks

compared to into the GBM. Representing these differences requires a volumetric source term definition for the heat flow.

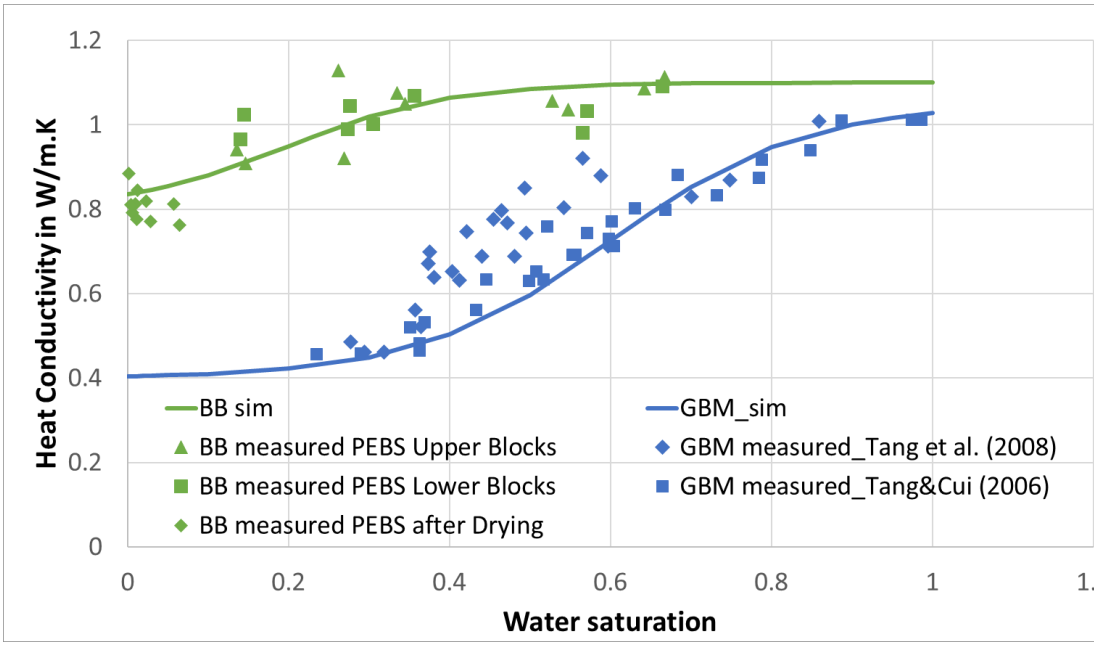

Figure 30: Comparison of measured values of heat conductivity for Granular Bentonite Mixture (GBM) and Bentonite Blocks.

Figure 31 shows the influence of equivalent thermal conductivity used for the heater on the heater surface temperature in a sensitivity case undertaken by NWMO (Guo and Briggs, 2024). The 'base case' in Figure 31 represented the model with detailed heater. Each detailed heater included three portions. The inside portion was a cylinder with a diameter of 940 mm and a length of 4.49 m in which heat power was applied. Around the inside heater there was a 20 mm air gap. Outside the air gap there was a 35-mm-thick steel protection cylinder shell which had an outside diameter of 1.05 m and a length of 4.6 m.

NWMO's sensitivity case compared the temperature output between using different equivalent thermal conductivity values and using a detailed heater model. The equivalent thermal conductivities were calculated based on the geometrical description above and assumed heat conductivities for the steel and the air. Using low equivalent thermal conductivity, e.g., TC=1.47 W/m/K, overestimated the heater temperature by about 11.3°C while using a high value (TC=43) underestimated the heater temperature by about 2°C at the location of H2-1. At location H2-4 the effect was less pronounced, with an overestimation of the heater temperature by about 5.5 °C for using a low equivalent thermal conductivity (TC=1.47 W/m/K), while using a high value (TC=43 W/m/K) led to an overestimation of about 0.4°C.

Application of heat load at the heater surface overestimated the temperature by about 12.5°C at the location of H2-1 while underestimating it by about 16.5°C at the location of H2-4. The reason was that application of heat load along the heater surface limited the adjustment of heat flow based on the heat flow gradients, compared to the detailed heater representation where the surface heat flux could vary along the heater surface depending on the different thermal conductivities of the surrounding material.

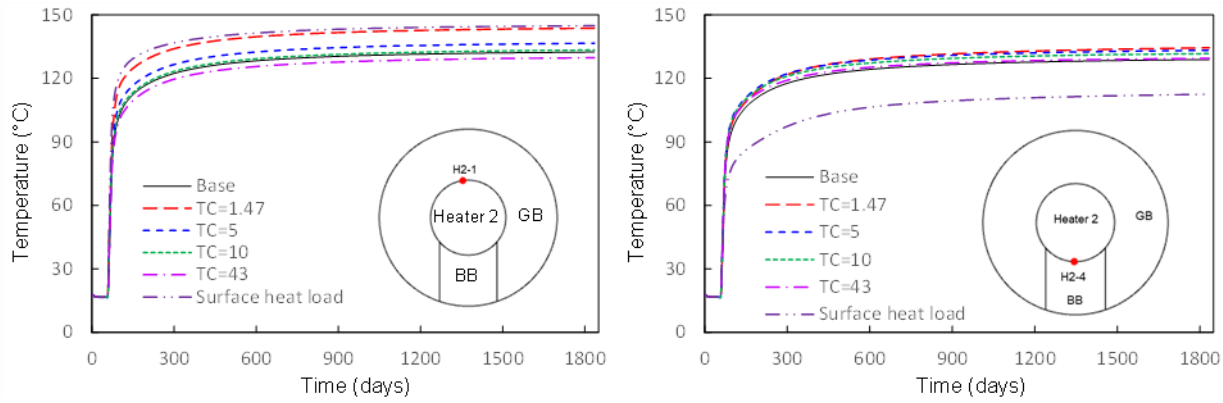

Figure 31: Influence of heat location application on temperature at heater surface

Although the influence of application of heat load was significant for the temperature development of the heater and in the buffer materials, the influence on the temperature of the surrounding rock is very minor (Guo and Briggs, 2024). The teams agreed that the temperatures in the Opalinus Clay are not sensitive to the representation of the heater. Therefore, different representations of the heater were possible.

5.4 Step 1b

Step 1b provided an opportunity for teams to consider how best to use the substantial amount of data from the FE experiment to inform and calibrate their models.

Data were available from a large number of sensors over a period from the start of excavation (2012) until August 2020 (or November 2021 for subset of sensors). Some measurement errors and apparently anomalous data points are noted in the data report (Firat Lüthi & Mussina, 2020). The measurement precision for temperature sensors is 0.3°C and for pressure sensors is 2.5 kPa. Discontinuities are seen in some pressure sensors in May 2019 due to excavation of a new gallery at Mont Terri.

BGE/TUBAF compared their modelling results to 200 sensors at different locations and measuring different variables. The experimental raw data was only coarsely screened to remove obvious measurement errors. The model results were interpolated to create a

result at each sensor location for each time in the data. The modelled and measured data were then compared relative to their starting values. A large number of models were run for comparison against the data, using different parameter values.

For these comparisons, the 5-year modelled duration as well as the measurement time series were split into sections of 0.5 years (with shorter 0.25 year sections at the start and end), and additionally the whole 5 years was considered as a single section. Then, the Index of Agreement (IA) (Willmott *et al.*, 2011) was calculated for every sensor, every time series section, every model run and every dimension in space (for displacement and strain):

$$IA = \begin{cases} 1 - \frac{\sum_{i=1}^{n}|M_i - D_i|}{2 \cdot \sum_{i=1}^{n}|D_i - \overline{D}|} & \text{if } (\sum_{i=1}^{n}|M_i - D_i|) \leq (2 \cdot \sum_{i=1}^{n}|D_i - \overline{D}|) \\ \frac{2 \cdot \sum_{i=1}^{n}|D_i - \overline{D}|}{\sum_{i=1}^{n}|M_i - D_i|} - 1 & \text{if } (\sum_{i=1}^{n}|M_i - D_i|) > (2 \cdot \sum_{i=1}^{n}|D_i - \overline{D}|) \end{cases} \quad (50)$$

where M stands for model and D for data.

The resulting 4D array was then aggregated in different ways. The final choice here was to use all sensors excluding the mechanical ones and all short time series sections together and to use means with equal weights over both the sensors and the time series sections. The "best" model fit was defined as the one with the highest value among all different runs.

Using this method, a single “best” model was picked with a particular set of parameter values. Additionally, the parameter values of models that had good fits according to the above criteria as well as other similar models were compared, to identify patterns that tended to lead to a better fit with the data. It was found that reducing the Biot Coefficient and Young’s Modulus in combination was likely to produce better fits to the data. Likewise, runs with changes to the Step 1a specification using the documentation of the FE experiment performed better against the data. Reducing the permeability anisotropy in the Opalinus Clay also resulted in better fits to the data.

This approach from BGE/TUBAF demonstrated how to handle and make use of larger volumes of data. However, the chosen best model fit described above was one with unrealistic parameter variations. Based on this, 82 additional model runs were done, varying the parameters in a way that was now aimed to be more physical. The run that was the best fitting according to the above-described method was finally picked out of these new model runs, and used as basis for BGE/TUBAF’s model in the next step.

5.5 Step 1c

5.5.1 Modelling strategy

The teams followed the same modelling strategy as for Step 1a, apart from the changes documented below. The heater representations, the domain size and the number of nodes/elements of the grids are presented in Table 10.

For Step 1c, teams were invited to update their initial conditions to fixed temperatures of 18°C in the bentonite and 16.5°C in the Opalinus Clay. Teams were also invited to calibrate the parameters in their models to better represent the observations from the FE experiment. Many teams chose to use lower thermal conductivity in the Opalinus Clay and GBM, whilst increasing thermal conductivity in the bentonite blocks (Table 11). All teams reduced the hydraulic conductivity of the Opalinus Clay in the bedding parallel direction, but teams both increased and reduced hydraulic conductivity in the bedding perpendicular direction (Table 11). Teams that calibrated the hydraulic properties of the bentonite chose lower entry pressure for the GBM and higher for the blocks as well as lower permeability in the GBM and higher in the blocks (Table 11).

Table 10: Domain sizes chosen by teams for Step 1c.

Team	Heater representation	Domain size (m)	Number of nodes/ elements
BGR/UFZ	Surface boundary	150 x 100 x 150	120,000/720,000
BGE/TUBAF	Surface boundary (complete surface)	200 x 200 x 200	210,977 / 1,267,770
CAS	Thin-walled cylinder	100 x 100 x 55	226703 / 214240
DOE/LBNL	Solid volume	150 x 150 x 150	64,158 / 67,627
ENSI	Solid volume	150x100x150	110,405 / 644,554
GRS	Solid volume	100 x 100 x 49.3	44,368/259,244
KAERI/KIGAM	Surface boundary	100 x 60 x 100	38,403 / 71,710
NWMO	Solid volume	100 x 90 x 100	140,888/269,371
DOE/SNL	Solid volume	50 x 50 x 50	1,497,366 elements

Teams had different approaches to calibration. Some used more automated methods such as evolutionary neural networks (CAS) and index of agreement (BGE/TUBAF) while others visually examined the fit of the results.

Table 11 shows the range of parameters chosen by the teams after calibration in Step 1c compared to the prescribed parameters. Appendix B shows in detail the calibrated parameters of each team for Opalinus Clay, Granular Bentonite Mixture and Bentonite Blocks.

Table 11: Range of finally chosen parameters used by the teams after calibrating the models in Step 1c

Input parameters		Symbol	Unit	OPA	Teams parameter range	GBM	Teams parameter range	Bentonite blocks	Teams parameter range	Source
Thermal parameters	Dry thermal conductivity parallel and perpendicular to bedding	$\lambda_{dry,\parallel}$	*W/mK*	2.4	1.71 - 2.45	0.35	0.26 - 0.4	0.26	0.26 - 1	
		$\lambda_{dry,\perp}$	*W/mK*	1.3	0.94 -1.3					
	Saturated thermal conductivity parallel and perpendicular to bedding	$\lambda_{sat,\parallel}$	*W/mK*	2.4	1.71 - 2.45	1.2	1 - 1.16	0.96	0.87 - 1.3	
		$\lambda_{sat,\perp}$	*W/mK*	1.3	0.94 - 1.3					
	Solid specific heat capacity	c_s	J/kgK	995	995	800	800	800	750 - 800	
Hydraulic parameters	Dry Bulk Density	ρ_{bulk}	*kg/m³*	2340	2340	1490	1490	1690	1690	NTB 15-02
	Porosity	ϕ	-	0.13	0.13 - 0.17	0.331	0.331 - 0.45	0.331	0.331 - 0.36	
	Intrinsic permeability	$k_{i,\parallel}$	*m²*	1.6E-20	6.2E-21 - 1E-19	3.5E-20	3.5E-21 - 3.5E-20	1.0E-22	1E-22 - 1E21	
		$k_{i,\perp}$		1.0E-20	3E-21 - 5E-20					
	van Genuchten Entry Pressure	p_e	*MPa*	20.0	12 - 20	28.6	10 - 28.6	30	21.9 - 64	
	van Genuchten n	n	-	2.5	1.4 - 2.5	2.0	1.67 - 2.0	1.67	1.43 - 1.67	
	van Genuchten maximum water saturation	s_{max}	-	1.0	1.0	1.0	1.0	1.0	1.0	
	van Genuchten residual water saturation	s_r	-	0.0	0.0	0.0	0.0	0.0	0.0	
	Pore compressibility	c_{pore}	*1/Pa*	-	"-" or 5.13E-10 - 2E-9	-	"-" or 1.05E-7 - 6.95E-7	-	"-" or 1.13E-07 - 3.74E-7	calculated from E, ν
Mechanical parameters	Young's modulus	$E_\parallel$	*MPa*	8000	1600 - 8000	18	18	24	24	
		$E_\perp$		4000	800 - 4000					
	Shear modulus	$G_\perp$	*MPa*	3500	880 - 3500	-	0	-	0	
	Poisson ratio	$\nu_\parallel$	-	0.35	0.35	0.35	0.35	0.2	0.2	
		$\nu_\perp$		0.25	0.25					
	Linear thermal expansion	α_T	*1/K*	1.5E-05	1E-5 - 1.5E-5	3.0E-06	3.0E-06	3.0E-06	3.0E-06	
	Biot coefficient	α	-	1	0.6 - 1	1	1	1	1	
Fluid parameters	Reference water density	ρ_{fluid_ref}	*kg/m³*	1000						
	Fluid compressibility	c_{fluid}	*1/Pa*	4.65E-10						
	Linear thermal expansion water	α_w	*1/K*	4.00E-04						
	Vapour diffusivity (vapour in air)	D_v	*m²/s*	2.42E-05						

BGR/UFZ

No additional change, only parameters were calibrated. The initial capillary pressure in bentonite blocks and pedestal was adjusted to match initial measurements for relative humidity.

DOE/LBNL

For Step 1C DOE/LBNL changed the temperature and pressure dependent water properties to use steam tables. Furthermore, model results included a low permeability barrier at the rock wall representing the shotcrete that impacted the pore pressure evolution in the Opalinus Clay.

ENSI

ENSI included the heaters as a volumetric source term with an overall heat conductivity of 1.5 W/mK based on the calculations shown in Figure 32. Figure 33 shows the resulting model geometry.

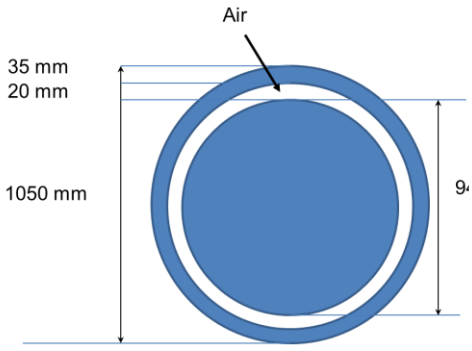

	Layer Thickness d [m]	Heat conductivity lambda [W/m.K]	Heat resistance R [W/m2.K]	
Steel	0.47	50	0.0094	=d/lambda
Air	0.02	0.0262	0.7634	=d/lambda
Steel	0.035	50	0.0007	=d/lambda
Total	0.525	**1.4733**	0.7735	=Rgesamt/dgesamt

Figure 32: Structure of the Heater and calculation of the average heat conductivity

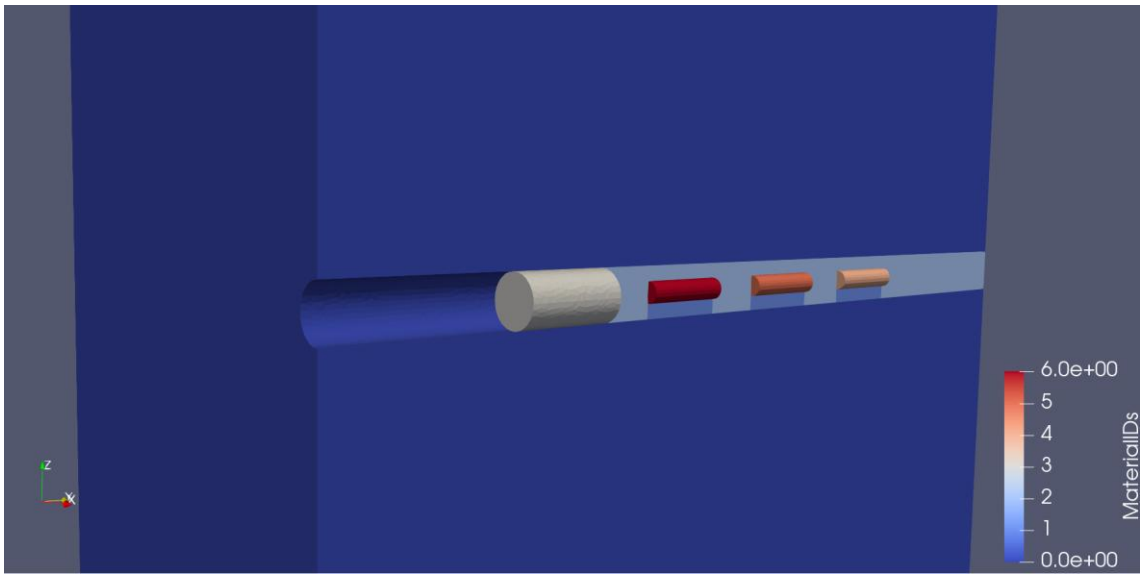

Figure 33: Heaters represented as cylinders in the mesh of the ENSI model

GRS

The material parameters were modified, based on the GRS experience with the modelling of Mont Terri in-situ experiments. Retention curves and permeabilities for the Opalinus Clay, the granular bentonite and the bentonite blocks were adapted, respectively. Further, the thermal conductivities for the Opalinus clay and the granular bentonite were adjusted.

KAERI/KIGAM

Based on Nagra's experimental data, KAERI/KIGAM changed the thermal conductivity of granular bentonite and bentonite block. Also, the team changed some hydraulic properties of the Opalinus Clay and bentonite material for the calibration. First, the compressibility of 8.66e-10 and Biot coefficient of 0.6 were applied to the Opalinus Clay based on the provided specifications. Pore compressibility affects the flow rate, and the Biot coefficient was modified considering soft bentonite. We changed the entry pressure in the van Genuchten curve parameters for the bentonite material. Entry pressure can affect the capillary pressure depending on the saturation in the two-phase flow system, and thus, the two-phase flow rate might change depending on the parameter.

NWMO

NWMO's model in Step 1c included the heaters with detailed structures as shown in Figure 5.9. There were no other changes made in this step other than to parameter values (including a very low Young's modulus for the Opalinus Clay – which could be justified as representing the plastic yielding of the Opalinus Clay).

BGE/TUBAF

Aside from parameter adjustments as a result of fitting, some EOS were altered. Febex vapor diffusion models which are dependent on temperature, saturation and tortuosity were used. Water density was represented by a non-linear temperature dependence and compressibility effects only taken into account for positive pore water pressures, i.e. in the saturated state.

DOE/SNL

For Step 1c the SNL-PFLOTRAN team used material and fluid properties that are part of the PFLOTRAN code (Hammond *et al*., 2014). For TH simulations, water and steam properties Equation-of-State (EOS) from the International Formulating Committee (IF97, 1997) were used. Water density, steam density and enthalpy were calculated as a function of temperature and pressure. Viscosity was calculated as a function of temperature, pressure, and saturation pressure. Vapor diffusion was a function of pressure and temperature. The diffusion coefficient was calculated using the equation by Vargaftik (1975) and Walker *et al*. (1981).

The relation for thermal conductivity as a function of saturation given in Equation (2) as well as the default function in PFLOTRAN were used. The default thermal conductivity equation in PFLOTRAN is (Somerton *et al*., 1974):

$$\lambda_{th} = \lambda_{dry} + \sqrt{s}(\lambda_{sat} - \lambda_{dry}) \quad (51)$$

where,

λ_{th} = thermal conductivity

λ_{dry} = dry thermal conductivity

λ_{sat} = fully saturated thermal conductivity

Figure 34 illustrates the differences in thermal conductivity equations, with higher differences at low liquid saturations.

In PFLOTRAN heat capacity was represented as a constant value.

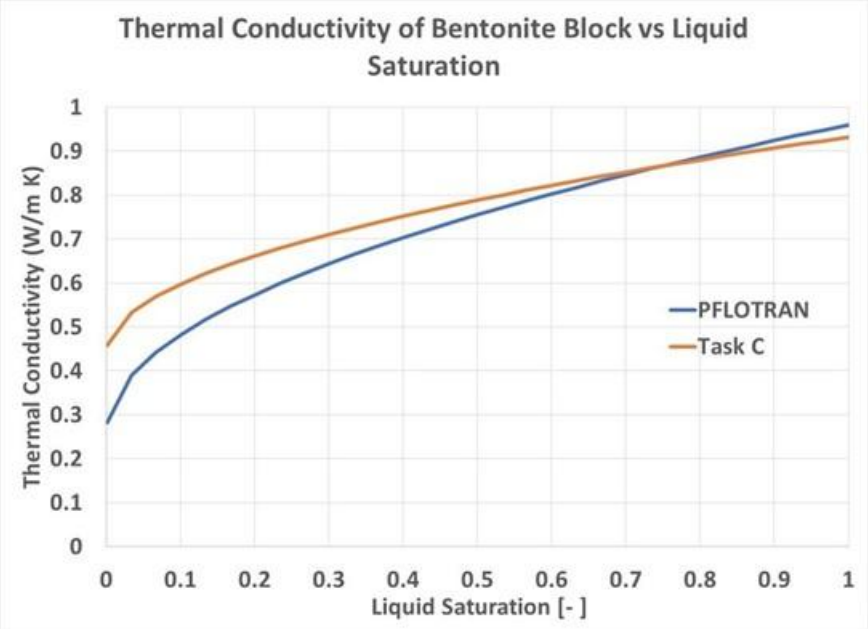

Figure 34: Comparison of thermal conductivity as a function of liquid saturation equations: PFLOTRAN default method vs Task C specified.

For Step 1c, a new mesh was built that includes the shotcrete. The domain size was 50 m x 50 m x 50 m. A 30 cm thick shotcrete was introduced represented by two elements in the radial direction. Mesh refinements were applied in selected areas to get better resolution. These include the tunnel area and locations of observation points. The finite volume method used in PFLOTRAN means that solutions are evaluated at cell centers, which could be different from observation point locations. To reduce the discrepancy, smaller cell sizes were used. In addition, interpolation methods were used when necessary. The mesh size is 1,497,366 elements. For the PFLOTRAN simulations, a high-performance computing system was used to solve the mass and energy equations on the large mesh size. For each PFLOTRAN run up to 320 processors were used.

For Step 1c, shotcrete calibrated properties were a permeability of 2E-21 m^2 and dry and wet thermal conductivity of 0.3 and 0.5 W/m K, respectively.

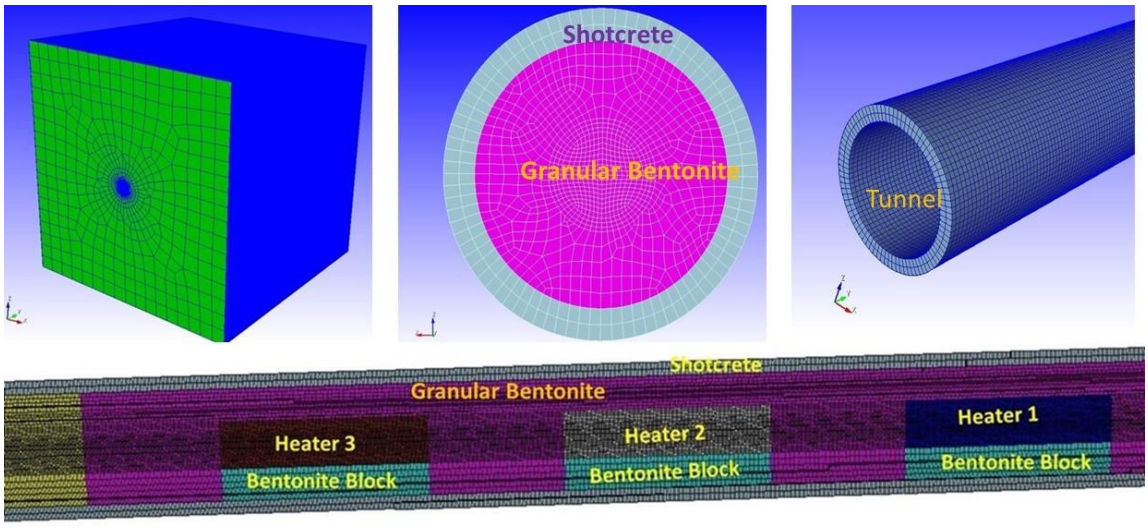

Figure 35: SNL mesh used for Step 1c and Step 2 TH simulations .

5.5.2 Results

In the Opalinus Clay, the spread of modelled temperature results was similar in the calibrated results (Figure 36) to the calculations based on the prescribed parameters (Step 1a) (Figure 25), but the updated results in Step 1c were closer to the data from the experiment due to modification of the heat conductivity and the update of the initial temperatures. Results of most teams agreed well with measurements in the Opalinus Clay with lower agreement for the sensors close to the heater.

In the Opalinus Clay, the spread of modelled pressure results was similar in the calibrated results (Figure 37) and the simulations of Step 1a (Figure 26), but the calibrated pressure results matched the data more closely. In particular, the calibrated models showed less drainage in the bedding parallel direction, consistent with the data and lower pressure in the bedding perpendicular direction, again consistent with the data. Once again, NWMO produced particularly close matches of the data, but with parameterisation (Young's Modulus) that was outside what was expected of the Opalinus Clay.

Within the bentonite, the spread of modelled temperature results was slightly larger in the calibrated models (Figure 38) compared to the simulations of Step 1a (Figure 27), but the teams generally matched the data better, with higher temperatures due to the lower thermal conductivity of the Opalinus Clay. Furthermore, some teams used a volumetric source term which supports a better fit of temperatures in granular bentonite mixture and bentonite blocks.

The relative humidity in the bentonite was slightly more consistent between the models in the calibrated results (Figure 39) than in the simulations of Step 1a (Figure 28) and was also more consistent with the data in the calibrated results. In particular, the relative humidity from days 600 – 1000 was better captured in the GBM and the initial relative humidity was better captured in the bentonite block.

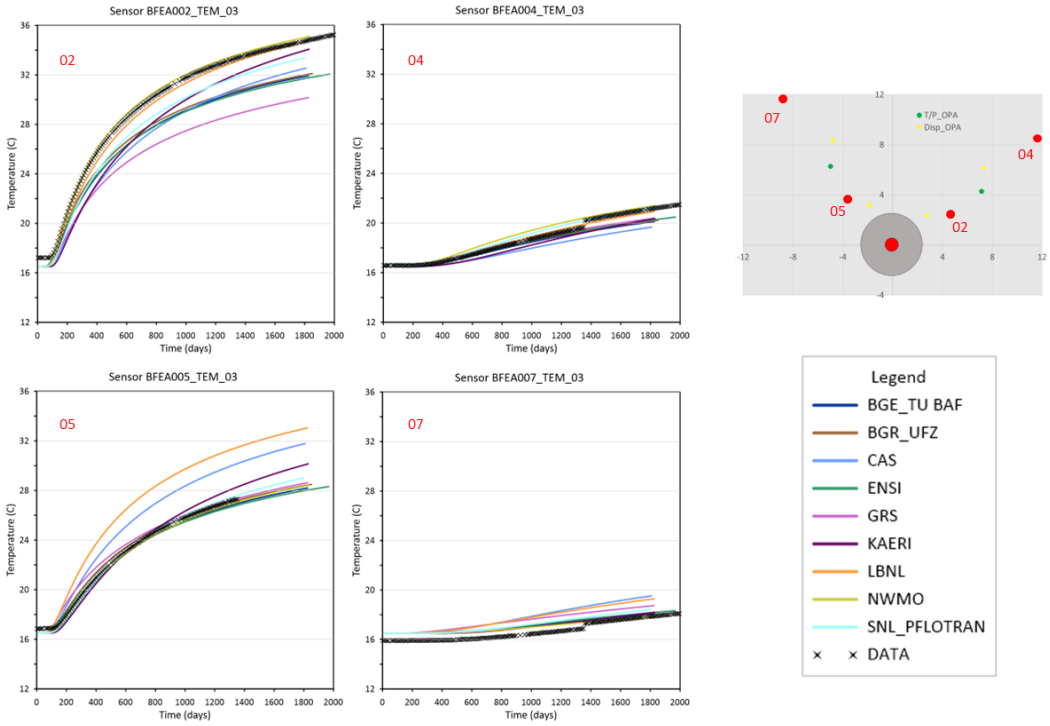

Figure 36: Selected temperature results for locations in the Opalinus Clay from Step 1c.

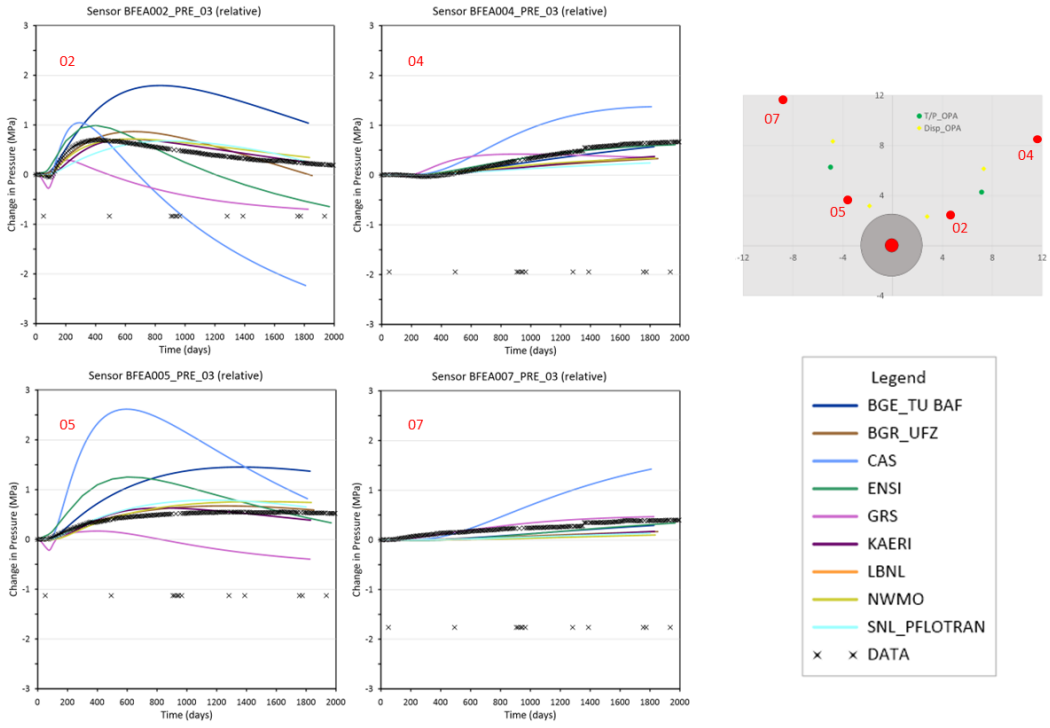

Figure 37: Selected pressure results for locations in the Opalinus Clay from Step 1c.

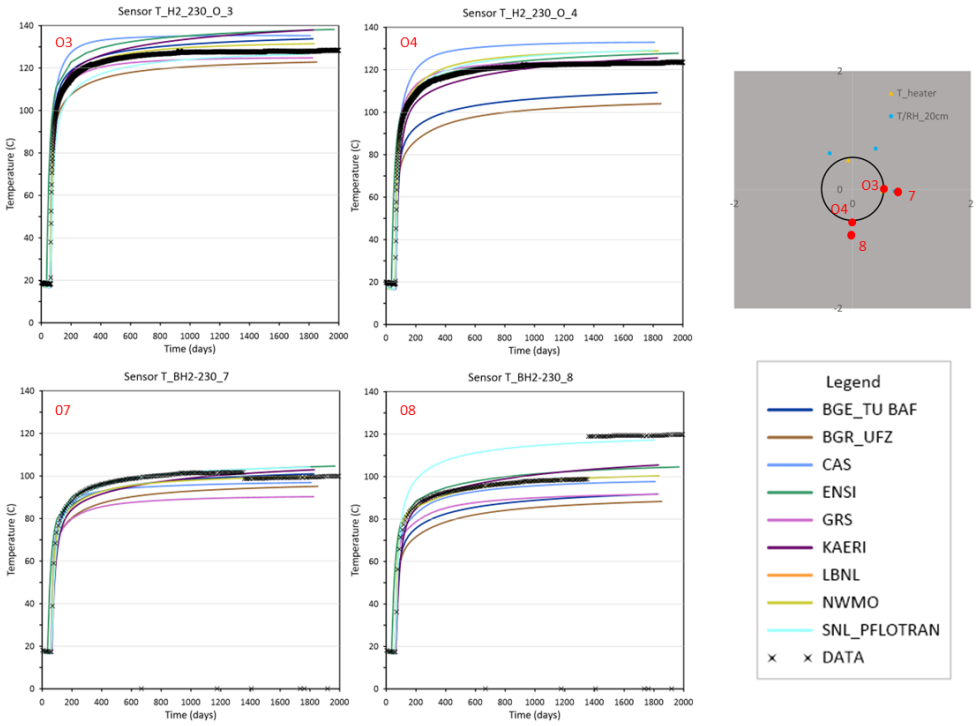

Figure 38: Selected temperature results in the bentonite from Step 1c.

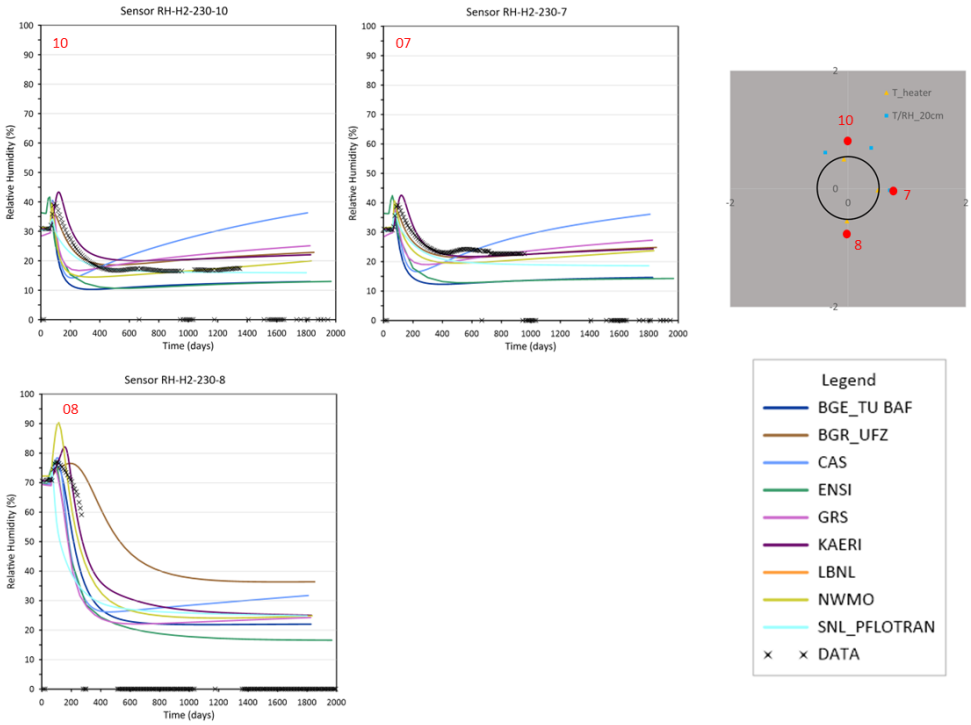

Figure 39: Selected relative humidity results in the bentonite from Step 1c.

5.5.3 Discussion

The teams improved the fit of their model to the data during this calibration exercise. Some teams even found a very close agreement with the measurements. However, the range of the results remained relatively high especially for the results of pore pressure. This indicated that the discrepancies between the models and the observations could not be explained by material parameters alone (Buchwald et al., 2024). Most teams still needed to reduce drainage into the tunnel without decreasing permeability because decreasing permeability causes higher fluid pressure. Due to the low compressibility of water, small changes in deformation and drainage conditions can lead to large variations in water pressure. Capturing flow into the unsaturated bentonite at high suctions is associated with initially steep gradients and is sensitive to the parameters used for retention and relative permeability curves. NWMO did find a parameter set that could reproduce the observations, but the Young's modulus was outside the expected range for the Opalinus Clay. Low values of Young's Modulus were used to consider the plastic yielding of the Opalinus Clay.

This difficulty in calibrating the models pointed toward missing features or processes in the models. Teams highlighted potential additional features as the inclusion of the EDZ and shotcrete and potential additional processes to be excavation and ventilation of the tunnel. Bentonite permeability and retention curves strongly depend on the multi-scale pore structure, and thus on compaction and swelling. As the focus of this series of simulations was on thermally-induced pore water pressurization, it was decided early on not to focus on bentonite behaviour. Neglecting the strong saturation dependence of bentonite, the alteration of its hydraulic properties by swelling (upon water uptake from the host rock) and shrinkage (dry out near the heater) and the effect of developing swelling pressures on the mechanical and hydraulic properties of the EDZ may thus have contributed to the teams' difficulties in capturing the behaviour in the immediate vicinity of the tunnel contour.

6 Step 2 – FE experiment: from ventilation to heating

6.1 Aim

Step 2 moved towards a more complete representation of the FE experiment, allowing teams to add additional features and materials, as well as representing the excavation and ventilation of the tunnel prior to the onset of heating. This allowed teams to calculate the initial pressure distribution in the Opalinus Clay before heating starts and the results comparison focussed on absolute pressures in the Opalinus Clay, rather than pressure changes, as were considered for Step 1.

6.2 Model specification

The model specification from previous steps was still relevant in Step 2. In addition, teams were provided with information on the experiment schedule prior to heating (Table 12) along with the measured conditions in the tunnel during ventilation (Figure 40). Teams were asked to report results such that the onset of heating (15.12.2014) is time zero in the results, with the ventilation period being at negative times. The teams were left to choose when to start the model.

Table 12: Experiment schedule (Lanyon et al., 2020)

	Date
Start of excavation	26.04.2012
End of excavation	11.07.2012
Start of backfilling	04.07.2014
Backfill around H1	23.10.2014
Backfill around H2	20.11.2014
Backfill around H3	21.01.2015
Concrete plug emplacement	17.03.2015
Start of heating	15.12.2014

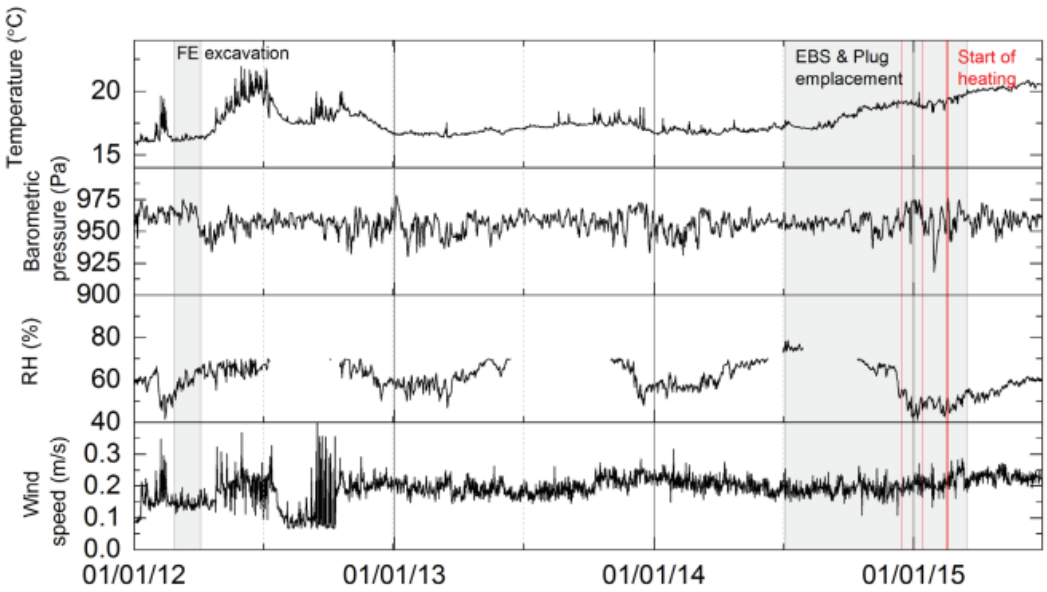

Figure 40: Conditions inside the tunnel during ventilation (Lanyon et al., 2020)

6.3 Modelling strategy

The teams followed the same modelling strategy for Step 2 as for Step 1c, with any differences outlined below. The heater representations, the domain size and the number of nodes/elements of the grids are presented in Table 13.

All teams represented the ventilation phase of the FE experiment. Five teams (BGR/UFZ, BGE/TUBAF, CAS, ENSI and GRS) chose to represent the ventilation of the tunnel by applying a suction pressure as a boundary condition on the tunnel wall. The suction pressure was related to the relative humidity in the tunnel by the Kelvin equation (Eqn. (18)). Teams chose different suctions as shown in Table 14 and ventilated the tunnel for different amounts of time. Two teams (KAERI and NWMO) applied a boundary condition of atmospheric pressure to the tunnel walls and one team (SNL) applied an atmospheric boundary condition for the gas phase at the end of the tunnel and assumed the tunnel was filled with high permeability high porosity material. Most teams that applied a suction boundary on the tunnel surface used relatively low values of suction that do not correspond to the measured relative humidity in the tunnel, but it was needed to reproduce the slow and light decrease in porewater pressure in the Opalinus Clay. This could be explained by the presence of a boundary layer at the tunnel wall where the relative humidity was higher and suction was thus lower (consistent with the finding of Bond et al., 2013).

Two teams (ENSI and NWMO) included the excavation of the tunnel in their model, with ENSI simulating excavation over 100 days and NWMO assuming instantaneous excavation. Both models assumed linear elasticity in the Opalinus Clay, so the excavation did not produce a damage zone but changed the stresses and pore pressures in the Opalinus Clay. BGR/UFZ also investigated simulation of excavation using a linear elastic model, but concluded that it didn't explain satisfactorily the early liquid pressure drop from the initial 2 MPa visible in the field measured right after excavation. Therefore, they chose to postulate an initial pressure field (with lower pressures near the tunnel and with an elliptical shape to take into account the anisotropy in the permeability) to match measurements at $t = -900$ days, while acknowledging that processes taking place before that could not be explained by the chosen modelling approach. During the ventilation phase, no large pressure changes were measured in the host rock.

Three teams included an EDZ (BGE/TUBAF, KAERI and NWMO). BGE/TUBAF assumed different thicknesses in different directions related to the bedding in the Opalinus Clay and depending on the presence or absence of shotcrete at the tunnel wall. The other two teams used uniform thicknesses (Table 15). The EDZ was modelled with higher permeability and lower Youngs' Modulus than the Opalinus Clay (Table 15).

Most teams chose to represent shotcrete lining the tunnel with thicknesses around 20 cm, but had different values for EDZ permeability, with a range of $1x10^{-17}$ to $1x10^{-21}$ m^2.

Once the additional features were added, some teams chose to revisit the parameter calibration from Step 1c, with updated calibrations shown in Table 16 and Appendix C.

Table 13: Domain sizes chosen by teams for Step 2.

Team	Heater representation	Domain size (m)	Number of nodes/ elements
BGR/UFZ	Surface boundary	150 x 100 x 150	120,000/720,000
BGE/TUBAF	Heater volume	200 x 200 x 200	475313 / 2909597
CAS	Thin-walled cylinder	100 x 100 x 55	226703 / 214240
DOE/LBNL	Solid volume	150 x 150 x 150	64,158 / 67,627
ENSI	Solid volume	150x100x150	99,397 / 597,634
GRS	Solid volume	100 x 100 x 49.3	29,895/27,910
KAERI/KIGAM	Surface boundary	100 x 60 x 100	44,586 / 85,080
NWMO	Solid volume	100 x 90 x 100	140,888/269,525
DOE / SNL	Solid volume	50 x 50 x 50	1,497,366 elements

Table 14: Boundary conditions used to represent ventilation of the tunnel

Team	Boundary condition	Modelled duration of ventilation
BGR/UFZ	69.0 MPa suction at tunnel wall (60% RH)	2.5 years
BGE/TUBAF	57.2 MPa suction (65% RH)	2.5 years
CAS	57.4 MPa suction (65% RH)	2.5 yrs
ENSI	2 MPa suction 98.5% RH	2.5 yrs
GRS	2 MPa suction	2 years
KAERI/KIGAM	Atmospheric pressure	3 yrs
LBNL	2 MPa suction	3 yrs
NWMO	Atmospheric pressure	3 yrs
SNL	Atmospheric pressure on tunnel end assigned to the gas phase. Tunnel has permeability of 1E-12 m^2 and porosity of 0.9	1000 days

Table 15: Additional materials in the Step 2 model

Team	EDZ	Shotcrete
BGR/UFZ	none	20 cm thick Intrinsic permeability 1E-17 m^2
BGE/TUBAF	Parallel 2 m (0.8 m where shotcrete) thick Perp 2.5 m (1.0 m where shotcrete) thick Perm 5E-19 m^2 parallel 3.5E-19 m^2 perp YM 3.6 GPa parallel 1.8 GPa perp	16-24 cm thick (changes along tunnel) Permeability 1.15E-17 m^2 Thermal conductivity 1.06 – 1.7 W/mK YM 21.5 GPa
CAS	No	No
ENSI	No	25 cm thick, 1.75E-19 m^2
GRS	None	None
KAERI/KIGAM	1.8 m circle 8E-18 m^2 parallel 6E-19 m^2 perp YM 4 GPa parallel 2 GPa perp	20 cm 1E-17 m^2
LBNL	No	18 cm Thick 3e-22 m^2
NWMO	3m thick Perm 20x greater than Opa Biot 0.6 YM 4 GPa parallel, 2 GPa perp	No
SNL	No	30 cm thick 2E-21 m^2

Table 16: Range of parameters used by the teams for Step 2

Input parameters		Symbol	Unit	OPA	Teams parameter range	EDZ	Teams parameter range	GBM	Teams parameter range	Bentonite blocks	Teams parameter range	Shotcrete	Teams parameter range
Thermal parameters	Dry thermal conductivity parallel and perpendicular to bedding	$\lambda_{dry,\parallel}$	*W/mK*	2.4	1.71 - 2.5	2.4	2.4	0.35	0.23 - 0.4	0.26	0.26 - 1	1	0.1 -1.7
		$\lambda_{dry,\perp}$	*W/mK*	1.3	0.94 - 1.3	1.3	1.3						
	Saturated thermal conductivity parallel and perpendicular to bedding	$\lambda_{sat,\parallel}$	*W/mK*	2.4	1.71 - 2.5	2.4	2.4	1.2	1.0 - 1.16	0.96	0.87 - 1.3	1.7	0.3 - 1.7
		$\lambda_{sat,\perp}$	*W/mK*	1.3	0.94 - 1.3	1.3	1.3						
	Solid specific heat capacity	c_s	J/kgK	995	995	995	995	800	800	800	750 - 800	750	750
Hydraulic parameters	Dry Bulk Density	ρ_{bulk}	kg/m^3	2340	2340	2340	2311 - 2340	1490	1490	1690	1690	1725	1725 - 2300
	Porosity	ϕ	-	0.13	0.13 - 0.17	0.13	0.13 - 0.18	0.331	0.331 - 0.45	0.331	0.331 - 0.36	0.25	0.23 - 0.25
	Intrinsic permeability	$k_{i,\parallel}$	m^2	1.6E-20	6.2E-21 - 4E-20	5.0E-20	5E-19 - 8E-19	3.5E-20	3.5E-21 - 3.5E-20	1.0E-22	1E-22 - 2E-21	1.00E-19	2E-21 - 1.15E-17
		$k_{i,\perp}$		1.0E-20	2.5E-21 - 3E-20	1.0E-20	3.5E-19 - 5.6E-19						
	van Genuchten Entry Pressure	p_e	*MPa*	20.0	12 - 20	20	20	28.6	10.0 - 30.0	30	21.9 - 64	1	1.0 - 20.0
	van Genuchten n	n	-	2.5	1.4 - 2.5	0.6	1.4 - 2.5	2.0	1.67 - 3.0	1.67	1.43 - 1.67	1.49	1.49 - 2.5
	van Genuchten maximum water saturation	s_{max}	-	1.0	1.0		1.0	1.0	1.0	1.0	1.0	1	1
	van Genuchten residual water saturation	s_r	-	0.0	0.0		0.0	0.0	0.0	0.0	0.0	0.01	0.01
	Pore compressibility	c_{pore}	*1/Pa*	-	"-" or 5.13E-10 - 8.66E-10		"-" or 8.66E-10	-	"-" or 1.05E-7 - 1.05E-6	-	"-" or 1.13E-7 - 2E-6	-	"-" or 3.5E-12 - 1.4E-10
Mechanical parameters	Young's modulus	$E_\parallel$	*MPa*	8000	1600 - 8000	6000	3600 - 4000	18	18	24	24	20000	20000 - 21500
		$E_\perp$		4000	800 - 4000		1800 - 2000						
	Shear modulus	$G_\perp$	*MPa*	3500	880 - 3500		3500	-	0	-	0	-	0
	Poisson ratio	$\nu_\parallel$	-	0.35	0.35	0.3	0.35	0.35	0.35	0.2	0.2	0.15	0.15
		$\nu_\perp$		0.25	0.25		0.25						
	Linear thermal expansion	α_T	*1/K*	1.5E-05	1E-5 - 1.5E-5	1.50E-05	1E-5 - 1.5E-5	3.0E-06	3.0E-06	3.0E-06	3.0E-06	1.50E-05	1.50E-05
	Biot coefficient	α	-	1	0.6 - 1	1	0.6 - 1	1	1	1	1	1	1
Fluid parameters	Reference water density	ρ_{fluid_ref}	kg/m^3	1000									
	Fluid compressibility	c_{fluid}	*1/Pa*	4.65E-10									
	Linear thermal expansion water	α_w	*1/K*	4.00E-04									
	Vapour diffusivity (vapour in air)	D_v	m^2/s	2.42E-05									

6.4 Results

In the Opalinus Clay, the spread of modelled temperature results in Step 2 (Figure 41) was significantly improved compared to Step 1c (Figure 36), with a good match to temperature at all sensors. Some teams underpredicted the temperature evolution parallel to bedding slightly. The initial temperature that CAS have used was higher than the agreed value.

The water pressure in the Opalinus Clay is given as absolute values in Figure 42, compared to pressure changes given in Step 1 (Figure 26 and Figure 37) since the teams moved to representing the ventilation period in Step 2, which improved the results, but involved artificially reducing drainage to the tunnel. Most team results agreed nicely with the measurements whereas some teams over- or underestimated the pressure increase due to heating for sensors close to the heater and several teams overestimate the drainage effect slightly compared to measurements. CAS was not able to reproduce the evolution of porewater pressures and reported very high water pressure values (up to 4.5 MPa). The teams that reported pressure values during ventilation consistently found that the pressure decreased faster in the models than in the data.

Within the bentonite, the majority of teams show good agreement with the data, particularly at the heater surface (Figure 43). BGR/UFZ and CAS have consistently too high temperatures in the bentonite (by 10-30°C) while GRS has too low temperature in the bentonite blocks (by 5-10°C).

The relative humidity in the bentonite is very consistent between the teams in terms of the shape of curve although the final relative humidity varies by 20%. All teams captured the initial increase in relative humidity at the onset of heating and the subsequent rapid decrease.

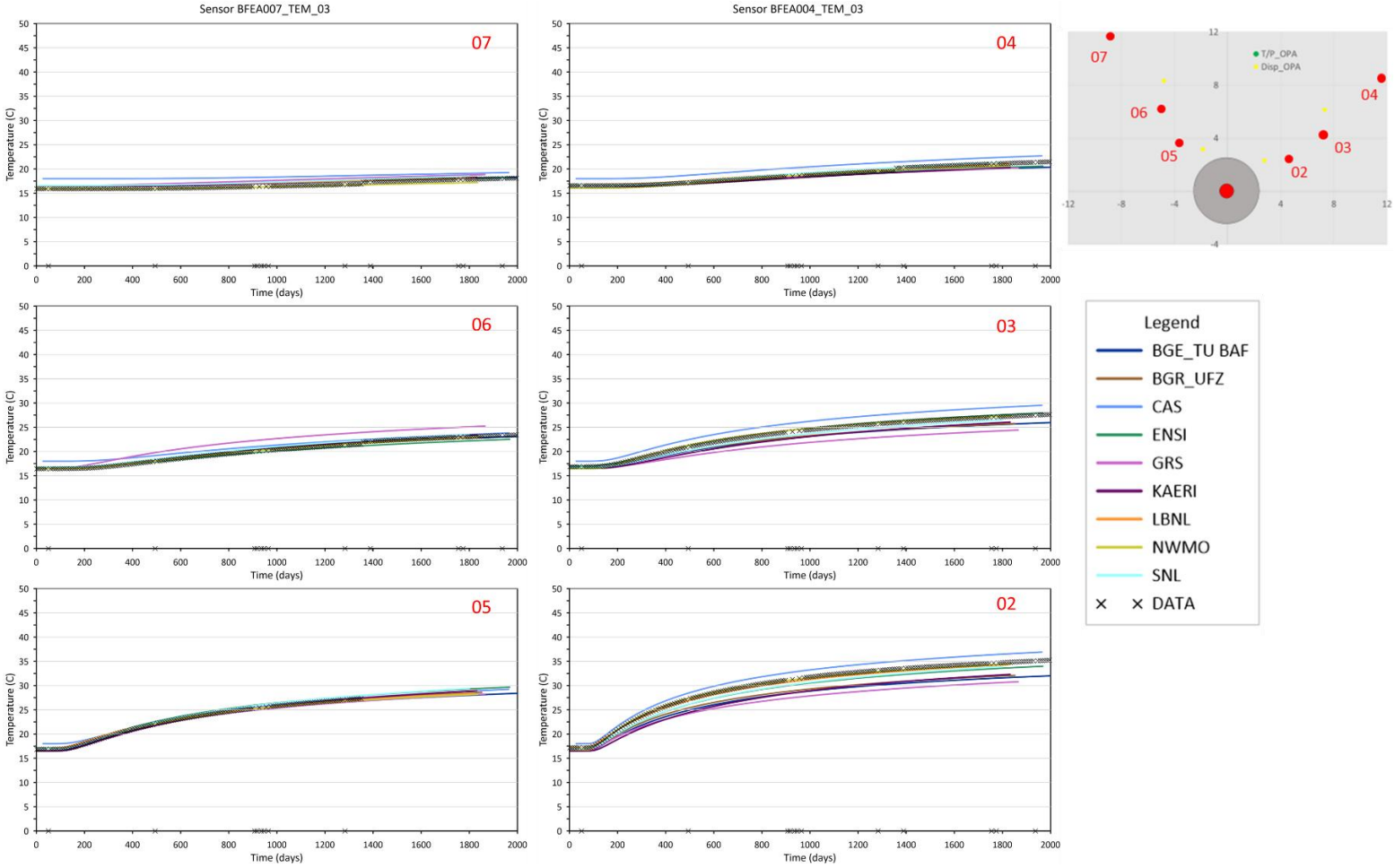

Figure 41: Selected temperature results for locations in the Opalinus Clay from Step 2.

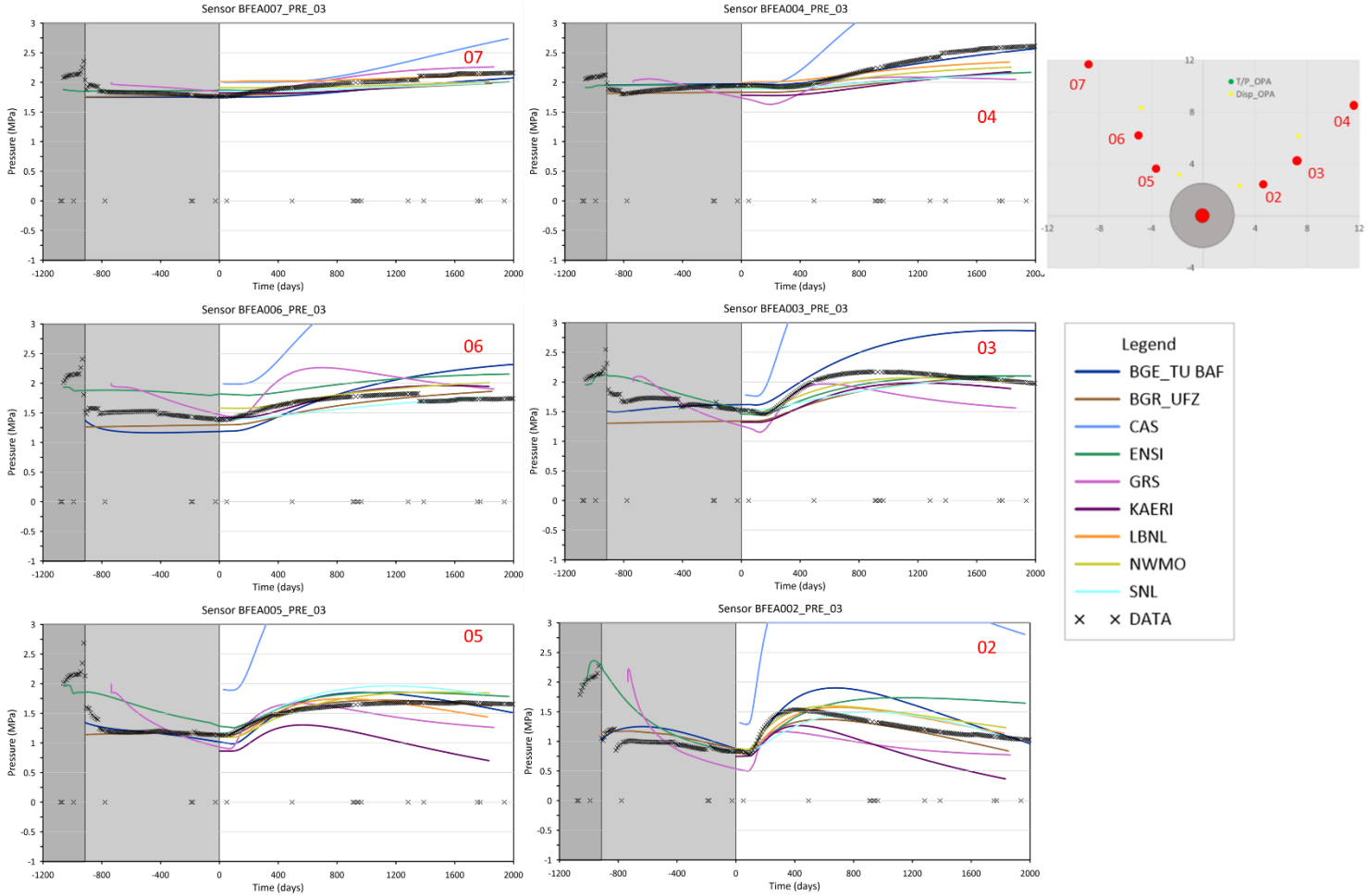

Figure 42: Selected pressure results for locations in the Opalinus Clay from Step 2.

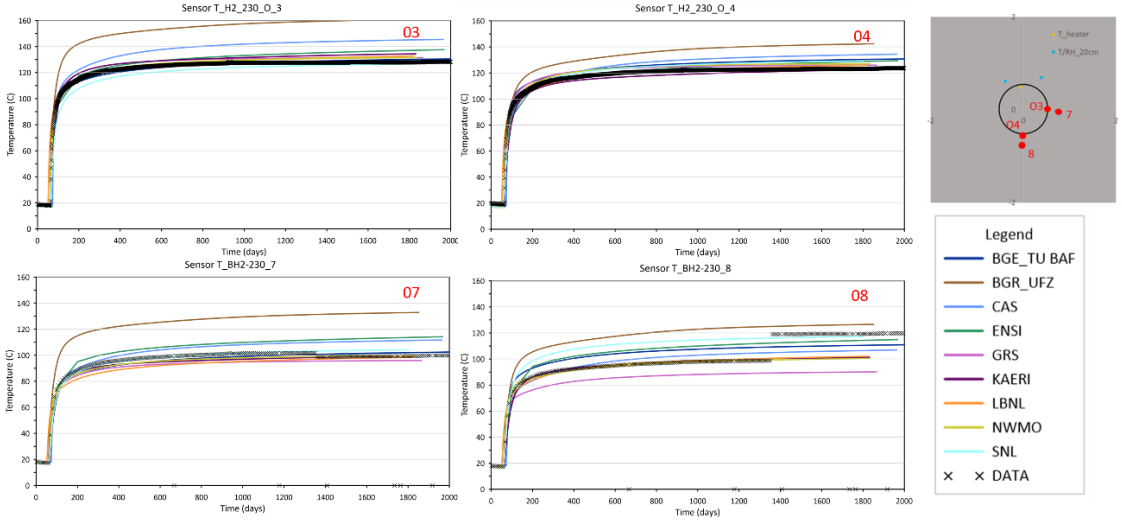

Figure 43: Selected temperature results for locations in the bentonite from Step 2.

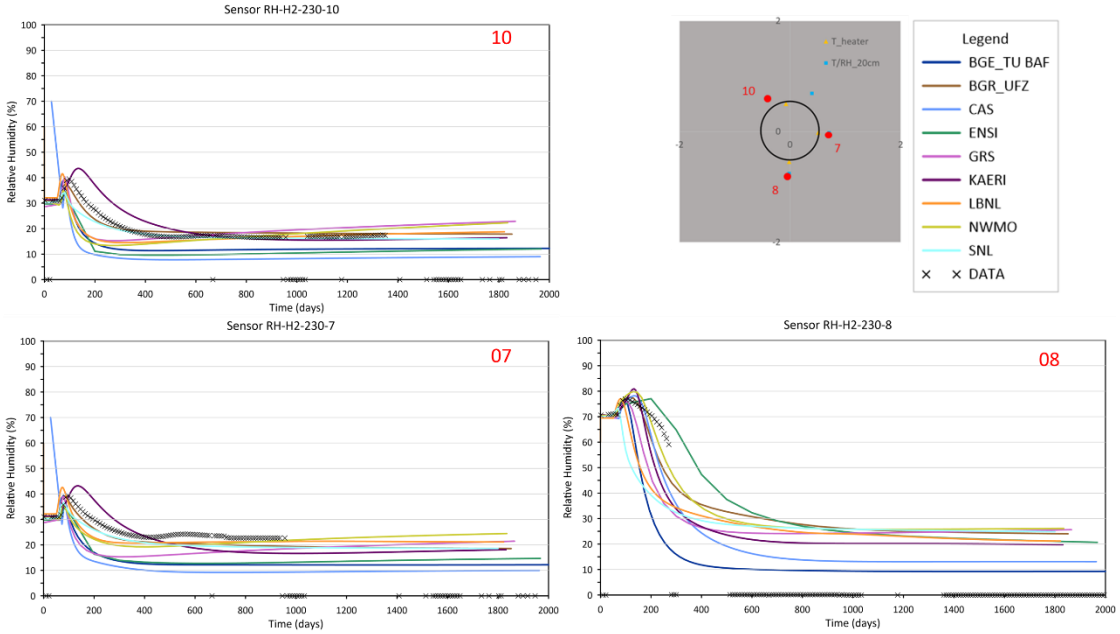

Figure 44: Selected relative humidity results for locations in the bentonite from Step 2.

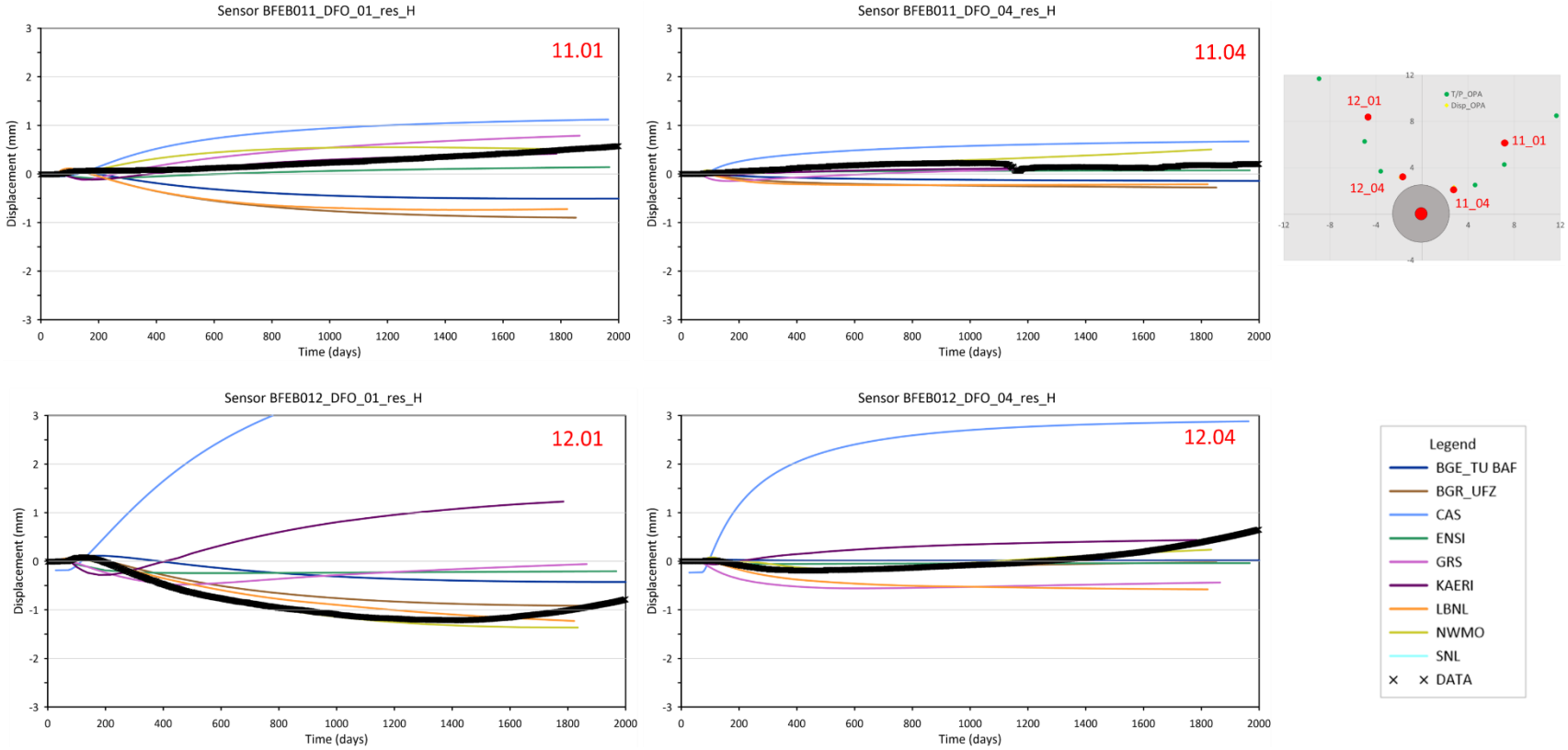

Figure 45: Selected displacement results for locations in the Opalinus Clay from Step 2

6.5 Discussion

The inclusion of additional complexity in the form of modelling excavation, ventilation, shotcrete and the EDZ improved individual teams' results, but there remains a significant spread between the teams. This may indicate that the missing features and/or processes that would help the models represent the data better were still not included in the models. Potential candidates could be a better representation of the failure of the Opalinus Clay during excavation and formation of the EDZ, as well as better representing the complexities of the bentonite buffer. However, moving to more complex models also increased the opportunity for conceptual and parametric differences between the different approaches. There was already a large set of inputs that contributed to model separation, some of which are discussed in Appendix D. Therefore, a higher spread in results compared to simpler models was to be expected. This is one of the major reasons for the value of well-constrained benchmarking studies when comparing complex process model implementations.

It is also interesting to note that although teams applied a range of boundary conditions to the tunnel wall during ventilation, there was generally agreement between the teams that the data showed less of an effect of ventilation in the Opalinus Clay than the models. This is potentially because the Opalinus Clay was disturbed already during excavation and the teams have not modelled this in detail, or the variation in relative humidity across the tunnel (especially boundary layers around the tunnel surface) may restrict water vapour loss from the tunnel walls.

The comparison of porewater pressure evolution in Opalinus Clay shows larger discrepancies between measurements and models closer to the tunnel contour. The models either overpredicted the pressure increase, or overpredicted the drainage effect. With increasing distance, the discrepancies decreased and at the sensors farthest away from heater the models tended to underpredict the pressure evolution. Potential reasons for this could be interactions with other experiments, variations in the reference stress or water pressure fields, or deformations of the rock mass during excavation that were not correctly considered in the models. Those changes seem to limit the temperature driven pressure increase and the drainage of Opalinus Clay.

Another finding is that relatively low values for the Young's modulus helped to have a better agreement with the porewater pressure increase closer to the heater. Figure 46 shows the effect on the porewater pressure for the ENSI results if the Young's modulus

is reduced from 60 % (4800 MPa parallel and 2400 MPa perpendicular) to 20 % (1600 MPa parallel and 800 MPa perpendicular). While the selection of a value as low as 60 % of the original provided Young's modulus would be supported by findings of (Winhausen et al. 2022), selecting an even lower value cannot be justified by tests in the laboratory or might be indicative of inelastic effects. Figure 47 presents all teams that used a value of 20 – 30 % of the original provided data for Young's modulus. The comparison with measurements suggested that choosing such a low value for the Young's modulus could by justified based on the in-situ experiment. This underpinned the interpretation that the rock mass around the FE tunnel seemed to behave in a less stiff manner closer to the tunnel and appeared stiffer further away from the tunnel. It is probably caused by rock damage processes during and after the excavation indicating a possible weak EDZ.

The EDZ, which was incorporated by some teams, could have provided the necessary degrees of freedom to reflect the effects of rock mass deformations during excavation. Three teams (BGE/TUBAF, KAERI and NWMO) modelled the EDZ, but while NWMO's results agreed well with the measurements, BGE/TUBAF's results tended to overpredict the pressures, and KAERI's results tended to underpredict them. The three teams have used similar parameterisations for the EDZ but the pressure results do not show a consistent trend. This could be due to other differences between the teams' models such as choice of Youngs' Modulus for the Opalinus Clay, the inclusion of shotcrete for BGE/TUBAF or KAERI needing to use the pore compressibility instead of a fully coupled THM model. Representation of the EDZ as an elastic material is a significant simplification of the known features of the EDZ. The EDZ has an internal structure dependent on the anisotropy of both stress field and material properties and shows incremental non-linearity, i.e. different values for differing loading and unloading stiffness. There is some indication from NWMO's work that a simplified representation of the EDZ is sufficient for understanding pore pressures within the Opalinus Clay, but the lack of agreement between the teams means this cannot be concluded with confidence.

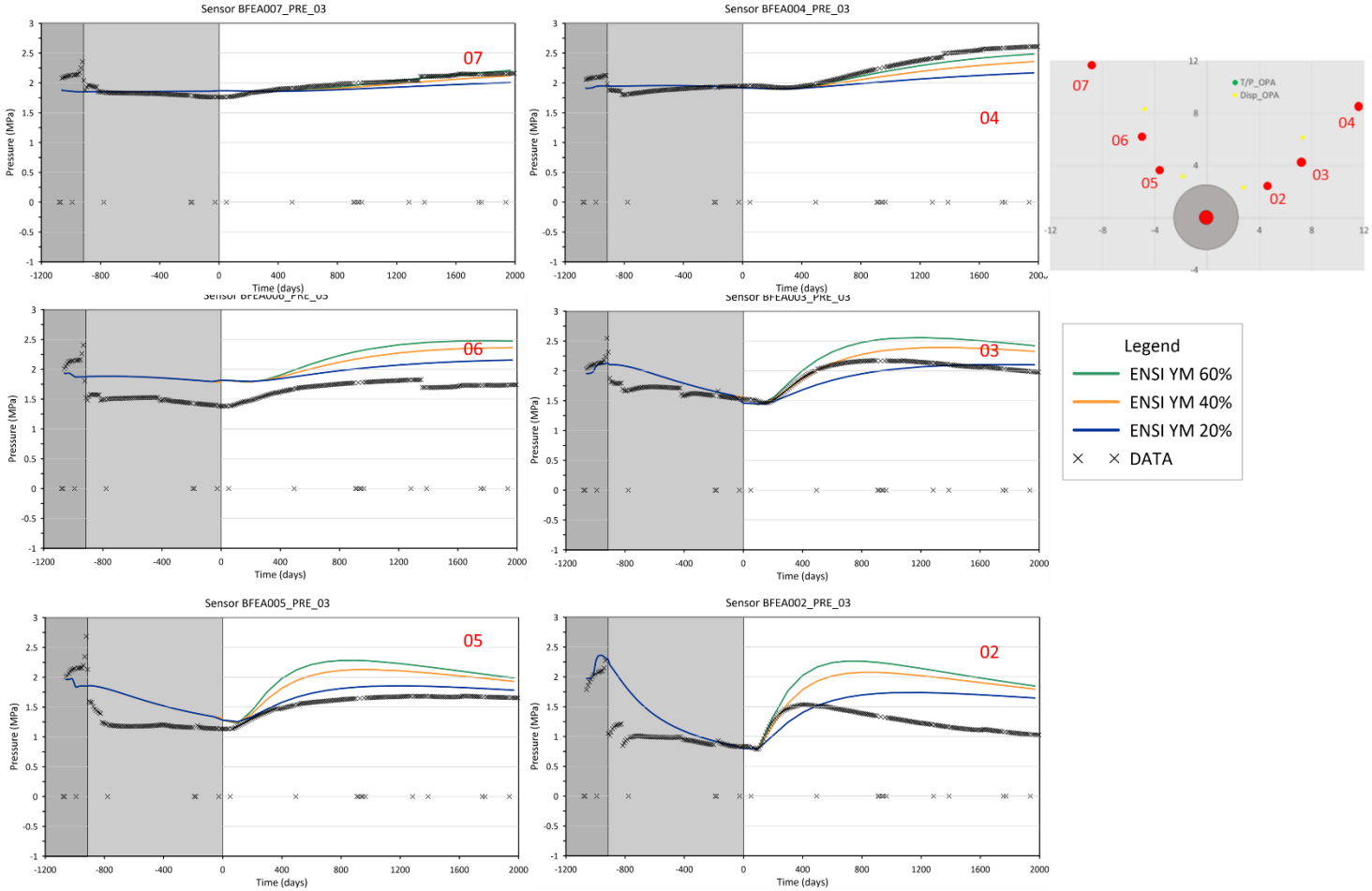

Figure 46: Change in pore pressure increase depending on selected Youngs Modulus (60%...green, 40%...orange, 20%...blue)

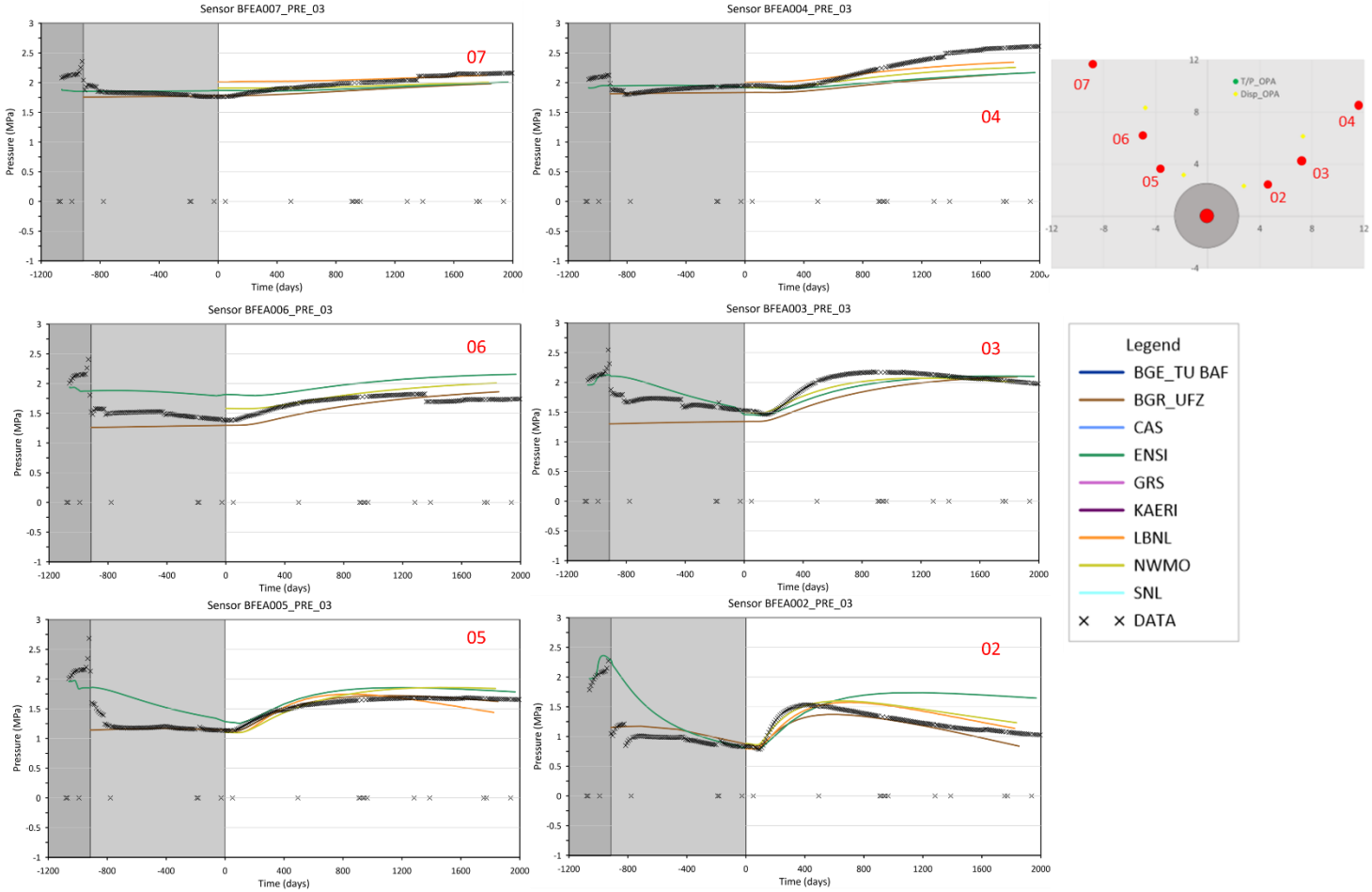

Figure 47: Change in pore water pressure for the teams with Youngs Modulus of 20 % (NWMO, LBNL, ENSI) and 25% (BGR/UFZ)

7 Step 3 – Extended heating prediction

7.1 Aim

The aim of Step 3 was to use the models developed in previous steps along with the parameterisation calibrated against the data, to predict how temperature and pressure in the Opalinus Clay will change through time beyond the available data, taking into account the actual and planned changes in heater power in the FE experiment.

7.2 Model specification

The model specifications previously described were still relevant to this step and the only additional data that teams were given was the schedule of power output for the heaters (Table 17, Figure 48). Teams were advised to use their preferred model from Step 1 or Step 2 as a basis for this longer-term prediction.

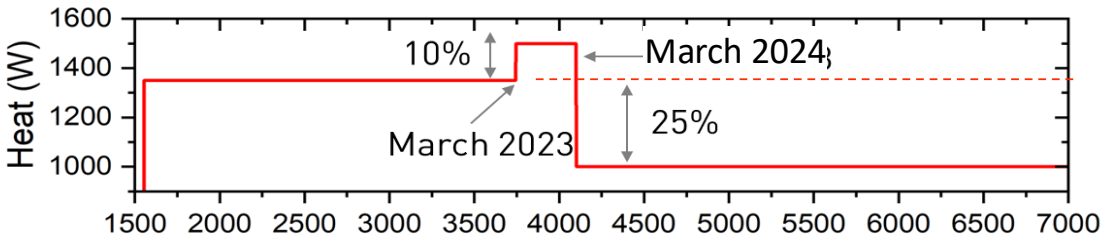

Figure 48: Modified schedule of heating for the FE experiment in days after start of heating.

Table 17: Scheduled power output for the heaters in the FE experiment.

	Date	Power (W)
Heater 1	15.12.2014 13.01.2015 16.02.2015	500 1000 1350
Heater 2	17.02.2015	1350
Heater 3	18.02.2015	1350
All Heaters	16.03.2023	1485
All Heaters	16.03.2024	1012.5

7.3 Modelling strategy

Six teams contributed results to Step 3, and the models that they were based on are shown in Table 18.

Table 18: Model on which Step 3 model is based.

Team	Starting model
BGR/UFZ	Step 2
BGE/TUBAF	Step 2
ENSI	Step 2
KAERI/KIGAM	Step 2 (model size-up 150 x 100 x 150)
LBNL	Step 2
NWMO	Step 2

7.4 Results

The modelled temperatures in Step 3 are all within 2°C of each other over the 6000-day time period modelled, and there is no evidence of the models diverging. The differences between the models arise within the first 2000 days and are then stable. This suggests that the differences are caused by the thermal conductivities. The two sensors closest to the tunnel (BFEA002_TEM_03 and BFEA005_TEM_03) show a short-term peak in temperature between 3000 and 4000 days related to the increase in heater power during 2023 and early 2024. Further into the Opalinus Clay the increase in heater power shows a smaller impact and the decrease in heater power in March 2024 is more evident as a flattening on the temperature graphs.

The modelled pressures in the Opalinus Clay in Step 3 are within 2 MPa of each other over the 6000-day time period, for the sensors closest to the heater. However, models do have different gradients of pressure evolution at the end of the model run and some teams overpredicted and some teams underpredicted the pressure evolution during the first 2000 years for which data were available. For the sensors further away from the heater, the pressure difference is less than 1 MPa, providing a better estimate of the pressure evolution over the next few years.

The predictions for the relative humidity mostly show a good agreement in trend over time. The discrepancy in the magnitude of relative humidity values between the team's predictions is up to 20% which is relatively high. Only one team predicted an increase of the relative humidity during the next 10 years.

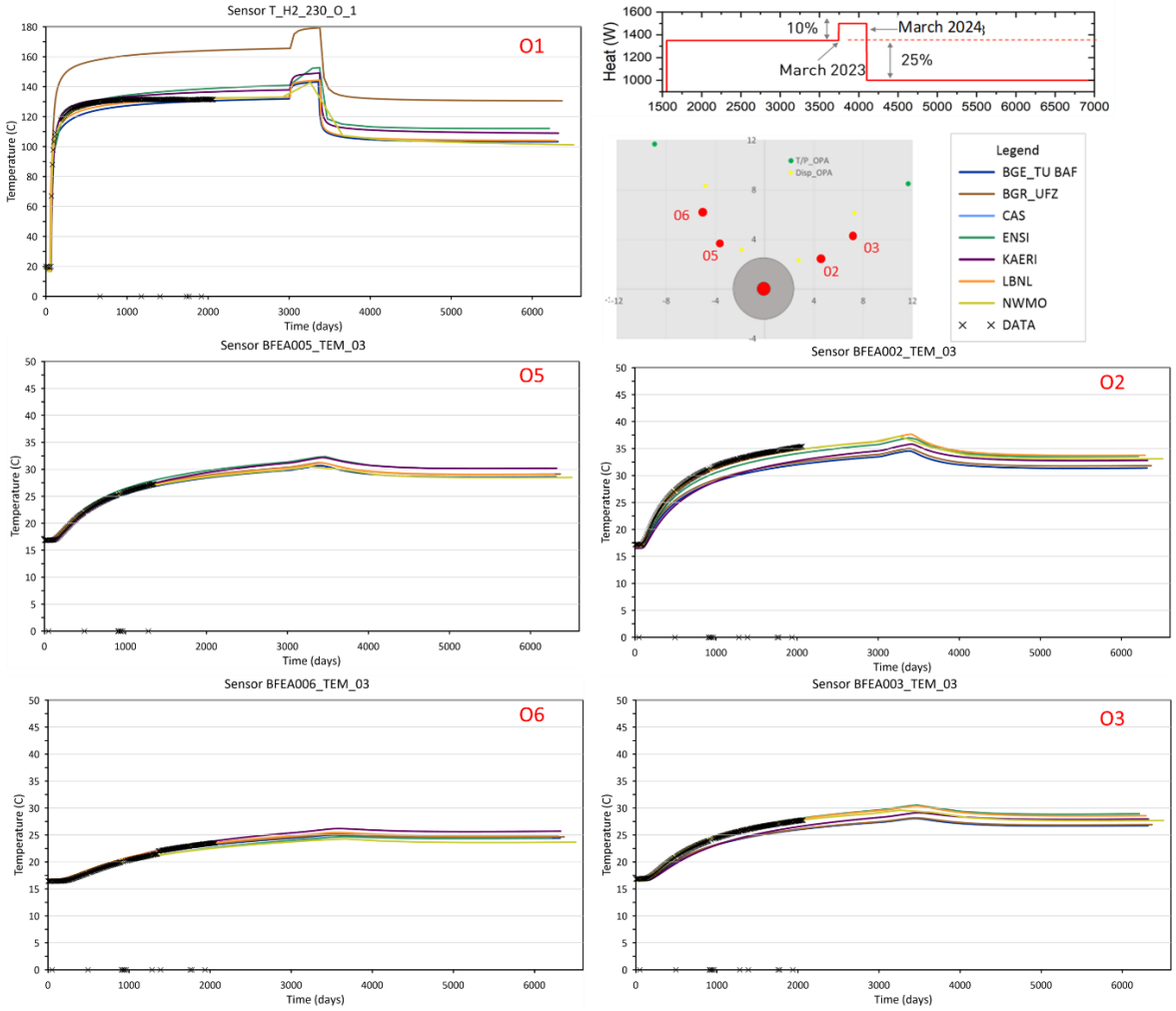

Figure 49: Selected temperature results for locations in the Opalinus Clay and on the heater from Step 3.

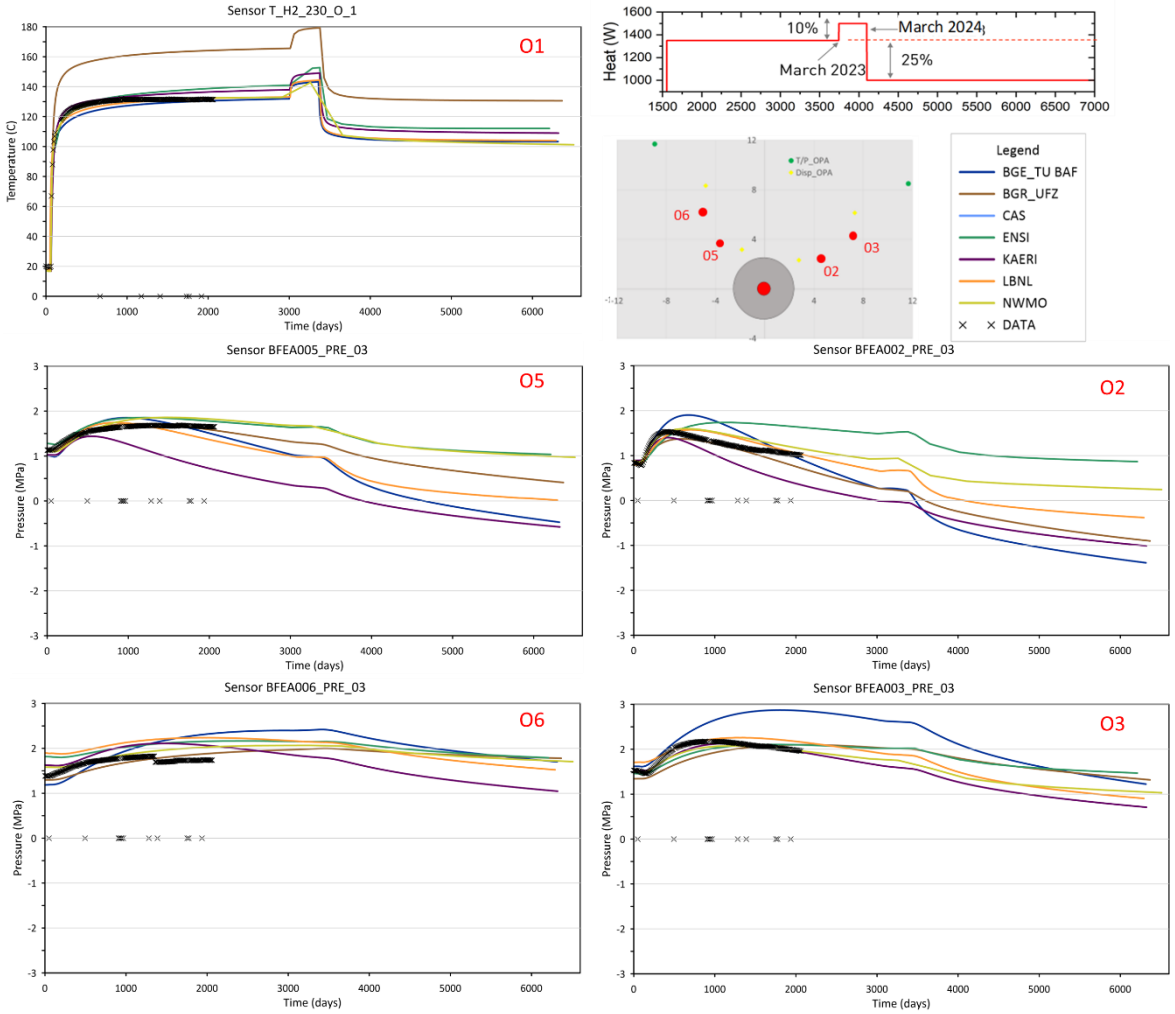

Figure 50: Selected Pressure results for locations in the Opalinus Clay from Step 3 and the temperature evolution at the heater (O1).

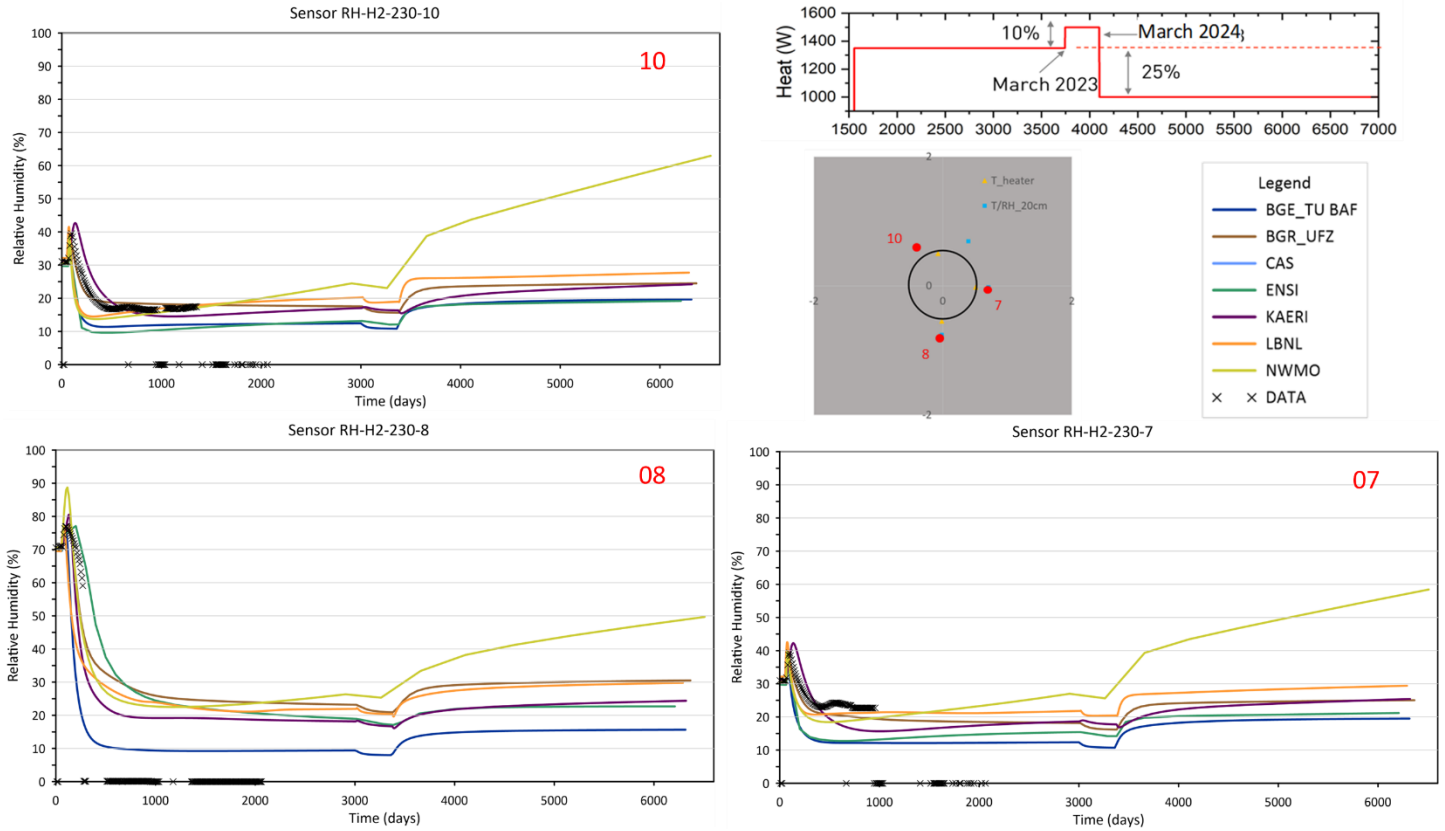

Figure 51: Selected relative humidity results for locations in the tunnel from Step 3.

7.5 Discussion

The predicted evolution of temperature agrees very closely between the teams and provides a small range of uncertainty for the expected future evolution. Compared to temperature, results for porewater pressure evolution by the teams show a larger range of possible development. The general behaviour is comparable between the teams but over- and underestimations of the pressure increase during initial heating and the drainage effect cause a larger uncertainty of about 2 MPa close to the heater. If we only used results for those sensors where the predictions of the models give a good reproduction of the measured peak porewater pressure and the decrease afterwards due to drainage, the range of pressure results could have been reduced to approximately 1 MPa. Further away from the heater, the range of pressure predictions is between 0.5 and 0.8 MPa. The relatively large range of results illustrates the value in using a multi-team approach for making predictions about the future evolution of repository systems. The difference in modelling approaches and calibration can be used to derive an envelope of performance and hence understand something about uncertainty in both the models and the disposal system itself.

The predictions for the relative humidity suggest with one exception that an increase in relative humidity due to the resaturation of bentonite from the Opalinus Clay is not expected by the models during the next 10 years. Though the discrepancy of up to 20 % between the team's predictions is relatively high, the processes within the tunnel were not the focus of the modelling work. These results suggest the process of resaturation to be a slow process. However, as said in previous chapters, the results need to be interpreted with care. The representation of bentonite was highly simplified in all models used here. Resaturation and relative humidity evolution are two quantities for which pore space alteration due to thermal, hydraulic and swelling pressure effects is likely to be significant, and increasingly so with the duration of the experiment.

8 Summary and Conclusions

Nine modelling teams have participated in Task C, developing models of the FE experiment of increasing complexity through a series of staged modelling steps.

In Step 0, teams participated in a series of benchmarking exercises with strictly defined specifications. These were designed to enable comparison between the different codes and model implementations, to ensure that the reasons for differences between team's results were understood before more complexity was introduced. Initially, although teams were able to produce consistent predictions of temperature and consistent predictions of trends in porewater pressure development in the Opalinus Clay, the predicted magnitudes of porewater pressure varied significantly between teams. The reasons for these differences were investigated and found to be caused primarily by different conceptual model assumptions (including temperature dependence of the thermal expansion of water), different model formulations (including porosity evolution) and differences in modelled domain sizes, boundary conditions and grid discretisation. This demonstrates that comparisons between multiple modelling teams and/or comparison with analytical results and experimental data are highly beneficial in providing an indication of uncertainty in model predictions. Once the modelling teams had agreed a consistent approach to the assumptions above, all teams were able to produce very consistent results for temperature and pressure evolution in the simplified benchmark cases.

In Step 1 of the task, teams produced 3D models of the FE experiment based on the models developed in Step 0 (with almost all teams producing coupled THM models). The model results were compared to sensor data from the FE experiment and teams could calibrate their model parameters to achieve a better fit to the data. These models were able to reproduce the correct range of behaviour for temperature and pressure evolution in the Opalinus Clay, but it was challenging to achieve a close match between all the teams and the data. This indicated that the fundamental physical processes leading to heating induced pore pressure change in the Opalinus Clay were correctly represented but there may be some additional features and/or processes, especially with regard to the hydraulic-mechanical behaviour during the excavation as well as simplified material models, that needed to be added to the models and improved to achieve a very close agreement. In particular, the comparison of porewater pressure evolution in Opalinus Clay showed larger discrepancies between measurements and models closer to the tunnel contour; the models either overpredicted the pressure

increase, or overpredicted the drainage effect. This could be due to deformations of the rock mass during excavation that were not correctly considered in the models, which may limit the temperature driven pressure increase and the drainage of Opalinus Clay.

In Step 2 of the task, the teams therefore investigated whether including additional processes or features in the models could explain the behaviour seen in the experimental data. This included representation of ventilation of the open FE tunnel prior to backfilling, stress change during excavation and development of an EDZ, and shotcrete lining the tunnel. Inclusion of ventilation and shotcrete improved teams' results, with better reproduction of the temperature driven pressure increase and the drainage of Opalinus Clay compared to measurements. However, teams generally overpredicted the drying effect of ventilation; this may be because the Opalinus Clay was disturbed already during excavation, or the variation in relative humidity across the tunnel may restrict water vapour loss from the tunnel walls. Relatively low values for the Young's modulus of Opalinus Clay helped to have a better agreement with the porewater pressure increase close to the heater, which may be indicative of inelastic effects. In general, the simplified models performed well in predicting the evolution of pore pressure (within ~1.5 MPa for most teams), but there remained a significant spread between teams which could indicate the range of uncertainty. This may indicate that further missing features and/or processes could be included to help the models represent the data better (e.g. better representation of the EDZ or bentonite buffer), though this would introduce further complexity. Inclusion of a simplified elastic representation of the EDZ by three modelling teams did not clearly improve pressure predictions.

In the final step of the task, teams used the calibrated models developed in previous steps to predict how temperature and pressure in the Opalinus Clay will change through time beyond the available data, taking into account the actual and planned changes in heater power in the FE experiment. The modelled temperatures were all within 2°C of each other over the 6000-day time period modelled. The modelled pressures in the Opalinus Clay were within 2 MPa, for sensors closest to the heater, with some divergence in pressure gradients shown and some discrepancies compared to the available data over the first 2000 years. For sensors further from the heater, the pressure difference is less than 1 MPa. This model comparison gives an indication of the modelling uncertainty expected in longer-term forecasts of pore pressure development.

Overall, the work conducted within the task, showed that the teams have a sufficient understanding of the relevant processes in the vicinity of the heater elements and based on that understanding teams were able to reproduce the measured data. Due to the detailed geometry and the necessary large size of the models the task was relatively

complex and time-consuming. Despite the experience of the teams benchmarking consumed a significant amount of the available time until it could be ensured that all teams covered the relevant processes correctly. Temperature, relative humidity and pore pressure were well reproduced by the teams although there remain uncertainties for the pore pressure. The models are able to reproduce the pressure evolution correctly further away from the heater whereas larger differences can be observed in the area closer to the heater. Probably the EDZ plays an important role on the THM behaviour of the rock in the near field, which is not fully understood yet. Similar observations were reported in the EURAD Hitec project. Implementing the missing processes in the models would help to improve the reproduction of the measured data and with that strengthen the predictive capabilities. Based on the current results, the prediction of the temperature is possible with a relative low degree of uncertainty whereas especially the prediction of pore pressure evolution remains challenging and is connected with a higher degree of uncertainty. Future code improvement might help to reduce the uncertainties. Furthermore, it could be helpful to assign the predictive modelling task to several teams. The spread between the teams could be used as indicator for the degree of uncertainty and ideally the real evolution of the measurements lies within the predicted range of team results.

9 Planned and Completed Publications

Table 19 gives the planned and completed publications under this task, correct at the time of writing.

Table 19: Planned and completed journal and conference papers for Task C. Entries in bold indicate RWM-funded authorship.

Author(s)	Title	Journal/ Conference	Status
Teklu Hadgu, Edward Matteo and Thomas Dewers	Model Development for Thermal-Hydrology Simulations of a Full-Scale Heater Experiment in Opalinus Clay	Nuclear Technology Journal	Published
Bastian Graupner, Kate Thatcher, Larissa Friedenberg, Ruiping Guo, Teklu Hadgu, Wenbo Hou, Sonja Kaiser, J Taehyun Kim, Thomas Nagel, Rebecca Newson, Peng-Zhi Pan, Michael Pitz, Jonny Rutqvist, Jan Thiedau	THM modelling of the FE-experiment	GETE	In preparation
Taehyun Kim, Chan-Hee Park, Changsoo Lee, Jin-Seop Kim, Eui-Seob Park and Bastian Graupner	A numerical analysis of thermo-hydro-mechanical behaviour in the FE experiment at Mont Terri URL: Investigating capillary effects in bentonite on the disposal system	GETE	Submitted, 25 March
Pitz, M., Kaiser, S., Grunwald, N., Kumar, V., Buchwald, J., Wang, W., Naumov, D., Chaudhry, A. A., Maßmann, J., Thiedau, J., Kolditz, O., & Nagel, T	Non-isothermal consolidation: A systematic evaluation of two implementations based on multiphase and Richards equations.	*International Journal of Rock Mechanics and Mining Sciences (2023)*	Published
Buchwald, J., Kolditz, O., & Nagel, T.	Design-of-Experiment (DoE) based history matching for probabilistic integrity analysis—A case study of the FE-experiment at Mont Terri	*Reliability Engineering & System Safety (2023)*	Published

Pitz, M., Grunwald, N., Graupner, B., Kurgyis, K., Radeisen, E., Maßmann, J., Ziefle, G., Thiedau, J., & Nagel, T.	Benchmarking a new TH2M implementation in OGS-6 with regard to processes relevant for nuclear waste disposal.	Environmental Earch Sciences (2023)	Published
Buchwald, J., Kaiser, S., Kolditz, O., & Nagel, T.	Improved predictions of thermal fluid pressurization in hydro-thermal models based on consistent incorporation of thermo-mechanical effects in anisotropic porous media.	International Journal of Heat and Mass Transfer (2021)	Published
Kaiser, S., Wang, W., Buchwald, J., Naumov, D., Chaudhry, A.A., Nagel, T.	Effects of increasing complexity: Coupled THM modelling of the FE Experiment at Mt. Terri	TBD	In preparation
Guo, R., and Briggs, S.	Thermo-hydro-mechanical calibration modelling of the FE-Experiment and sensitivity analyses	International Journal of Rock Mechanics and Mining Sciences	Submitted, Jan. 2024
Guo, R.	Influence of porosity variation on thermally-induced pore pressure in coupled thermo-hydro-mechanical modelling	TBD	In preparation.

10 Acknowledgements

DECOVALEX is an international research project comprising participants from industry, government and academia, focusing on development of understanding, models and codes in complex coupled problems in sub-surface geological and engineering applications; DECOVALEX-2023 is the current phase of the project. The authors appreciate and thank the DECOVALEX-2023 Funding Organisations Andra, BASE, BGE, BGR, CAS, CNSC, COVRA, US DOE, ENRESA, ENSI, JAEA, KAERI, NWMO, RWM, SÚRAO, SSM and Taipower for their financial and technical support of the work described in this report. The statements made in the report are, however, solely those of the authors and do not necessarily reflect those of the Funding Organisations.

11 References

Bilke L., Flemisch B., Kalbacher T., Kolditz O., Helmig R. and Nagel, T., 2019. Development of Open-Source Porous Media Simulators: Principles and Experiences. Transport in Porous Media, 130(1) (2019), 337–361. https://doi.org/10.1007/s11242-019-01310-1

Bock H., 2009. RA Experiment: Updated Review of the Rock Mechanics Properties of the Opalinus Clay of the Mont Terri URL based on Laboratory and Field Testing Technical Report 2008-04, November 2009, Mont Terri Project, St-Ursanne.

Bond A., Millard A., Nakama S., Zhang C. and Garritte B., 2013. Approaches for representing hydro-mechanical coupling between sub-surface excavations and argillaceous porous media at the ventilation experiment, Mont Terri. Journal of Rock Mechanics and Geotechnical Engineering 2013, 5(2). https://doi.org/10.1016/j.jrmge.2013.02.002

Bossart P. (2015): Characteristics of the Opalinus Clay at Mont Terri, Manuscript.

Buchwald J., Kaiser S., Kolditz O., & Nagel T., 2021. Improved predictions of thermal fluid pressurization in hydro-thermal models based on consistent incorporation of thermo-mechanical effects in anisotropic porous media. International Journal of Heat and Mass Transfer, 172, 121127. https://doi.org/10.1016/j.ijheatmasstransfer.2021.121127

Buchwald, J., Kolditz, O., & Nagel, T., 2024. Design-of-Experiment (DoE) based history matching for probabilistic integrity analysis—A case study of the FE-experiment at Mont Terri. Reliability Engineering & System Safety, 244(August 2023), 109903. https://doi.org/10.1016/j.ress.2023.109903

COMSOL Multiphysics® v. 5.3, 2017. www.comsol.com. COMSOL AB, Stockholm, Sweden.

COMSOL Multiphysics® v. 5.6, 2020. www.comsol.com. COMSOL AB, Stockholm, Sweden.

Edlefsen N. E. and Anderson A. B. C., 1943. Thermodynamics of soil moisture. Hilgardia, 15, 31-299.

Elyasi A., Goshtasbi K., Hashemolhosseini H. and Barati S., 2016. Coupled solid and fluid mechanics simulation for estimating optimum injection pressure during reservoir co 2-eor. Structural Engineering and Mechanics, 59(1), 37-57. https://doi.org/10.12989/sem.2016.59.1.037

ENSI, 2014. Kompilation der lithologischen Variabilität und Eigenschaften des Opalinus-Ton im Felslabor Mont Terri, swisstopo, Expertenbericht zuhanden des ENSI, Wabern, 2014, ENSI 33/489.

Feng X.-T., Pan P.-Z., Wang Z. and Zhang Y., 2021. Development of Cellular Automata Software for Engineering Rockmass Fracturing Processes. Challenges and Innovations in Geomechanics 125 (2021) 62:74. http://dx.doi.org/10.1007/978-3-030-64514-4_4

Garitte B., Shao H., Wang X. R., Nguyen T. S., Rutqvist J., Birkholzer J., Wang W. Q., Kolditz O., Pan P. Z., Feng X. T., Graupner B. J., Maekawa K., Manepally C., Dasgupta B., Stothoff S., Ofoegbu G., Fedors R. and Barnichon J. D., 2017. Evaluation of the predictive capability of coupled 106odelli-hydro-mechanical models for a heated bentonite/clay system (HE-E) in the Mont Terri Rock Laboratory. Environ Earth Sci 76, 64 (2017). https://doi.org/10.1007/s12665-016-6367-x

Graupner B. J., Shao H., Nguyen T. S., Li Z., Rutqvist J., Chen F., Birkholzer J., Wang W., Kolditz O., Pan P. Z., Feng X. T., Lee C., Maekawa K., Stothoff S., Manepally C., Dasgupta B., Ofoegbu G., Fedors R., Barnichon J. D., Ballarini E., Bauer S. and Garitte B., 2018. Comparative modelling of the coupled thermal-hydraulic-mechanical (THM) processes in a heated bentonite pellet column with hydration. Environmental Earth Sciences (2018) 77:84.

Grunwald N., Maßmann J., Naumov D., Kolditz O. and Nagel T., 2022. Non-isothermal two-phase flow in deformable porous media: Systematic open-source implementation and verification procedure. Geomech. Geophys. Geo-energ. Geo-resour. 8, 107 (2022). https://doi.org/10.1007/s40948-022-00394-2

Guo R., 2023. Calculation of thermal-hydraulic-mechanical response of a deep geological repository for radioactive used fuel in granite. International Journal of Rock Mechanics and Mining Sciences 170 (2023) 105435. https://doi.org/10.1016/j.ijrmms.2023.105435.

Guo R. and Briggs Scott., 2024. Thermo-hydro-mechanical calibration modelling of the FE-Experiment and sensitivity analyses. Planned to be submitted to IJRMMS.

Hammond G. E., Lichtner P. C. and Mills R. T., 2014. Evaluating the Performance of Parallel Subsurface Simulators: An Illustrative Example with PFLOTRAN. J. Water Resources Research. 50, doi:10.1002/2012WR013483.

IF97 (International Formulating Committee), 2017. International Association for the Properties of Water and Steam Revised Release on the IAPWS Industrial

Formulation 1997 for the Thermodynamic Properties of Water and Steam, Lucerne, Switzerland August 2007.

Itasca Consulting :Group, 2017. FLAC3D V6.0, Fast Lagrangian Analysis of Continua in 3 Dimensions, User's Guide Minneapolis.

Jung Y., Pau G.S.H., Finsterle S., Pollyea R.M., 2017. TOUGH3: A new efficient version of the TOUGH suite of multiphase flow and transport simulators. Comput. Geosci. 108, 2–7 (2017). https://doi. org/10.1016/j.cageo.2016.09.00919.

Kim T., Park C.-H., Watanabe N., Park E.-S., Park J.-W., Jung Y.-B. and Kolditz O., 2021. Numerical modelling of two-phase flow in deformable porous media: application to CO2 injection analysis in the Otway basin, Australia. Environmental Earth Sciences 80(3):1–15.

Kolditz O., Gorke U.-J., Shao H., Shao H. and Nagel T., 2019. Workflows in Environmental Geotechnics: Status-Quo and Perspectives (2019), pp. 119–127. https://doi.org/10.1007/978-981-13-2221-1_6

Lanyon B., Firat Lüthi B. and Manukyan E., 2020. Interpretation of the First 5 Years of the FE Experiment: a THM Synthesis. Nagra Arbeitsbericht NAB 19-46.

Lehmann, C., Bilke, L., Buchwald, J., Graebling, N., Grunwald, N., Heinze, J., Meisel, T., Lu, R., Naumov, D., Rink, K., Özgür Sen, O., Selzer, P., Shao, H., Wang, W., Zill, F., Nagel, T., & Kolditz, O., 2024. OpenWorkFlow—Development of an open-source synthesis-platform for safety investigations in the site selection process. Grundwasser. https://doi.org/10.1007/s00767-024-00566-9

Firat Lüthi B., 2018. Full-Scale Emplacement (FE) Experiment – Data Trend Report. Data from excavation and during 3 first years of heating 01.01.2012 – 31.08.2018. Nagra Arbeitsbericht NAB 18-39.

Firat Lüthi B. and Mussina Z., 2020. FE Experiment: Data Trend Report. Data from excavation and during 5 first years of heating (01.01.2012 – 31.08.2020). Nagra Arbeitsbericht NAB 20-42.

Mei W., Li M., Pan P.-Z., Pan J. and Liu K., 2021. Blasting induced dynamic response analysis in a rock tunnel based on combined inversion of Laplace transform with elasto-plastic cellular automaton. Geophysical Journal International 225 (2021), 699-710.

Müller, H.R., Garitte, B. Vogt, T., Köhler, S., Sakaki, T., Weber, H., Spillmann, T., Hertrich, M., Becker, J. K., Giroud, N., Cloet, V., Diomidis, N. & Vietor, T., 2017.

Implementation of the full-scale emplacement (FE) experiment at the Mont Terri rock laboratory, Swiss Journal of Geoscience, DOI 10.1007/s00015-016-0251-2.

Nagra, 2019. Implementation of the Full-scale Emplacement Experiment at Mont Terri: Design, Construction and Preliminary Results. Nagra Technical Report 15-02.

Olivella S., Vaunat J. and Rodriguez-Dono A., 2021. CODE_BRIGHT User's Guide 2021. Universitat Politècnica de Catalunya (UPC), Department of Civil and Environmental Engineering. https://deca.upc.edu/en/projects/code_bright.

Pan P.-Z., Feng X.-T. and Hudson J. A., 2009. Study of failure and scale effects in rocks under uniaxial compression using 3d cellular automata. International Journal of Rock Mechanics and Mining Sciences 46, 4 (2009), 674–685.

Pan P.-Z., Yan F. and Feng X.-T., 2012a. Modeling the cracking process of rocks from continuity to discontinuity using a cellular automaton. Computers & Geosciences 42 (2012), 87–99.

Pan P., Feng X. and Zhou H., 2012b. Development and applications of the elasto-plastic cellular automaton. Acta Mechanica Solida Sinica 25, 2 (2012), 126–143.

Pan P.-Z., Rutqvist J., Feng X.-T. and Yan F., 2013. Modeling of caprock discontinuous fracturing during co2 injection into a deep brine aquifer. International Journal of Greenhouse Gas Control 19 (2013), 559–575.

Pan P.-Z., Feng X.-T., Zheng H. and Bond, A., 2016. An approach for simulating the THMC process in single novaculite fracture using EPCA. Environmental Earth Sciences 75, 15 (2016), 1–16.

Pan P.-Z., Yan F., Feng X.-T. and Wu Z.-H., 2017. Study on coupled thermo-hydro-mechanical processes in column bentonite test. Environmental Earth Sciences (2017), 76(17), 618.

Park C.-H., Kim T., Park E.-S., Jung Y.-B. and Bang E.-S., 2019. Development and verification of OGSFLAC simulator for hydromechanical coupled analysis: Single-phase fluid flow analysis. Tunnel and Underground Space 29(6) (2019), 468–479.

Philip J. R. and de Vries D. A., 1957. Moisture movement in porous materials under temperature gradients. EOS Transactions, AGU, 38, 222-232.

Pitz M., Kaiser S., Grunwald N., Kumar V., Buchwald J., Wang W., Naumov D., Chaudhry A. A., Maßmann J., Thiedau J., Kolditz O. and Nagel T., 2023. Non-isothermal consolidation: A systematic evaluation of two implementations based on multiphase and Richards equations. International Journal of Rock Mechanics and Mining Sciences, 170, 1365-1609, https://doi.org/10.1016/j.ijrmms.2023.105534.

Plua C., Vitel M., Seyedi D. M. and Armand G., 2020. DECOVALEX-2019: Task E Final Report.

Pruess K., Oldenburg C. and Moridis G., 2012. TOUGH2 User's Guide, Version 2. LBNL-43134.

Rinaldi A.P., Rutqvist J., Luu K., Blanco-Martín L., Hu M., Sentís M.L., Eberle L., and Kaestli P., 2022. TOUGH3-FLAC3D: a modeling approach for parallel computing of fluid flow and geomechanics. Computational Geosciences. 26, 1563–1580. https://doi.org/10.1007/s10596-022-10176-0.

Rutqvist J., 2011. Status of the TOUGH-FLAC simulator and recent applications related to coupled fluid flow and crustal deformations. Computer & Geosciences, Volume 37, Issue 6 (June 2011), pp. 739-750.

Rutqvist J., 2017. An overview of TOUGH-based geomechanics models. Computers & Geosciences, 108, 56–63 (2017). https://doi.org/10.1016/j.cageo.2016.09.007.

Rutqvist J., Wu Y.-S., Tsang C.-F. and Bodvarsson G. A., 2002. Modeling approach for analysis of coupled multiphase fluid flow, heat transfer, and deformation in fractured porous rock. International Journal of Rock Mechanics and Mining Sciences, 39, 429-442. https://doi.org/10.1016/S1365-1609(02)00022-9.

Rutqvist J., Graupner B., Guglielmi Y., Kim T., Maßmann J., Nguyen T. S., Park J. W., Shiu W., Urpi L., Yoon J. S., Ziefle G. and Birkholzer J., 2020. An international model comparison study of controlled fault activation experiments in argillaceous claystone at the Mont Terri Laboratory. International Journal of Rock Mechanics and Mining Sciences 136(4):104505.

Rutqvist J., Noorishad J. and Tsang C.-F., 1999. Coupled thermohydromechanical analysis of a heater test in unsaturated clay and fractured rock at Kamaishi Mine. LBNL report 44203.

Settari A. and Mourits F. M., 1998. A coupled reservoir and geomechanical simulation system. Society of Petroleum Engineers (SPE) Journal 27(9), 219-226, SPE paper 50939.

Sharqawy M. H., Lienhard J. H. and Zubair S. M., 2010. Thermophysical properties of seawater: A review of existing correlations and data. Desalination and Water Treatment, 16:354-380.

Simandoux O., Prost A., Gateau J., Bossy E., 2015. Influence of nanoscale temperature rises on photoacoustic generation: Discrimination between optical absorbers based on thermal nonlinearity at high frequency, Photoacoustics, 3:1, pp 20-25,

https://doi.org/10.1016/j.pacs.2014.12.002.Somerton W.H., El-Shaarani A. H. and Mobarak S. M., 1974. High temperature behavior of rocks associated with geothermal-type reservoirs. Paper SPE-4897. Proceedings of the 44th Annual California Regional Meeting of the Society of Petroleum Engineers. Richardson, TX: Society of Petroleum Engineers.

Vargaftik N. B., 1975. Tables on the Thermophysical Properties of Liquids and Gases, 2nd Ed., John Wiley & Sons, New York, NY, 1975.

Walker W. R., Sabey J. D., and Hampton D. R., 1981. Studies of Heat Transfer and Water Migration in Soils, Final Report, Department of Agricultural and Chemical Engineering, Colorado State, University, Fort Collins, CO, 80523, April 1981.

Willmott, C.J., S.M. Robeson and K. Matsuura (2011). A refined index of model performance. International Journal of Climatology 32.13, pp. 2088–2094. https://doi.org/10.1002/joc.2419

Winhausen L., Khaledi K., Jalali M., Urai J.L. and Amann F, 2022. Failure mode transition in Opalinus Clay: a hydro-mechanical and microstructural perspective, Solid Earth, 13, 901–915, https://doi.org/10.5194/se-13-901-2022

Appendix A: Porosity Evolution in TH and THM Simulations

For the THM simulations in cases 0c2, 0c3 and 0c, some teams decided to represent THM behaviour by TH simulations with the pore compressibility coefficient. Hence, some differences can be expected resulting from how the pore space evolution is reflected in fully coupled THM simulations and TH simulations with a storage coefficient. In the following text, the evolution of pore space for both of these cases is briefly derived and the implications for simulation results are discussed using simulation results obtained with different boundary conditions and domain sizes:

In the fully saturated case c3, the general water mass balance equation can be expressed by[1]:

$$\frac{\partial}{\partial t}(\phi\rho_{\mathrm{LR}}) + \phi_0\rho_{\mathrm{LR}}\mathrm{div}\frac{\partial \mathbf{u}}{\partial t} + \rho_{\mathrm{LR}}\mathrm{div}\mathbf{q}_{\mathrm{w}} = 0 \qquad (1)$$

Where ϕ is the porosity, ρ_{LR} is the pore water density, $\mathbf{q}_{\mathrm{w}}$ is the Darcy flow and **u** represents the solid displacement vector. The chain rule can be applied to expand the first term:

$$\underbrace{\rho_{\mathrm{LR}}\frac{\partial}{\partial t}(\phi)}_{\text{porosity change}} + \phi_0\frac{\partial}{\partial t}(\rho_{\mathrm{LR}}) + \underbrace{\phi_0\rho_{\mathrm{LR}}\mathrm{div}\frac{\partial \mathbf{u}}{\partial t}}_{\text{control volume change}} + \rho_{\mathrm{LR}}\mathrm{div}\mathbf{q}_{\mathrm{w}} = 0 \qquad (2)$$

The reference porosity or Lagrangian pore space evolves therefore with the change of porosity $\frac{\partial}{\partial t}(\phi)$ on one hand as well as with the expansion of the medium or the control volume given by $\phi_0\mathrm{div}\frac{\partial \mathbf{u}}{\partial t}$ on the other hand. Thus, we can introduce a new variable Φ, which denotes the reference or Lagrangian pore space, and its change is described by:

$$\frac{\partial \Phi_{\mathrm{THM}}}{\partial t} = \frac{\partial}{\partial t}(\phi) + \phi_0\mathrm{div}\frac{\partial \mathbf{u}}{\partial t} \qquad (3)$$

According to Grunwald *et al*. (submitted), the change of porosity for the THM-case is given by:

$$\frac{\partial}{\partial t}\phi = (\alpha_{\mathrm{B}} - \phi_0)\left(\mathrm{div}\frac{\partial \mathbf{u}}{\partial t} - \beta_{T,\mathrm{SR}}\frac{\partial T}{\partial t} + \beta_{p,\mathrm{SR}}\frac{\partial p_{\mathrm{LR}}}{\partial t}\right) \qquad (4)$$

[1] With the assumption of small deformations, a linearization around the initial state is used.

where α_{B} is the Biot coefficient, $\beta_{T,\mathrm{SR}}$ represents the volumetric solid thermal expansion coefficient, $\beta_{p,\mathrm{SR}}$ represents the solid compressibility and T and p_{LR} are temperature and pore water pressure. (4) can be inserted into (3), yielding:

$$\begin{aligned}\frac{\partial \Phi_{\mathrm{THM}}}{\partial t} &= (\alpha_{\mathrm{B}} - \phi_0)\left(\mathrm{div}\frac{\partial \mathbf{u}}{\partial t} - \beta_{T,\mathrm{SR}}\frac{\partial T}{\partial t} + \beta_{p,\mathrm{SR}}\frac{\partial p_{\mathrm{LR}}}{\partial t}\right) + \phi_0 \mathrm{div}\frac{\partial \mathbf{u}}{\partial t} \\ &= \alpha_{\mathrm{B}}\mathrm{div}\frac{\partial \mathbf{u}}{\partial t} + (\alpha_{\mathrm{B}} - \phi_0)\left(-\beta_{T,\mathrm{SR}}\frac{\partial T}{\partial t} + \beta_{p,\mathrm{SR}}\frac{\partial p_{\mathrm{LR}}}{\partial t}\right) \end{aligned} \quad (5)$$

For the following equation, we express the medium deformation by $\mathrm{div}\frac{\partial \mathbf{u}}{\partial t} = \frac{\partial}{\partial t}\varepsilon_{\mathrm{vol}}$ with $\varepsilon_{\mathrm{vol}}$ as the volumetric strain. In this comparison, we interpret the change of pore space available to pore water with respect to its initial state $\Delta\Phi = \Phi - \Phi_0$ (integration over elapsed time interval) so we get:

$$\Delta\Phi_{\mathrm{THM}} = \alpha_{\mathrm{B}}\boldsymbol{\varepsilon}_{\mathrm{vol}} + (\alpha_{\mathrm{B}} - \phi_0)\left(-\beta_{T,\mathrm{SR}}\Delta T + \beta_{p,\mathrm{SR}}\Delta p_{\mathrm{LR}}\right) \quad (6)$$

where the change of a temperature and pore pressure is also interpreted with respect to its initial state. With a Biot coefficient of $\alpha_{\mathrm{B}} = 1$, it is implicit that solid grains are incompressible and $\beta_{p,\mathrm{SR}} = 0$. Thus, eq. (6) becomes

$$\Delta\Phi_{\mathrm{THM}} = \alpha_{\mathrm{B}}\boldsymbol{\varepsilon}_{\mathrm{vol}} + (\alpha_{\mathrm{B}} - \phi_0)\beta_{T,\mathrm{SR}}\Delta T \quad (7)$$

In the TH case, we do not consider the deformation process and $\mathrm{div}\frac{\partial \mathbf{u}}{\partial t} = 0$ throughout the simulation. Instead, a pore compressibility coefficient c_{pore} was proposed as a proxy for the pore space evolution which is incorporated in eq. (10). Furthermore, it was proposed to neglect any thermal effects on pore space (Rutqvist *et al*. 2014). This argument follows Gens *et al*. (2007) where it is assumed that the pore space reduction due to thermal expansion of solid grains and pore space increase due to thermal expansion of the porous medium cancel each other out. The pore space in the TH case is thus given by:

$$\phi = \phi_0\left(1 + c_{\mathrm{pore}}(p_{\mathrm{LR}} - p_{\mathrm{LR0}})\right) \quad (8)$$

With its time derivative:

$$\frac{\partial}{\partial t}\phi = \phi_0 c_{\mathrm{pore}}\frac{\partial p_{\mathrm{LR}}}{\partial t} \quad (9)$$

where c_{pore} represents the pore compressibility. By inserting (9) into (2) and by considering that $\mathrm{div}\frac{\partial \mathbf{u}}{\partial t} = 0$ for the TH simulation, we get for the water mass balance equation:

$$\rho_{\mathrm{LR}}\phi_0 c_{\mathrm{pore}}\frac{\partial p_{\mathrm{LR}}}{\partial t} + \phi_0\frac{\partial}{\partial t}(\rho_{\mathrm{LR}}) + \rho_{\mathrm{LR}}\mathrm{div}\mathbf{q}_{\mathrm{w}} = 0 \quad (10)$$

where the change of pore space is equal to the change of porosity given by (9). It is a function only of pore water pressure and the integration over elapsed time interval leads to the following expression for the evolution of pore space available to pore water:

$$\Delta\Phi_{\mathrm{TH}} = \phi_0 c_{\mathrm{pore}} \Delta p_{\mathrm{LR}} \tag{11}$$

Since the mechanical response of the medium to pore water pressure and temperature changes in (1) is given by the term $\mathrm{div}\,(\partial\mathbf{u}/\partial t)$, an influence of the mechanical boundary conditions is expected. On small and confined domains, the value of this term will be smaller than on large, unconfined domains.

The plots in Figure 52 and Figure 53 compare evolution of the pore space available to pore water obtained by the models as defined in (7) and (11). In Figure 52, the pore space evolution of different models is compared at points O1 (near field, solid lines) and O3 (far field, dotted lines). When looking at the solid lines, it can be stated that in the end of the simulation, the smallest increase in pore space was computed by the 50x50m confined model. The 100x100m and 200x200m confined models resulted in larger pore space increases. The 50x50m unconfined model resulted in the largest increase of pore space of the THM models since the medium could expand freely.

The TH model with pore compressibility coefficient resulted in even higher pore space increase and is the only model where pore space increased monotonously throughout the entire simulation. All THM models predicted that at some point, the pore space begins to decrease again after the initial increase. Also, all THM models predicted a faster increase of pore space in the beginning of the simulation when compared to the TH model.

Another difference is that in the far field (red, dotted line) in THM, an initial decrease of pore space was observed. This was probably due to the compression of the medium in the far field as a response to the expansion of the medium in the near field. This effect became smaller for larger domains or with free outer boundaries. Looking at the pore pressure evolutions at the same points (Figure 52, right plot), it is evident that the pore pressures predicted by the TH model and THM model with free outer boundaries agreed very well. However, this was only true for the comparison with the unconfined THM model. All confined THM models predicted higher pore water pressures than the TH simulation.

Another difference between the THM and TH simulations is that all points (with the exception of point O3 in the 50x50 confined model) seemed to undergo an initial drop in pore pressure before the onset of the thermal pressurization of the water. This was due to the mechanical response of the medium, which propagated through the medium instantaneously and which translated the expansion of the medium through shearing.

It should be noted that different boundary conditions and assumptions regarding the mechanical behaviour can be cast into different parameterizations of TH models consistent with THM analyses under said boundary conditions (Buchwald *et al*. 2021). However, certain effects such as the pressure drop described in the last paragraph will only remain accessible in fully coupled simulations.

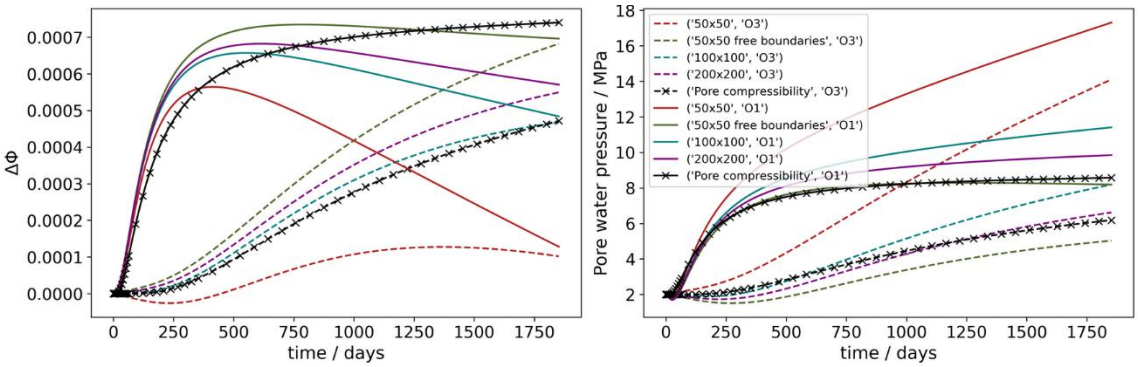

Figure 52: Pore space and pore water pressure temporal evolutions in the bedding direction in the near field (point O1, solid lines) and far field (point O3, dotted lines).

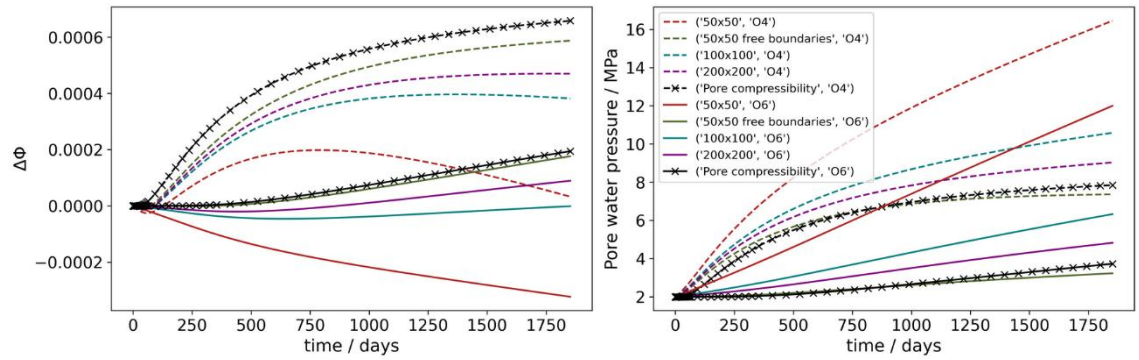

Figure 53: Pore space and pore water pressure temporal evolutions perpendicular to the bedding direction in the near field (point O4, solid lines) and far field (point O6, dotted lines).

A.1 References

Buchwald J., Kaiser S., Kolditz O. and Nagel T., 2021. Improved predictions of thermal fluid pressurization in hydro-thermal models based on consistent incorporation of thermo-mechanical effects in anisotropic porous media. International Journal of

Heat and Mass Transfer, 172, 121127. https://doi.org/10.1016/j.ijheatmasstransfer.2021.121127

Gens A., Garitte B. and Wileveau Y., 2007. In situ behaviour of a stiff layered clay subject to thermal loading: observations and interpretation. Geotechnique 57:207–228

Grunwald N., Maßmann J., Naumov D., Kolditz O. and Nagel T., 2022. Non-isothermal two-phase flow in deformable porous media: Systematic open-source implementation and verification procedure. Geomech. Geophys. Geo-energ. Geo-resour. 8, 107 (2022). https://doi.org/10.1007/s40948-022-00394-2

Rutqvist J., Zheng L., Chen F., Liu H. and Birkholzer J., 2014. Modeling of Coupled Thermo-Hydro-Mechanical Processes with Links to Geochemistry Associated with Bentonite-Backfilled Repository Tunnels in Clay Formations. Rock Mech Rock Eng (2014) 47:167–186 DOI 10.1007/s00603-013-0375-

Appendix B: Step 1c Team Parameters

Table 20: Team parameters for Opalinus Clay in Step 1c

Input parameters		Symbol	Unit	OPA [1]	BGE/TU BAF	BGR/UFZ	CAS	ENSI	GRS	KAERI	LBNL	NWMO	SNL
Thermal parameters	Dry thermal conductivity parallel and perpendicular to bedding	$\lambda_{dry,\parallel}$	*W/mK*	2.4	2.4	2.4	1.71	2.4	2.15	2.15	2.4	2.45	1.8
		$\lambda_{dry,\perp}$	*W/mK*	1.3	1.3	1.3	1.3	1.3	1.3	1.3	1.3	0.94	1.29
	Saturated thermal conductivity parallel and perpendicular to bedding	$\lambda_{sat,\parallel}$	*W/mK*	2.4	2.4	2.4	1.71	2.4	2.15	2.15	2.4	2.45	1.8
		$\lambda_{sat,\perp}$	*W/mK*	1.3	1.3	1.3	1.3	1.3	1.3	1.3	1.3	0.94	1.29
	Solid specific heat capacity	c_s	J/kgK	995	995	995	995	995	995	995	995	995	995
Hydraulic parameters	Dry Bulk Density	ρ_{bulk}	*kg/m³*	2340	2340	2340	2340	2340	2340	2340	2340	2340	2340
	Porosity	ϕ	-	0.13	0.17	0.13	0.13	0.13	0.13	0.13	0.13	0.13	0.13
	Intrinsic permeability	$k_{i,\parallel}$	*m²*	1.6E-20	6.25E-21	1.0E-20	4.0E-20	1.6E-20	1.0E-19	4.0E-20	2.0E-20	4.0E-20	1.5E-20
		$k_{i,\perp}$		1.0E-20	3.75E-21	5.0E-21	1.5E-20	1.0E-20	5.0E-20	3.0E-20	1.0E-20	1.2E-20	3.0E-21
	van Genuchten Entry Pressure	p_e	*MPa*	20.0	20.0	20.0	20.0	20.0	12.0		20.0	20.0	20.0
	van Genuchten n	n	-	2.5	2.5	2.5	2.5	2.5	1.4		2.5	2.5	2.5
	van Genuchten maximum water saturation	s_{max}	-	1.0	1.0	1.0	1.0	1.0	1.0		1.0	1.0	1.0
	van Genuchten residual water saturation	s_r	-	0.0	0.0	0.0	0.0	0.0	0.0		0.0	0.0	0.0
	Pore compressibility	c_{pore}	*1/Pa*	-	-	-	8.66E-10	-	-	8.66E-10	2.00E-09	-	5.13E-10
Mechanical parameters	Young's modulus	$E_\parallel$	*MPa*	8000	4800	2000	8000	4800	8000	8000	8000	1600	8000
		$E_\perp$		4000	2400	1000	4000	2400	4000	4000	4000	800	4000
	Shear modulus	$G_\perp$	*MPa*	3500	3500	880		3500	3500	3500	3500	3500	3500
	Poisson ratio	$\nu_\parallel$	-	0.35	0.35	0.35	0.35	0.35	0.35	0.35	0.35	0.35	0.35
		$\nu_\perp$		0.25	0.25	0.25	0.25	0.25	0.25	0.25	0.25	0.25	0.25
	Linear thermal expansion	α_T	*1/K*	1.5E-05	1.0E-05	1.5E-05	1.5E-05	1.5E-05	1.5E-05	1.5E-05	1.5E-05	1.5E-05	1.5E-05
	Biot coefficient	α	-	1	0.6	0.6	1	0.6	0.6	0.6	1	1	1

Table 21: Team parameters for Granulate Bentonite Mixture (GBM) in Step 1c

Input parameters		Symbol	Unit	GBM [3]	BGE/TU BAF	BGR/UFZ	CAS	ENSI	GRS	KAERI	LBNL	NWMO	SNL
Thermal parameters	Dry thermal conductivity parallel and perpendicular to bedding	$\lambda_{dry,\parallel}$	*W/mK*	0.35	0.35	0.4	0.28	0.4	0.26	0.4	0.3	0.35	0.3
		$\lambda_{dry,\perp}$	*W/mK*										
	Saturated thermal conductivity parallel and perpendicular to bedding	$\lambda_{sat,\parallel}$	*W/mK*	1.2	1	1.03	1.02	1.03	1	1.03	1	1.16	1
		$\lambda_{sat,\perp}$	*W/mK*										
	Solid specific heat capacity	c_s	J/kgK	800	800	800	800	800	800	800	800	800	800
Hydraulic parameters	Dry Bulk Density	ρ_{bulk}	*kg/m³*	1490	1490	1490	1490	1490	1490	1490	1490	1490	1490
	Porosity	ϕ	-	0.331	0.45	0.44	0.331	0.331	0.331	0.331	0.331	0.331	0.331
	Intrinsic permeability	$k_{i,\parallel}$	*m²*	3.5E-20	3.5E-20	1.4E-20	3.3E-20	3.5E-20	3.5E-20	3.5E-20	3.5E-20	1.75E-20	3.5E-21
		$k_{i,\perp}$											
	van Genuchten Entry Pressure	p_e	*MPa*	28.6	10.0	15.0	28.6	10.0	10.0	17.0	10.0	17.0	28.6
	van Genuchten n	n	-	2.0	1.67	1.75	2.0	1.67	1.67	2.0	1.67	2.0	1.85
	van Genuchten maximum water saturation	s_{max}	-	1.0	1.0	1.0	1.0	1.0	1.0	1.0	1.0	1.0	1.0
	van Genuchten residual water saturation	s_r	-	0.0	0.0	0.0	0.0	0.0	0.0	0.0	0.0	0.0	0.0
	Pore compressibility	c_{pore}	*1/Pa*	-	-	-	1.05E-07	-	-	1.05E-07	1.05E-07	-	6.95E-07
Mechanical parameters	Young's modulus	$E_\parallel$	*MPa*	18	18	18	18	18	18	18	18	18	18
		$E_\perp$											
	Shear modulus	$G_\perp$	*MPa*	-	-	-	-	-	-	-	-	-	-
	Poisson ratio	$\nu_\parallel$	-	0.35	0.35	0.35	0.35	0.35	0.35	0.35	0.35	0.35	0.35
		$\nu_\perp$											
	Linear thermal expansion	α_T	*1/K*	3.0E-06	3.0E-06	3.0E-06	3.0E-06	3.0E-06	3.0E-06	3.0E-06	3.0E-06	3.0E-06	3.0E-06
	Biot coefficient	α	-	1	1	1	1	1	1	1	1	1	1

Table 22: Team parameters for Bentonite Blocks (BB) in Step 1c

Input parameters		Symbol	Unit	Bentonite blocks [4]	BGE/TU BAF	BGR/UFZ	CAS	ENSI	GRS	KAERI	LBNL	NWMO	SNL
Thermal parameters	Dry thermal conductivity parallel and perpendicular to bedding	$\lambda_{dry,\parallel}$	*W/mK*	0.26	0.8	0.87	0.26	0.87	0.26	0.87	1	0.44	0.8
		$\lambda_{dry,\perp}$	*W/mK*							1			
	Saturated thermal conductivity parallel and perpendicular to bedding	$\lambda_{sat,\parallel}$	*W/mK*	0.96	0.96	1	0.96	1	0.96	0.87	1.3	1.22	1.1
		$\lambda_{sat,\perp}$	*W/mK*							1			
	Solid specific heat capacity	c_s	J/kgK	800	800	750	800	800	800	800	800	800	800
Hydraulic parameters	Dry Bulk Density	ρ_{bulk}	*kg/m³*	1690	1690	1690	1690	1690	1690	1690	1690	1690	1690
	Porosity	ϕ	-	0.331	0.331	0.36	0.331	0.331	0.331	0.331	0.331	0.331	0.331
	Intrinsic permeability	$k_{i,\parallel}$	*m²*	1.0E-22	1.0E-22	1.0E-22	1.0E-22	1.0E-22	1.0E-21	1.0E-22	2.0E-22	1.0E-22	1.0E-22
		$k_{i,\perp}$											
	van Genuchten Entry Pressure	p_e	*MPa*	30	30	40	30	30	21.9	50	64	30	30
	van Genuchten n	n	-	1.67	1.67	1.67	1.67	1.67	1.43	1.67	1.67	1.54	1.54
	van Genuchten maximum water saturation	s_{max}	-	1.0	1.0	1.0	1.0	1.0	1.0	1.0	1.0	1.0	1.0
	van Genuchten residual water saturation	s_r	-	0.0	0.0	0.0	0.0	0.0	0.0	0.0	0.0	0.0	0.0
	Pore compressibility	c_{pore}	*1/Pa*	-	-	-	1.13E-07	-	-	1.13E-07	1.13E-07	-	3.74E-07
Mechanical parameters	Young's modulus	$E_\parallel$	*MPa*	24	24	24	24	24	24	24	24	24	24
		$E_\perp$											
	Shear modulus	$G_\perp$	*MPa*	-	-	-	-	-	-	-	-	-	-
	Poisson ratio	$\nu_\parallel$	-	0.2	0.2	0.2	0.2	0.2	0.2	0.2	0.2	0.2	0.2
		$\nu_\perp$											
	Linear thermal expansion	α_T	*1/K*	3.0E-06	3.0E-06	3.0E-06	3.0E-06	3.0E-06	3.0E-06	3.0E-06	3.0E-06	3.0E-06	3.0E-06
	Biot coefficient	α	-	1	1	1	1	1	1	1	1	1	1

Appendix C: Step 2 Team Parameters

Table 23: Team parameters for Opalinus Clay in Step 2

Input parameters		Symbol	Unit	OPA [1]	BGE/TU BAF	BGR/UFZ	CAS	ENSI	GRS	KAERI	LBNL	NWMO	SNL
Thermal parameters	Dry thermal conductivity parallel and perpendicular to bedding	$\lambda_{dry,\parallel}$	*W/mK*	2.4	2.4	2.4	1.71	2.4	2.15	2.4	2.5	2.45	1.8
		$\lambda_{dry,\perp}$	*W/mK*	1.3	1.3	1.3	1.3	1.3	1.3	1.3	1	0.94	1.29
	Saturated thermal conductivity parallel and perpendicular to bedding	$\lambda_{sat,\parallel}$	*W/mK*	2.4	2.4	2.4	1.71	2.4	2.15	2.4	2.5	2.45	1.8
		$\lambda_{sat,\perp}$	*W/mK*	1.3	1.3	1.3	1.3	1.3	1.3	1.3	1	0.94	1.29
	Solid specific heat capacity	c_s	J/kgK	995	995	995	995	995	995	995	995	995	995
Hydraulic parameters	Dry Bulk Density	ρ_{bulk}	*kg/m³*	2340	2340	2340	2340	2340	2340	2340	2340	2340	2340
	Porosity	ϕ	-	0.13	0.17	0.13	0.13	0.13	0.13	0.13	0.13	0.13	0.13
	Intrinsic permeability	$k_{i,\parallel}$	*m²*	1.6E-20	6.25E-21	1.0E-20	4.0E-20	4.0E-20	1.0E-20	4.0E-20	2.0E-20	4.0E-20	1.3E-20
		$k_{i,\perp}$		1.0E-20	3.75E-21	5.0E-21	1.5E-20	1.8E-20	3.0E-21	3.0E-20	1.0E-20	1.2E-20	2.5E-21
	van Genuchten Entry Pressure	p_e	*MPa*	20.0	20.0	20.0	20.0	20.0	12.0	20.0	20.0	20.0	20.0
	van Genuchten n	n	-	2.5	2.5	2.5	2.5	2.5	1.43	2.5	2.5	2.5	2.5
	van Genuchten maximum water saturation	s_{max}	-	1.0	1.0	1.0	1.0	1.0	1.0	1.0	1.0	1.0	1.0
	van Genuchten residual water saturation	s_r	-	0.0	0.0	0.0	0.0	0.0	0.0	0.0	0.0	0.0	0.0
	Pore compressibility	c_{pore}	*1/Pa*	-	-	-	8.66E-10	-	-	8.66E-10	-	-	5.13E-10
Mechanical parameters	Young's modulus	$E_\parallel$	*MPa*	8000	4800	2000	8000	1600	8000	8000	1600	1600	8000
		$E_\perp$		4000	2400	1000	4000	800	4000	4000	800	800	4000
	Shear modulus	$G_\perp$	*MPa*	3500	3500	880		3500	3500	3500	3500	3500	3500
	Poisson ratio	$\nu_\parallel$	-	0.35	0.35	0.35	0.35	0.35	0.35	0.35	0.35	0.35	0.35
		$\nu_\perp$		0.25	0.25	0.25	0.25	0.25	0.25	0.25	0.25	0.25	0.25
	Linear thermal expansion	α_T	*1/K*	1.5E-05	1.0E-05	1.5E-05	1.5E-05	1.5E-05	1.5E-05	1.5E-05	1.5E-05	1.5E-05	1.5E-05
	Biot coefficient	α	-	1	0.6	0.6	1	0.6	0.6	0.6	1	1	1

Table 24: Team parameters for EDZ in Step 2

Input parameters		Symbol	Unit	EDZ [2]	BGE/TU BAF	BGR/UFZ	CAS	ENSI	GRS	KAERI	LBNL	NWMO	SNL
Thermal parameters	Dry thermal conductivity parallel and perpendicular to bedding	$\lambda_{dry,\parallel}$	*W/mK*	2.4	2.4			-		2.4		-	
		$\lambda_{dry,\perp}$	*W/mK*	1.3	1.3			-		1.3		-	
	Saturated thermal conductivity parallel and perpendicular to bedding	$\lambda_{sat,\parallel}$	*W/mK*	2.4	2.4			-		2.4		-	
		$\lambda_{sat,\perp}$	*W/mK*	1.3	1.3			-		1.3		-	
	Solid specific heat capacity	c_s	J/kgK	995	995			-		995		-	
Hydraulic parameters	Dry Bulk Density	ρ_{bulk}	*kg/m³*	2340	2311.8			-		2340		-	
	Porosity	ϕ	-	0.13	0.18			-		0.13		-	
	Intrinsic permeability	$k_{r,\parallel}$	*m²*	5.0E-20	5.0E-19			-		8.0E-19		-	
		$k_{r,\perp}$		1.0E-20	3.5E-19			-		5.6E-19		-	
	van Genuchten Entry Pressure	p_e	*MPa*	20	20			-		20		-	
	van Genuchten n	n	-	0.6	2.5			-		1.43		-	
	van Genuchten maximum water saturation	s_{max}	-		1.0			-				-	
	van Genuchten residual water saturation	s_r	-		0.0			-				-	
	Pore compressibility	c_{pore}	*1/Pa*		-			-		8.66306E-10		-	
					-			-				-	
Mechanical parameters	Young's modulus	$E_\parallel$	*MPa*	6000	3600			-		4000		-	
		$E_\perp$			1800			-		2000		-	
	Shear modulus	$G_\perp$	*MPa*		3500			-		3500		-	
	Poisson ratio	$\nu_\parallel$	-	0.3	0.35			-		0.35		-	
		$\nu_\perp$			0.25			-		0.25		-	
	Linear thermal expansion	α_T	*1/K*	1.50E-05	1.00E-05			-		1.50E-05		-	
	Biot coefficient	α	-	1	0.6			-		1		-	

Table 25: Team parameters of Granular Bentonite Mixture (GBM) in Step 2

Input parameters		Symbol	Unit	GBM [3]	BGE/TU BAF	BGR/UFZ	CAS	ENSI	GRS	KAERI	LBNL	NWMO	SNL
Thermal parameters	Dry thermal conductivity parallel and perpendicular to bedding	$\lambda_{dry,\parallel}$	*W/mK*	0.35	0.35	0.4	0.23	0.4	0.26	0.4	0.25	0.35	0.3
		$\lambda_{dry,\perp}$	*W/mK*										
	Saturated thermal conductivity parallel and perpendicular to bedding	$\lambda_{sat,\parallel}$	*W/mK*	1.2	1	1.03	1.02	1.03	1	1.03	1	1.16	1
		$\lambda_{sat,\perp}$	*W/mK*										
	Solid specific heat capacity	c_s	J/kgK	800	800	800	800	800	800	800	800	800	800
Hydraulic parameters	Dry Bulk Density	ρ_{bulk}	*kg/m³*	1490	1490	1490	1490	1490	1490	1490	1490	1490	1490
	Porosity	ϕ	-	0.331	0.45	0.44	0.331	0.331	0.331	0.331	0.331	0.331	0.331
	Intrinsic permeability	$k_{i,\parallel}$	*m²*	3.5E-20	3.5E-20	1.4E-20	3.3E-20	3.5E-20	1.0E-20	3.5E-20	3.5E-20	1.75E-20	3.5E-21
		$k_{i,\perp}$											
	van Genuchten Entry Pressure	p_e	*MPa*	28.6	10.0	15.6	28.6	30.0	10.0	28.6	10.0	17.0	28.6
	van Genuchten n	n	-	2.0	1.67	1.75	2.0	3.00	1.67	2.0	1.67	2.0	1.85
	van Genuchten maximum water saturation	s_{max}	-	1.0	1.0	1.0	1.0	1.0	1.0	1.0	1.0	1.0	1.0
	van Genuchten residual water saturation	s_r	-	0.0	0.0	0.0	0.0	0.0	0.0	0.0	0.0	0.0	0.0
	Pore compressibility	c_{pore}	*1/Pa*	-	-	-	1.05E-07	-	-	1.05E-07	-	-	1.50E-06
Mechanical parameters	Young's modulus	$E_\parallel$	*MPa*	18	18	18	18	18	18	18	18	18	18
		$E_\perp$											
	Shear modulus	$G_\perp$	*MPa*	-	-	-	-	-	-	-	-	-	-
	Poisson ratio	$\nu_\parallel$	-	0.35	0.35	0.35	0.35	0.35	0.35	0.35	0.35	0.35	0.35
		$\nu_\perp$											
	Linear thermal expansion	α_T	*1/K*	3.0E-06	3.0E-06	3.0E-06	3.0E-06	3.0E-06	3.0E-06	3.0E-06	3.0E-06	3.0E-06	3.0E-06
	Biot coefficient	α	-	1	1	1	1	1	1	1	1	1	1

Table 26: Team parameters of Bentonite Blocks (BB) in Step 2

Input parameters		Symbol	Unit	Bentonite blocks [4]	BGE/TU BAF	BGR/UFZ	CAS	ENSI	GRS	KAERI	LBNL	NWMO	SNL
Thermal parameters	Dry thermal conductivity parallel and perpendicular to bedding	$\lambda_{dry,\parallel}$	*W/mK*	0.26	0.8	0.87	0.26	0.87	0.26	0.87	1	0.44	0.8
		$\lambda_{dry,\perp}$	*W/mK*							1			
	Saturated thermal conductivity parallel and perpendicular to bedding	$\lambda_{sat,\parallel}$	*W/mK*	0.96	0.96	1	0.96	1	0.96	0.87	1.3	1.16	1.1
		$\lambda_{sat,\perp}$	*W/mK*							1			
	Solid specific heat capacity	c_s	J/kgK	800	800	750	800	800	800	800	800	800	800
Hydraulic parameters	Dry Bulk Density	ρ_{bulk}	*kg/m³*	1690	1690	1690	1690	1690	1690	1690	1690	1690	1690
	Porosity	ϕ	-	0.331	0.331	0.36	0.331	0.331	0.331	0.331	0.331	0.331	0.331
	Intrinsic permeability	$k_{i,\parallel}$	*m²*	1.0E-22	1.0E-22	1.0E-22	1.0E-22	1.0E-22	1.0E-21	1.0E-22	2.0E-21	2.0E-22	1.0E-22
		$k_{i,\perp}$											
	van Genuchten Entry Pressure	p_e	*MPa*	30	30	40	30	30	21.9	30	30	64	30
	van Genuchten n	n	-	1.67	1.67	1.67	1.67	1.67	1.43	1.67	1.67	1.67	1.54
	van Genuchten maximum water saturation	s_{max}	-	1.0	1.0	1.0	1.0	1.0	1.0	1.0	1.0	1.0	1.0
	van Genuchten residual water saturation	s_r	-	0.0	0.0	0.0	0.0	0.0	0.0	0.0	0.0	0.0	0.0
	Pore compressibility	c_{pore}	*1/Pa*	-	-	-	1.13E-07	-	-	1.13E-07	-	-	2.00E-06
Mechanical parameters	Young's modulus	$E_\parallel$	*MPa*	24	24	24	24	24	24	24	24	24	24
		$E_\perp$											
	Shear modulus	$G_\perp$	*MPa*	-	-	-	-	-	-	-	-	-	-
	Poisson ratio	$\nu_\parallel$	-	0.2	0.2	0.2	0.2	0.2	0.2	0.2	0.2	0.2	0.2
		$\nu_\perp$											
	Linear thermal expansion	α_T	*1/K*	3.0E-06	3.0E-06	3.0E-06	3.0E-06	3.0E-06	3.0E-06	3.0E-06	3.0E-06	3.0E-06	3.0E-06
	Biot coefficient	α	-	1	1	1	1	1	1	1	1	1	1

Table 27: Team parameters of Shotcrete in Step 2

Input parameters		Symbol	Unit	Shotcrete [6]	BGE/TU BAF	BGR/UFZ	CAS	ENSI	GRS	KAERI	LBNL	NWMO	SNL
Thermal parameters	Dry thermal conductivity parallel and perpendicular to bedding	$\lambda_{dry,\parallel}$	*W/mK*	1	1.06	-		1		1.7		0.1	0.3
		$\lambda_{dry,\perp}$	*W/mK*										
	Saturated thermal conductivity parallel and perpendicular to bedding	$\lambda_{sat,\parallel}$	*W/mK*	1.7	1.7	-		1.7		1.7		0.3	0.5
		$\lambda_{sat,\perp}$	*W/mK*										
	Solid specific heat capacity	c_s	J/kgK	750	750	-		750		750		750	750
Hydraulic parameters	Dry Bulk Density	ρ_{bulk}	*kg/m³*	1725	2076.3	-		1725		2300		1725	1725
	Porosity	ϕ	-	0.25	0.231	-		0.25		0.23		0.25	0.25
	Intrinsic permeability	$k_{i,\parallel}$	*m²*	1.00E-19	1.15E-17	-		1.75E-19		1.00E-17		1.00E-19	2.00E-21
		$k_{i,\perp}$											
	van Genuchten Entry Pressure	p_e	*MPa*	1	1	-		1		1		1	20
	van Genuchten n	n	-	1.49	1.49	-		1.49		1.49		1.49	2.5
	van Genuchten maximum water saturation	s_{max}	-	1	1	-		1		1		1	1
	van Genuchten residual water saturation	s_r	-	0.01	0.01	-		0.01		0.01		0.01	0.01
	Pore compressibility	c_{pore}	*1/Pa*	-	-	-		-		1.40E-10		-	3.50E-12
Mechanical parameters	Young's modulus	$E_\parallel$	*MPa*	20000	21500	-		20000		20000		20000	
		$E_\perp$											
	Shear modulus	$G_\perp$	*MPa*	-	-	-		-		-		-	
	Poisson ratio	$\nu_\parallel$	-	0.15	0.15	-		0.15		0.15		0.15	
		$\nu_\perp$											
	Linear thermal expansion	α_T	*1/K*	1.50E-05	1.50E-05	-		1.50E-05		1.50E-05		1.50E-05	
	Biot coefficient	α	-	1	1	-		1		1		1	

Appendix D: Sensitivity analysis of tunnel convergence (2D)

Analyses of tunnel convergence were performed in a 2D plane strain setting in OpenGeoSys-6 using the TRM process model by BGE/TUBAF. The parameter variations focused on the effect of anisotropy in thermal, hydraulic and mechanical properties of the Opalinus clay as well as the effect of mechanical boundary conditions. The stiffness of granular bentonite was also varied. Base-line values were as in the main part of the report (Table 20, Table 21, Table 22).

Here, we refrain from a detailed presentation of the variations themselves and instead summarize some of the key findings that can help in interpreting the results discussed in the main part of the report:

- The stiffness of granular bentonite mainly impacted displacements at the tunnel contour, where a stiffer GBM led to higher divergence of the tunnel and lower convergence at later time points.
- Considering the stiffness anisotropy of clay rock was important because radial displacements at points parallel and perpendicular to the bedding plane differ. There were also qualitative differences with more pronounced non-monotonic displacement over time in the anisotropic case. Mechanical anisotropy could lead to convergence in one direction while divergence was observed in the other direction.
- The occurrence of convergence in the near field was increased if, additionally, anisotropy of thermal expansion was accounted for.
- Often, $\nu_{\perp}$is given in specifications making it unclear whether $\nu_{\perp\parallel}$ is implied or $\nu_{\parallel\perp}$. This frequent model input error related to $\nu_{ij} \neq \nu_{ji}$ had a significant impact on predicted displacements. It led to deviations that exceeded those contributed by other parameter variations. Great care therefore had to be taken to avoid this mistake. For the same reason, parameters should not be given non-unique identifiers such as $\nu_{\perp}$.
- Anisotropy of thermal conductivity affected the magnitude of the displacement predictions significantly, but did not alter the overall trends of the pressure curves.

- Anisotropy of intrinsic permeability also contributed to quantitative differences and to a certain degree qualitative differences, but not as strongly as mechanical anisotropy.
- There was a very strong effect of mechanical boundary conditions. If the outside boundaries were isostatic, the tunnel tended to diverge. If the outside boundaries were constrained in their normal direction, the cavity converged If boundaries orthogonal to each other were assigned different types of boundary conditions, convergence was observed in the direction of the constrained boundary, expansion in the direction of the isostatic boundary.